Phase Equilibria Predictions of Binary Mixtures of Light/Heavy Hydrocarbons by Monte Carlo Simulations

Zsolt Csaszar

Technische Universiteit Delft

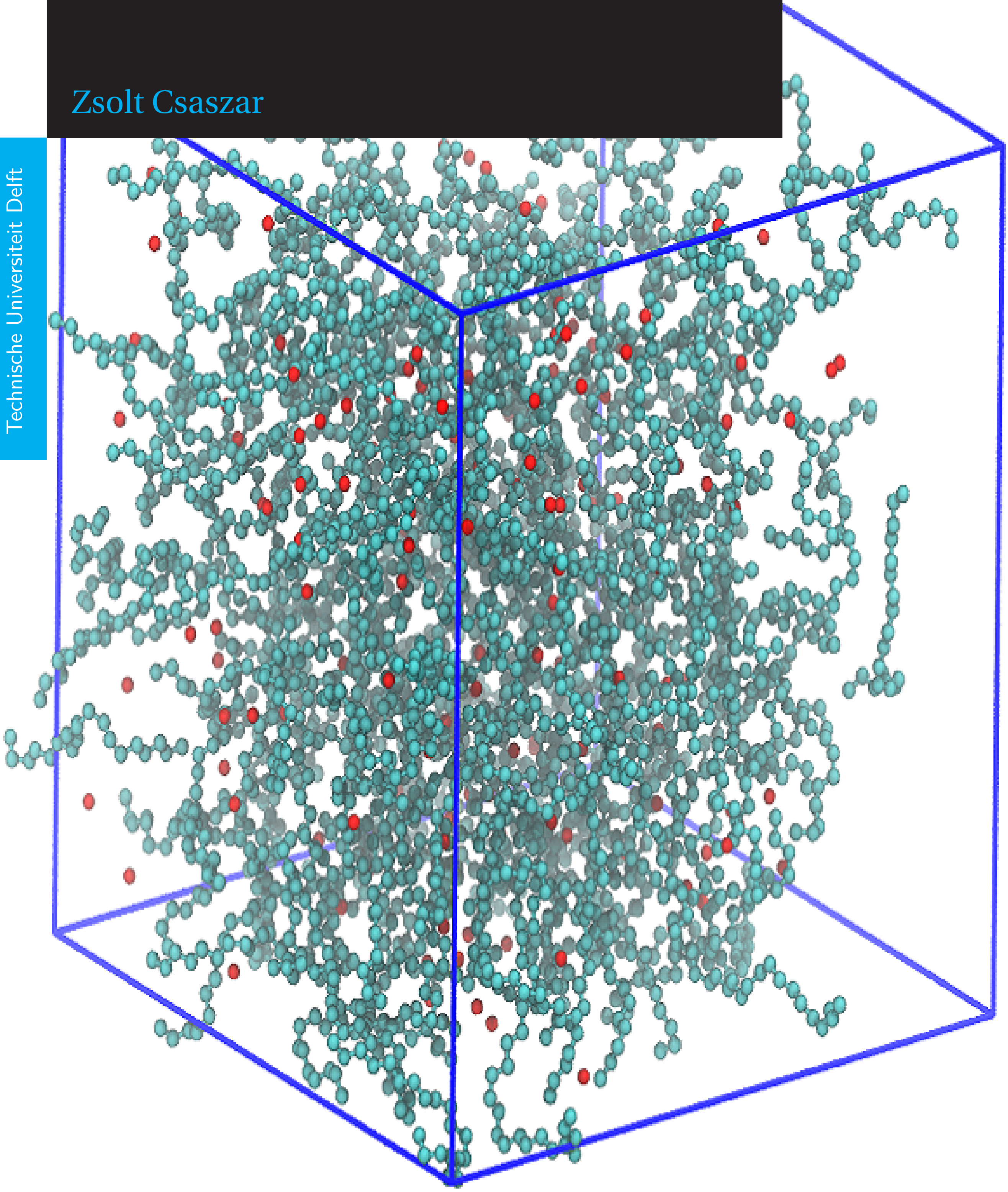

Delft University of Technology

Challenge the future

PHASE EQUILIBRIA PREDICTIONS OF BINARY MIXTURES OF LIGHT/HEAVY HYDROCARBONS BY MONTE CARLO SIMULATIONS

by

Zsolt Csaszar

in partial fulfillment of the requirements for the degree of

Master of Science
in Mechanical Engineering

at the Delft University of Technology,
to be defended publicly on the 31^{st} of October, 2017 at 13:00 PM.

Professor:	Prof. dr. ir. Thijs J. H. Vlugt	TU Delft
Supervisor:	Dr. Othon A. Moultos	TU Delft
Thesis committee:	Dr. ir. Remco M. Hartkamp	TU Delft
	Dr. ir. Mahinder Ramdin	TU Delft

CONTENTS

Nomenclature

Roman Symbols

$\mathcal{N}(s_n)$	Probability of finding a system in the new configuration, page 10
$\mathcal{N}(s_o)$	Probability of finding a system in the old configuration, page 10
$\mathcal{U}$	Potential energy, page 15
$\mathcal{U}\left(s_n^{n_I}\right)$	Potential energy of the new configuration of n_I molecules, page 14
$\mathcal{U}\left(s_o^{n_I}\right)$	Potential energy of the old configuration of n_I molecules, page 14
$\mathcal{U}^{tail}$	Potential of the applied analytical tail correction, page 19
$\mathcal{U}_{bend}(\theta)$	Bending potential, page 22
$\mathcal{U}_{bond}$	Bond-stretching potential, page 21
$\mathcal{U}_{LJ}\left(r_{ij}\right)$	Interaction energy, page 18
$\mathcal{U}_{molecule}$	Potential energy of a molecule, page 21
$\mathcal{U}_{nonbonded}$	Potential energy of the nonbonded interactions, page 21
$\mathcal{U}_{system}$	Potential energy of the simulated system, page 21
$\mathcal{U}_{torsion}(\phi)$	Torsion potential, page 22
$\overline{x}$	Average value of interest of the simulations, page 24
a	'Attraction' parameter, page 2
a_{ij}	Cross energy parameter , page 5
a_i	Energy parameter of component i, page 5
a_j	Energy parameter of component j, page 5
$acc(s_n \rightarrow s_o)$	Acceptance probability of a move from the new configuration to the old, page 10
$acc(s_o \rightarrow s_n)$	Acceptance probability of a move from the old configuration to a new, page 10
b	'Repulsion' parameter, page 2
b_{ij}	Cross co-volume parameter , page 5
c_0	Torsion potential constant, page 22
c_1	Torsion potential constant, page 22
c_2	Torsion potential constant, page 22
c_3	Torsion potential constant, page 22

E	Energy of the system, page 10
G	Gibbs free energy, page 10
$K(s_n \rightarrow s_o)$	Number of moves from s_n to s_o, page 10
$K(s_o \rightarrow s_n)$	Number of moves from s_o to s_n, page 10
k_θ	Bending potential constant, page 22
k_{ij}	Binary interaction parameter , page 5
l_{ij}	Binary interaction parameter , page 5
N	Number of molecules of the system, page 10
N	Number of simulations per state points, page 24
n_{II}	Number of particles in region II, page 14
n_I	Number of particles in region I, page 14
p	Pressure, page 2
p	System pressure, page 11
p_{cricon}	Cricondenbar, page 3
q_i	Charge of interaction site i, page 18
q_j	Charge of interaction site j, page 18
Q_{NPT}	Partition function in the NPT ensemble, page 15
Q_{NVT}	Partition function in the NVT ensemble, page 14
R	Universal gas constant, page 2
r	Length of the bond, page 21
r_{cut}	Cut-off radius, page 18
r_{ij}	Distance of between between interaction sites, page 18
r_o	Reference length of the bond, page 21
S	Entropy, page 10
s^N	Scaled coordinates, page 15
$s_{II}^{N-n_I}$	Scaled coordinates of region II, page 14
$s_I^{n_I}$	Scaled coordinates of region I, page 14
s_n	New system configuration, page 10
s_o	Old system configuration, page 10
T	System temperature, page 11

T	Temperature, page 2
T_{cricon}	Cricondentherm temperature, page 3
V	Volume of the system, page 10
v	molar volume, page 2
v	specific volume, page 3
V_I	Volume of region I, page 14
V_{II}	Volume of region II, page 14
val_{exp}	Values of experiments, page 27
val_{sim}	Values of simulations, page 27
x	Concentration, page 2
x_i	Value of interest of a simulation, page 24
x_{C_1}	Mole fraction of methane, page 4
x_i	Mole fraction of component i, page 5
x_j	Mole fraction of component j, page 5
Z	Compressibility factor, page 4
Z^{disp}	Perturbation contribution term , page 4
Z^{hc}	Hard-chain contribution term , page 4
Z^{id}	Ideal gas contribution term, page 4

Greek Symbols

$\alpha\left(s_n \rightarrow s_o\right)$	Probability of performing a trial move from the new configuration to the old, page 10
$\alpha\left(s_o \rightarrow s_n\right)$	Probability of performing a trial move from the old configuration to the new, page 10
α	Species of the system, page 13
β	Reciprocal temperature, page 14
ϵ	Segment energy, page 5
$\epsilon_{CH_3}^{ethane}$	Well-depth parameter of the methyl group for ethane, page 20
ϵ_0	Vacuum permittivity constant, page 18
ϵ_{CH_2}	Well-depth parameter of the methylene group for an *n*-alkane, page 20
ϵ_{CH_3}	Well-depth parameter of the methyl group for an *n*-alkane, page 20
ϵ_{ij}	Well-depth parameter between interaction sites, page 18

ϵ_i	Well-depth parameter of interaction site i, page 18
ϵ_j	Well-depth parameter of interaction site, page 18
Λ	Thermal de Broglie wavelength, page 14
λ	Scaling parameter of fractional molecules, page 16
$\AA$	Angström, page 21
μ	Chemical potential, page 11
ϕ	Dihedral angle, page 22
ρ	Density, page 2
σ	Segment diameter, page 5
$\sigma_{CH_3}^{ethane}$	Diameter parameter of the methyl group for ethane, page 20
σ_{CH_2}	Diameter parameter of the methylene group for an *n*-alkane, page 20
σ_{CH_3}	Diameter parameter of the methyl group for an *n*-alkane, page 20
σ_{ij}	Diameter parameter between between interaction sites, page 18
σ_i	Diameter parameter of interaction site i, page 18
σ_j	Diameter parameter of interaction site j, page 18
θ	Angle between bonds, page 22
θ_0	Reference angle between bonds, page 22

Abbreviations

$AMBER$	Assisted model building with energy refinement, page 20
Btu	British thermal unit, page 1
$CFCMC$	Continuous Fractional Component Monte Carlo, page 16
$CMBC$	Configurational Bias Monte Carlo, page 6
EOS	Equation of State, page 2
$OPLS$	Optimized potentials for liquid simulations, page 20
$PC-SAFT$	Perturbed chain statistical associated fluid theory, page 1
PR	Peng - Robinson, page 4
SKS	Siepmann-Karaborni-Smit, page 20
SRK	Soave - Redlich - Kwong, page 4
$TraPPE$	Transferable potentials for phase equilibria , page 20

Hydrocarbons

C	Carbon, page 18
C_1	Methane, page 6
C_{12}	Dodecane, page 6
C_{14}	Tetradecane, page 6
C_{16}	Hexadecane, page 6
C_{20}	Eicosane, page 6
C_{24}	Tetracosane, page 6
CH	Methyne, page 18
CH_2	Methylene group, page 18
CH_3	Methyl group, page 18
CH_4	Methane, page 18

LIST OF FIGURES

LIST OF TABLES

ACKNOWLEDGMENT

First and foremost, I would like to thank my parents who made this remarkable journey possible and who always supported me. During the last years I had the possibility to meet with many incredible people from all over the world, got to know their culture, their thinking and their view of life. This experience of studying abroad made me a better person and I will carry these precious memories through my entire life.

Furthermore, I would like to express my sincere gratitude to Prof. dr. ir. Thijs J. H. Vlugt who accepted me in his Engineering Thermodynamics group and provided the topic of the thesis for me.

I would also like to express my sincere gratitude to my supervisor Dr. Othon Moultos, who helped me during these last months. His constant encouragement, passion, support, humor and advice helped me to enjoy this topic and successfully deliver my thesis.

In addition, I am also grateful to my daily supervisors Dr. ir. Mahinder Ramdin and Ali Poursaeidesfahani, who helped me with pleasure even when I just had a tiniest problem or question. Through their in-depth knowledge of molecular simulations supported me to find quick solutions for any arisen problem. Without them the outcome of the thesis would not have been the same.

Moreover, I would like to express my sincere gratitude to Professor Ioannis Economou and to Ilias Nikolaidis who are members of the collaborating research group which provided the $PC-SAFT$ calculations during my work.

Finally, I would like to thank all my Hungarian and especially all my Dutch friends who made these last years amazing.

Zsolt Csaszar
Delft University of Technology
05 October 2017

ABSTRACT

For the design and optimization of different processes and technologies in the chemical and petrochemical industry, the knowledge of the accurate vapor-liquid phase equilibrium of hydrocarbons and their binary mixtures is fundamental. The main focus of this thesis is the binary mixtures of methane with various *n*-alkanes and the binary mixture of methane and toluene, at temperatures ranging from 400 to 650 K and pressures ranging from 2 MPa to 50 MPa.

Despite the currently increased importance of these asymmetric binary mixtures of methane and long *n*-alkanes due to Enhanced Oil Recovery technologies and depletion of old, easily accessible and highly profitable hydrocarbon reservoirs, the available vapor-liquid equilibrium (VLE) data from experiments are scarce or unknown.

Currently, the most common practice for volumetric and phase behavior calculations in the industry is based on different cubic, such as Peng-Robinson, SRK or on higher order equations of state like $PC-SAFT$. However, the predicted data by equations of state are not accurate enough, due to the lack of experimental data. This is more pronounced for high temperature and pressure conditions or in the vicinity of the critical point.

This thesis aims to produce vapor-liquid phase equilibrium data for binary mixtures of methane with various long *n*-alkanes by performing Monte Carlo molecular simulations in the Gibbs ensemble with $TraPPE$ force field. The simulation results are used to validate the applied $TraPPE$ force field by comparing its results to available experimental data. At extrapolated conditions, the new data are compared to $PC-SAFT$ predictions in order to assess the performance of the $CBMC$ technique and to highlight the deviations between the $CBMC$ and $PC-SAFT$ results. Additionally, this new data could be used to adjust the parameters of the applied $PC-SAFT$ equation of state to achieve better predictions at extrapolated conditions.

1

INTRODUCTION

The steadily increasing energy demand[1, 2] due to the rapidly growing population, is mainly covered and will be covered from fossil resources in the upcoming years (fig. 1.1, fig. 1.2). Companies considering techniques and reservoirs that earlier were not considered, such as non-conventional reservoirs with heavy and exta-heavy crude oils [3–5] and Enhanced Oil Recovery Technologies[6] with injection of CH_4 or CO_2.

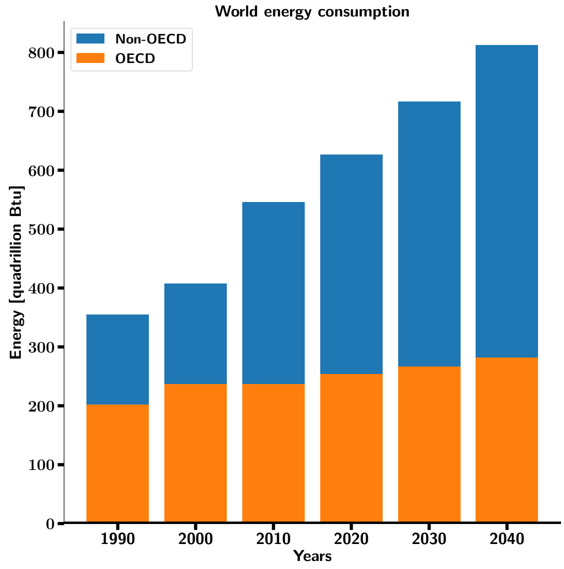

Figure 1.1: World energy consumption in quadrillion Btu, 1990-2040[1]

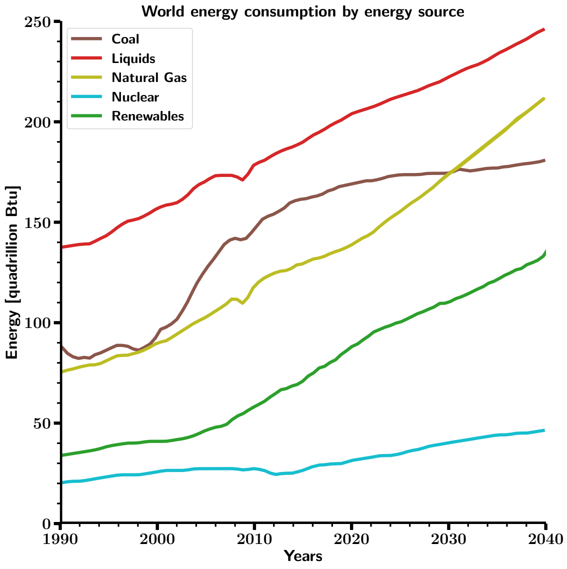

Figure 1.2: World energy consumption by energy source in quadrillion Btu, 1990-2040[1]

For these reasons, accurate phase equilibrium calculations of asymmetric binary mixtures, binaries of methane with long *n*-alkanes, became more and more important in the recent years in petroleum engineering applications and in the design and optimization of new processes in the chemical and petrochemical industry. However, the current approach of phase equilibrium calculations in the industry is based on applications of the modified version of the classic Redlich and Kwong[7] cubic equation of state, such as Peng-Robinson[8] or Soave-Redlich-Kwong[9] or on higher order equations of state like perturbed chain statistical associated fluid theory $(PC-SAFT)$[10–12].

1.1. PHASE EQUILIBRIUM AND EQUATIONS OF STATE

An equation of state is a function which relates pressure, temperature and volume. It describes the phase and volumetric behavior of single-component and multi-component systems. The only required input parameters are the critical properties and the acentric factors of each constituent component of the system of interest. The base of all currently used cubic equations of state was proposed in the nineteenth century by van der Waals[13].

$$p = \frac{RT}{v-b} - \frac{a}{v^2} \tag{1.1}$$

In eq. (1.1), where R stands for the universal gas constant, T is the temperature, p stands for pressure, a is the so called 'Attraction' parameter, b is the 'Repulsion' parameter and v stands for the molar volume, the first term on the right side describes the behavior of the liquid phase, while the second term on the right side describes the behavior of the gas phase. Van der Waals' equation has given a much better approximation for the phase and volumetric behavior of systems compared to the ideal gas law in its time.

The calculated results by equations of state are usually represented in different phase diagrams. The most commonly used diagrams are the $p-x, p-T, T-v$ and $T-\rho$ diagrams. However, the form of the phase diagrams depend on the type of the system. The shapes of the different phase diagrams for an arbitrary single-component and for an arbitrary multi-component system will be introduced in the following paragraphs.

A general single component $p-T$ phase diagram can be seen in fig. 1.3. For hydrocarbons the region of our interest is located above and below of the blue curve. The blue curve indicates those system points where saturated vapor and liquid coexist. Above the coexistence line only liquid phase can be found ,while below the coexistence line only vapor phase can be found. The critical point of this generic single-component system can be found at the highest temperature and at the highest pressure point on the coexistence curve.

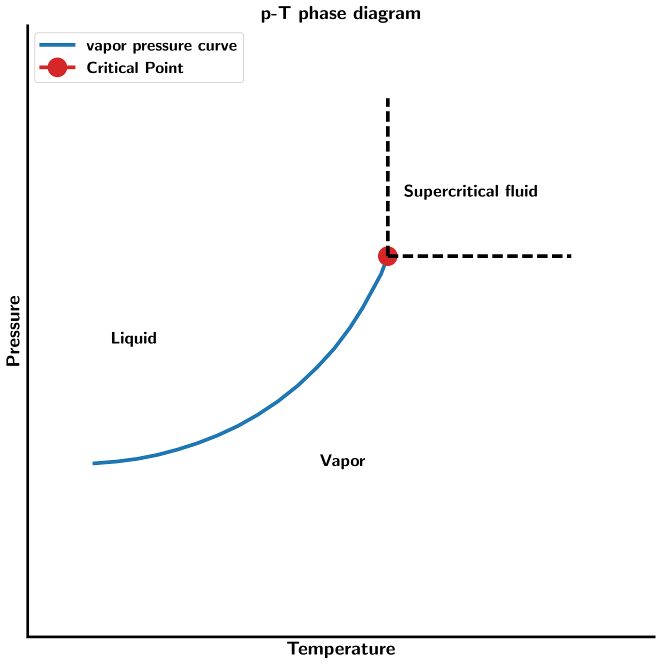

Figure 1.3: $p-T$ diagram of an arbitrary single-component system

The critical point defines the critical temperature and the critical pressure of the pure component. At the critical point the vapor and liquid phases are indistinguishable from each other, their physical properties are identical. The critical temperature defines the temperature above which liquid and vapor cannot coexist, only one phase can be found, regardless the pressure. The critical pressure defines that pressure above liquid and vapor cannot coexist, only one phase can be found, regardless the temperature[14, 15].

Furthermore, an other useful and frequently used phase diagram for pure component systems is the $T-v$ diagram that can be seen in fig. 1.4. On this diagram the blue curve, which is called the bubblepoint curve, represents the saturated liquid phase. To the left from the bubblepoint curve only undersaturated liquid phase can be found. The orange curve, which is called the dewpoint curve, indicates the saturated vapor phase. To the right from the dewpoint curve only superheated vapor can be found. The area enclosed by the bubblepoint and by the dewpoint curve is the two phase region, where both phases can coexist. The point where the bubblepoint curve and the dewpoint curve merge is the critical point.

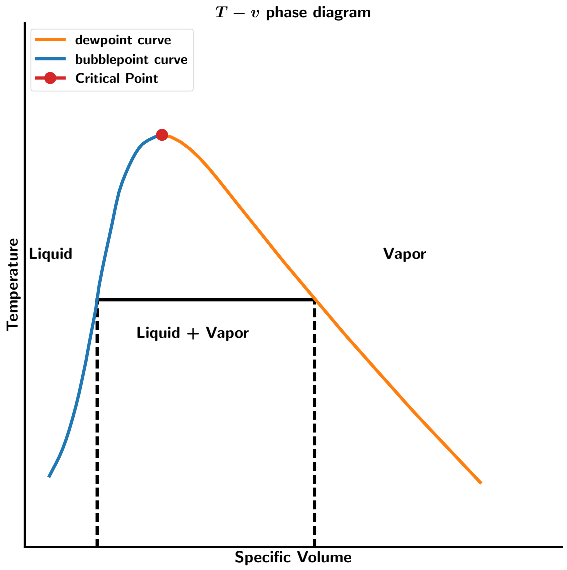

Figure 1.4: $T-v$ phase diagram of an arbitrary single-component system

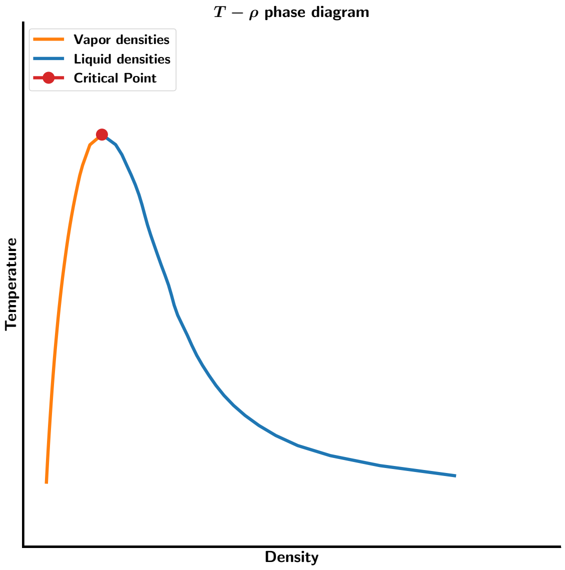

Figure 1.5: $T-\rho$ phase diagram of an arbitrary single-component system

This phase diagram is particularly useful when liquid and vapor densities must be obtained due to the fact that the density is inverse function of the specific volume. A $T-\rho$ phase diagram can be seen in fig. 1.5.

For binary mixtures the shape of the previously described diagrams are different due to the fact that both the pressure and the temperature affect the behavior of the system in the saturated region. Compared to a single-component (fig. 1.3) system, there are major differences. Firstly, on the $T-p$ phase diagram (fig. 1.6) the bubble- and dewpoint curves do not coincide anymore. It means that the vapor and liquid coexistence is defined by a region rather than a curve. Moreover, the existence of the two phase region is no longer defined by the critical point. For a binary system the critical point is defined as the intersection of the dewpoint and bubblepoint curve[14, 16].Furthermore, in contrast to the single-component system, liquid and vapor phases can still coexist above the critical temperature or critical pressure. For a binary system the highest temperature until two phases can coexist is defined by the cricondentherm T_{cricon}. The highest pressure until two phases can coexist is defined by the cricondenbar p_{cricon} (fig. 1.6). It must also be mentioned that for binary mixtures

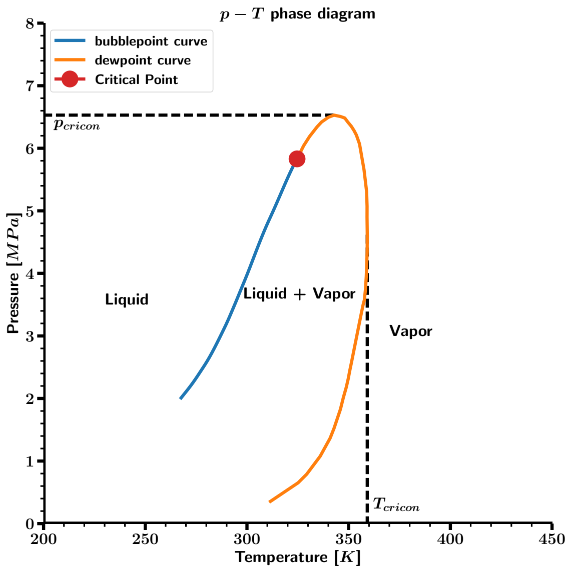

Figure 1.6: $p-T$ diagram for a $C_2/n-C_7$ mixture with 96.83mol% ethane[17]

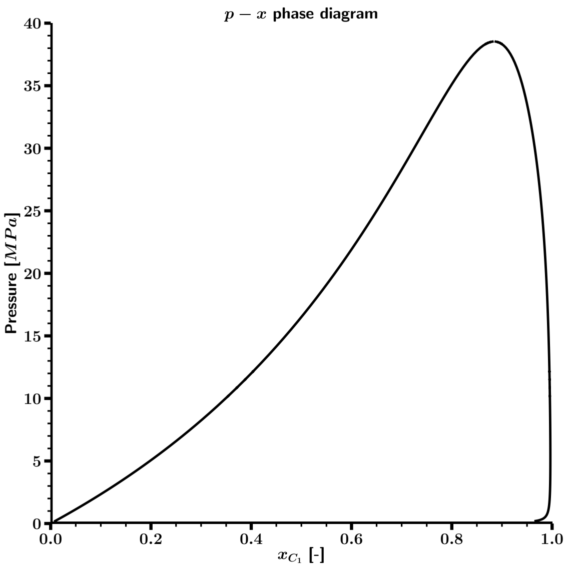

Figure 1.7: $p-x$ diagram for C_1/C_{12} mixture on $T = 400K$

the concentration changes the shape of the different phase diagrams. For example, for a $p-T$ diagram, the mole fraction x of one of the constituent component must be specified. An other useful phase diagram which will be frequently used in this thesis for phase equilibrium representations is the $p-x$ diagram (fig. 1.7). The advantage of using $p-x$ phase diagrams is shown when experimental data are compared to simulation data due to the fact that phase equilibrium experiments are performed at fix temperature T or at fix pressure p. Thus, the vapor-liquid phase equilibrium diagrams are mainly reported in $p-x$ or in $T-x$ format.

As mentioned earlier, during industrial applications the current phase and volumetric behavior calculations are made with different equations of state. The most commonly used equations of state are the Peng - Robinson, $PR\ EOS$ (eq. (1.2)), the Soave - Redlich - Kwong, $SRK\ EOS$ (eq. (1.3)) and the Perturbed Chain Statistical Associated Fluid Theory, $PC-SAFT$ (eq. (1.4)).

$$p = \frac{RT}{v-b} - \frac{a}{v(v+b)+b(v-b)} \tag{1.2}$$

$$p = \frac{RT}{v-b} - \frac{a}{v(v+b)} \tag{1.3}$$

$$Z = Z^{id} + Z^{hc} + Z^{disp} \tag{1.4}$$

The notations in eq. (1.2) and in eq. (1.3) are identical to the notations in eq. (1.1). In eq. (1.4) Z stands for the compressibility factor, with $Z = \frac{p \cdot v}{R \cdot T}$, Z^{id} being the ideal gas contribution, Z^{hc} is the hard-chain contribution and Z^{disp} is the perturbation contribution which accounts for the attractive interactions[12].

These equations of state became popular due to their simplicity and applicability over wide range of temperatures and pressures. However, it is also known[14] that liquid densities calculated by PR or SRK equation of state are underestimated for any pure hydrocarbon or hydrocarbon mixture. One of the reasons behind this behavior is the fact that the different parameters used in these equations of state ($PR\ EOS$ and $SRK\ EOS$) are calculated by utilizing vapor pressures and critical properties of the constituent components of the mixture. On the contrary, parameters of the $PC-SAFT$ equation of state are fitted to vapor pressures and liquid densities[18]. This is one of the reasons why the $PC-SAFT$ results are more accurate than PR or SRK predictions. However, $PC-SAFT$ overestimates the critical point[18].

Additionally, an other source of the deviation of the predicted values by equations of state from the experimental values lies in the application of inaccurate binary interaction parameters. These binary interaction parameters are important part of the combining rules (eq.(1.7 and 1.8)), that are applied in different equations of state to calculate vapor-liquid phase equilibria of mixtures. The most commonly employed mixing rules for PR and SRK are the van der Waals one-fluid mixing rules[18], where a_i is the energy parameter of component i, a_j is the energy parameter of component j , a_{ij} stands for the cross energy parameter, b_{ij} represents the cross co-volume parameter, k_{ij} and l_{ij} are binary interaction parameters and x_i and x_j stand for mole fractions of component i and j in the mixture. For $PC-SAFT$ Lorentz-Berthelot combining rules are applied (eq.(1.9 and 1.10)), where σ stands for the segment diameter and ϵ means the segment energy.

$$a = \sum_{i=1}^{n} \sum_{j=1}^{n} x_i \cdot x_j \cdot a_{ij} \tag{1.5}$$

$$b = \sum_{i=1}^{n} \sum_{j=1}^{n} x_i \cdot x_j \cdot b_{ij} \tag{1.6}$$

$$a_{ij} = \sqrt{a_i \cdot a_j} \cdot (1 - k_{ij}) \tag{1.7}$$

$$b_{ij} = \frac{b_i + b_j}{2} \cdot (1 - l_{ij}) \tag{1.8}$$

$$\sigma_{ij} = \frac{1}{2} \cdot (\sigma_i + \sigma_j) \tag{1.9}$$

$$\epsilon_{ij} = (\epsilon_i \cdot \epsilon_j)^{\frac{1}{2}} \cdot (1 - k_{ij}) \tag{1.10}$$

These binary interaction parameters are fitted to available phase equilibrium data. If data are not available, the binary interaction parameter value can be estimated by applying geometric mean value calculation[18] (eq. (1.11)).

$$a_{ij} = \sqrt{a_i \cdot a_j} \tag{1.11}$$

However, the calculated interaction parameter is often much higher[18] than the actual value that would be needed to fit the predicted equation of state data to experimental data.

1.2. SIMULATIONS AND EXPERIMENTS

Traditionally, vapor-liquid phase equilibrium data are obtained from experiments. The problem with this approach is that it could be dangerous. For example, performing meauserments at high temperature and pressure conditions or when hazardous substances are dealt with[19].

An alternative approach that emerged together with the rapid evolution of the computational power is the molecular simulation. It provides solution for the drawback of the experiments, namely any kind of temperature and pressure state point can be simulated for any substance without compromising safety. Additionally, this approach can be used for investigating the phase and volumetric behaviors at extrapolated conditions.

A prerequisite for the successful implementation of molecular simulations is the detailed and accurate description of the intra- and intermolecular interactions. For this reason, a large number of force fields, for many important substances, including hydrocarbons, have been reported in the literature, during the last decades. Detailed reviews of these force fields are presented in [20–26].

A thorough literature study was conducted, covering the experimental and simulation findings of the light/heavy binary mixtures of hydrocarbons.

One of the mixtures idetified after the literature review is the methane - hexadecane ($C_1 - C_{16}$) binary mixture. Mohammed *et al.*[27] reported experimental viscosity and density results for $C_1 - C_{16}$ mixture at temperatures from 298 to 473 K and at pressures up to 120 MPa. Lin *et al.*[28] reported experimental vapor-liquid phase equilibrium composition results for $C_1 - C_{16}$ mixture. In their paper, the temperature range was selected between 462.45 and 703.55 K and the pressure varied between 2 and 50 MPa. Suleiman *et al.*[29] reported C_{16} experimental solubility values of n-alkanes in methane at temperatures from 293.2 to 423.2 K and at pressures from 12 to 24 MPa. Experiments were also performed by Le Roy *et al.*[30], mainly focused on liquid phase properties of this binary mixture and they reported densities and bubble pressures at temperatures from 324 to 413.2 K and at mole fractions from 30.5 – 65.9% of methane. Furthermore, Fenghour *et al.*[31] reported bubble pressures and liquid densities with less than ±0.1% accuracy. Their measurements were performed at temperatures from 375 to 475 K and at pressures from 20 to 60 MPa. Overview of the found articles of this mixture can be seen in table 1.3.

An other binary mixture of our investigation is the methane - dodecane ($C_1 - C_{12}$) binary mixture. For this specific binary mixture significantly less experimental results are available in literature. One of the found experimental results were performed by Rijkers *et al.*[32]. In this paper vapor-liquid and solid-vapor phase equilibrium results are reported for temperatures between 240 and 315 K and for pressures up to 51 MPa. Böttger *et al.*[33] also performed measurements on this specific binary mixture at ambient temperatures. They reported the solubility of methane in the liquid phase at 273.1 K and at pressures up to about 10 MPa. Beside experiments, few simulation data are also available for $C_1 - C_{12}$ binary mixtures. Delhommelle *et al.*[34] computed vapor-liquid coexistence curves with Configurational Bias Monte-Carlo ($CBMC$) simulations in the Gibbs ensemble. In this article performances of four different potential models were compared to each other at 374.03 K and at pressures up to 35 MPa. Their simulations predicted acceptable vapor-liquid phase equilibrium curves. An other simulation by Mackie *et al.*[35] was also performed at 374.05 K and at pressures up to 42 MPa. In this paper, phase compositions and densities predicted by the simulation are compared to experimental values reported in [36]. Overview of the articles of this mixture can be seen in table 1.1.

Moreover, the binary mixture of methane - tetradecane ($C_1 - C_{14}$) was also selected for this thesis, thus literature study was also conducted for this mixture. However, only one article was found, written by Nourozieh *et al.*[37]. In this article the phase composition, density and viscosity of saturated liquid phase were measured at pressures up to 10 MPa and at temperatures from 295 to 448 K. Overview of the articles of this mixture can be seen in table 1.2.

Furthermore, the binary mixtures of methane-icosane ($C_1 - C_{20}$) and methane-tetracosane ($C_1 - C_{24}$) were also selected as subject of this thesis. For icosane (C_{20}) Darwish *et al.*[41] reported experimental vapor-liquid phase equilibrium composition values at temperatures from 323 to 423 K and at pressures up to 10.7 MPa. They also compared results to values obtained from PR and SRK equations of state. Unfortunately, in their article density values are not reported which could have been useful for setting up simulations. For tetracosane (C_{24}) and methane binary system, experiments were also performed by Flöter *et al.*[42] at temperatures from 315 to 450 K and at pressures up to

Table 1.1: Literature review summary of $C_1 - C_{12}$ binary system

Mixture	$C_1 - C_{12}$			
Reference	[32]	[33]	[34]	[35]
	experiment	experiment	simulation	simulation
temperature range [K]	240 -315	273.1	374.03	374.05
pressure range [MPa]	up to 51	up to 10	up to 35	up to 42

Table 1.2: Literature review summary of $C_1 - C_{14}$ and $C_1 - Toluene$ binary systems

Mixture	$C_1 - C_{14}$	$C_1 - Toluene$		
Reference	[37]	[38]	[39]	[40]
	experiment	experiment	experiment	experiment
temperature range [K]	295 - 448	188 - 348	422.45 - 543.15	338.7
pressure range [MPa]	up to 10	up to 13	2 -25	up to 38

200 MPa and by Arnaud *et al.*[43] at temperature 374 K and at pressures up to 90 MPa. In the paper of Flöter vapor - liquid phase equilibrium compositions were reported, meanwhile Arnaud reported excess volumes and saturation pressures.Overview of the articles of this mixture can be seen in table 1.4.

Additionally, in order to assess the performance of the $TraPPE$ force field, not just for mixtures of methane and n-alkanes but for mixtures of methane with aromatic hydrocarbons as well, the methane - toluene binary mixture is also selected in this thesis. The literature study for this mixture revealed that Hughes *et al.*[38] performed measurements on this system at temperatures from 188 to 348 K and at pressures up to 13 MPa. They reported vapor - liquid phase equilibrium compositions. An article by Lin *et al.*[39] listed experimental vapor - liquid equilibrium composition data at temperatures from 422.45 to 543.15 K and at pressures from 2 to 25 MPa. Spencer *et al.*[40] performed experiments on methane-toluene binary system as well. They investigated and reported vapor - liquid phase equilibrium composition data at 338.7 K and at pressures from 0 to 38 MPa. Overview of the found articles of this mixture can be seen in table 1.2.

Table 1.3: Literature review summary of $C_1 - C_{16}$ binary system

Mixture	$C1 - C_{16}$				
Reference	[28]	[30]	[29]	[31]	[27]
	experiment	experiment	experiment	experiment	experiment
temperature range [K]	462.45 - 703.55	324 - 413.2	293.2 - 423.2	375 - 475	298 - 473
pressure range [MPa]	2 - 50	7 - 32	12 - 24	20 - 60	up to 120

Table 1.4: Literature review summary of $C_1 - C_{20}$ and $C_1 - C_{24}$ binary systems

Mixture	$C_1 - C_{20}$	$C_1 - C_{24}$	
Reference	[41]	[43]	[42]
	experiment	experiment	experiment
temperature range [K]	323 - 423	374	315 -450
pressure range [MPa]	up to 10.7	up to 90	up to 200

Dohrn *et al.*[44] organized the available articles of experiments into a paper to highlight the scarcity of the data. Overall, it can be said based on the thorough literature study that the available experimental or simulated vapor - liquid phase equilibrium reports and data are insufficient for proper parameter fitting purposes at different state points in order to obtain accurate vapor - liquid phase equilibrium and volumetric predictions from any equations of state for these mixtures.

The main aim of this work is to test the performance of the $TraPPE$ force field for the selected $C_1 - C_{12}$, $C_1 - C_{14}$, $C_1 - C_{16}$, $C_1 - C_{20}$, $C_1 - C_{24}$ and $C_1 - Toluene$ binary mixtures by providing new simulation data using Configurational Bias Monte Carlo[45–49] technique in the Gibbs ensemble at temperature between 400 K and 650 K and pressures up to 50 MPa. The new data are compared to calculations by $PC - SAFT$ equation of state at .

The secondary aim of this work is to provide new data to equation of state experts to adjust or determine accurate binary interaction parameters k_{ij} for these mixtures. These properly fitted new k_{ij} values would increase the accuracy of the phase and volumetric predictions of the different equations of state.

2

MONTE CARLO MOLECULAR SIMULATION

The first molecular simulations were performed in the early 1950's when computers became available for non-military use in the United States[19]. The availability of computers provided the possibility to scientists to solve problems that otherwise couldn't have been solved analytically. Monte Carlo technique was one among many others that was developed and used for simulations. Since then, it has become a vital part of most of the scientific research.

Monte Carlo can be generally applied for all simulations that utilize stochastic methods to generate new configurations of a system of interest. The concept of any Monte Carlo simulation starts with an initial configuration of particles in a system. Then, trial moves are attempted in order to change the configuration of the system. A move is accepted or rejected based on an acceptance criterion. This criterion must guarantee that the configurations are sampled with correct weights and the configurations are sampled from a statistical mechanics ensemble distribution as well. Once a move was accepted or rejected, the property of interest is calculated. After many moves, an average value of the equilibrium thermodynamic property of interest can be obtained[50]. The most important condition that every Monte Carlo method must fulfill is the detailed balance condition.

2.1. DETAILED BALANCE

As it was mentioned before, Monte Carlo simulations consist of different trial moves. Once a move is attempted and accepted, a new system configuration s_n is formed. In order to satisfy the detailed balance condition (eq.(2.3)), this new system configuration must not change the equilibrium distribution of system states[19, 51]. When an infinite simulation is considered, the number of moves, which changes the system from the old configuration to the new configuration (eq.(2.1)) must be equal to the number of moves, which transforms the system back from the new configuration to the old configuration (eq.(2.2)).

$$\begin{aligned}
K(s_o \rightarrow s_n) &= \mathcal{N}(s_o) \cdot \alpha(s_o \rightarrow s_n) \cdot acc(s_o \rightarrow s_n) \qquad (2.1)\\
K(s_n \rightarrow s_o) &= \mathcal{N}(s_n) \cdot \alpha(s_n \rightarrow s_o) \cdot acc(s_n \rightarrow s_o) \qquad (2.2)\\
K(s_o \rightarrow s_n) &= K(s_n \rightarrow s_o) \qquad (2.3)
\end{aligned}$$

In the equations above $K(s_o \rightarrow s_n)$ stands for the number of moves from the old configuration to the new configuration, $K(s_n \rightarrow s_o)$ represents the number of moves from the new configuration back to the old configuration, s_o being the old configuration of the system, while s_n is the new configuration of the system. Furthermore, $\mathcal{N}(s_o)$ stands for the probability of finding a system in the old configuration, $\mathcal{N}(s_n)$ stands for probability of finding a system in the new configuration, $\alpha(s_o \rightarrow s_n)$ being the probability of performing a trial move from the old configuration to the new, $\alpha(s_n \rightarrow s_o)$ stands for the probability of performing a trial move from the new configuration to the old, $acc(s_o \rightarrow s_n)$ being the acceptance probability of a move from the old configuration to a new and $acc(s_n \rightarrow s_o)$ stands for the acceptance probability of a move from the new configuration to the old.

2.2. BOUNDARY CONDITIONS

Monte Carlo simulations aim to provide macroscopic properties of the phases in the bulk regions. In order to achieve this, it is fundamental to employ a boundary condition that simulates the presence of an infinite bulk surrounding of the system. For this purpose, periodic boundary condition is applied. It means that the simulated region is surrounded by its own identical images and the surrounding images simultaneously contain the same amount of molecules as the main region and the position of the constituent molecules are also identical to the main region. The representation of this boundary condition can be seen in fig. 2.1 on the example of region II.

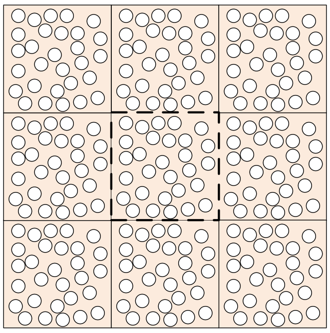

Figure 2.1: 2D Representation of the periodic boundary condition

2.3. ENSEMBLES

Molecular simulations work on the molecular level, which means that the most fundamental information gained from the simulated system are the possible structures of the system constructed by its constituent molecules and the intermolecular potentials of the system[52] in those different configurations. However, the goal of any molecular simulation is to gain macroscopic thermodynamic properties, such as entropy (S) or Gibbs free energy (G) of the simulated system based on its molecular, microscopic properties.

If an arbitrary macroscopic system is considered, it can be specified with a few macroscopic parameters, such as pressure (P), volume (V), temperature (T) or chemical potential (μ). In contrast, at molecular level there are large number of quantum states, different configurations that describe the same macroscopic system with those fixed parameters. As long as, the arbitrarily selected macroscopic system is isolated (fixed N, V and E) any macroscopic thermodynamic property of the macroscopic system can be calculated as the ensemble average of the corresponding property[53]. However, most of the molecular simulations are performed in non-isolated ensemble. In this thesis the most commonly used ensemble is the NPT ensemble. In this ensemble the link that makes any macroscopic thermodynamic property calculation possible is the so called partition function, which relates the available quantum mechanical energy levels of an N-body system to its thermodynamic properties considering the probability of occurrence of those energy levels.

2.4. GIBBS ENSEMBLE

The purpose of this section is to introduce the Gibbs ensemble Monte Carlo computer simulation technique[54], which is widely used for phase equilibrium calculations and was extensively employed in the present work. The reason for the popularity of this technique originates in its simplicity and in the fact that it is computationally inexpensive. It does not require the prior specification of the chemical potentials[55] and it also places minimal demand on the user in terms of information of the approximate phase diagram[56]. An other important benefit of this technique is the fact that it is easy to code. All simulations in this thesis were performed by an open source molecular simulation software (*RASPA*[57]). This employed software has the capability of handling the Gibbs ensemble and many more. Examples for *RASPA* simulation input files in the Gibbs ensemble can be found in Appendix-C and in Appendix-D.

The Gibbs ensemble technique's principle is the following. In this method a macroscopic system is given, which can be seen in fig. 2.2. Within this macroscopic system there are two microscopic regions, one in the liquid phase and one in the vapor phase. These regions are located in the bulk, far away from the vapor-liquid interface. A macroscopic system is in thermal equilibrium if the temperature (T), pressure (p) and chemical potentials (μ) of all the species (α) are the same[56] in both regions (I, II). See equations below.

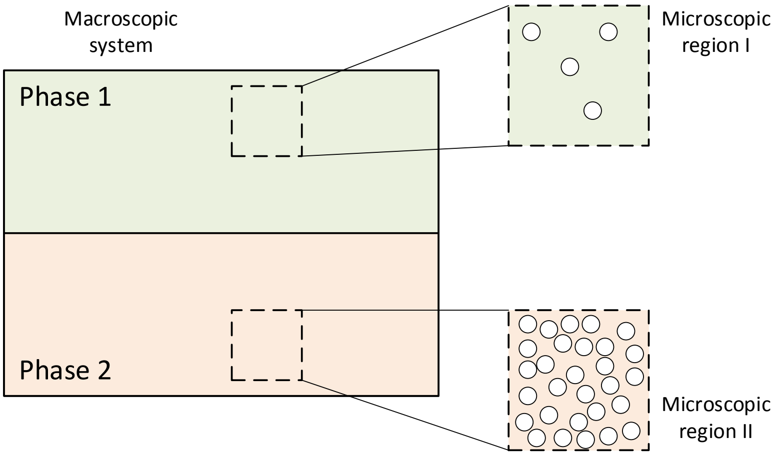

Figure 2.2: Schematic diagram of the Gibbs ensemble system

$$p_I = p_{II} \tag{2.4}$$
$$T_I = T_{II} \tag{2.5}$$
$$\mu_I^\alpha = \mu_{II}^\alpha \tag{2.6}$$

Furthermore, each microscopic region must be in internal equilibrium as well. In Gibbs ensemble Monte Carlo simulations the system temperature is a predefined property. The rest of the previously mentioned conditions are satisfied via different system moves.

2.4.1. MONTE CARLO MOVES IN THE GIBBS ENSEMBLE

PARTICLE DISPLACEMENT

The internal equilibrium condition is satisfied via random displacement trial moves of a random molecule within each region. During an attempted displacement move, a random displacement vector is given to all beads of the selected molecule. The schematic representation of a displacement trial move can be seen in fig. 2.3.

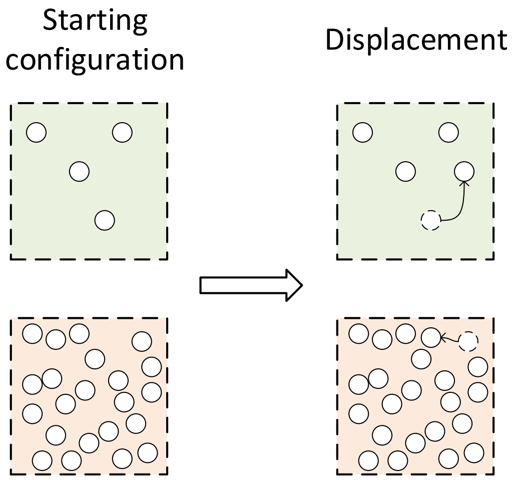

Figure 2.3: Schematic diagram of a random displacement move

VOLUME CHANGE

The equilibrium of pressures (eq. (2.7)) between the two microscopic regions is reached by attempting random volume change trial moves. When this trial move is attempted, a random ΔV volume change is given to the volume of the selected microscopic region. Based on the employed ensemble, the volume changes of the regions can be coupled or decoupled. The schematic representation of a volume change trial move can be seen in fig. 2.4.

$$p_I = p_{II} \tag{2.7}$$

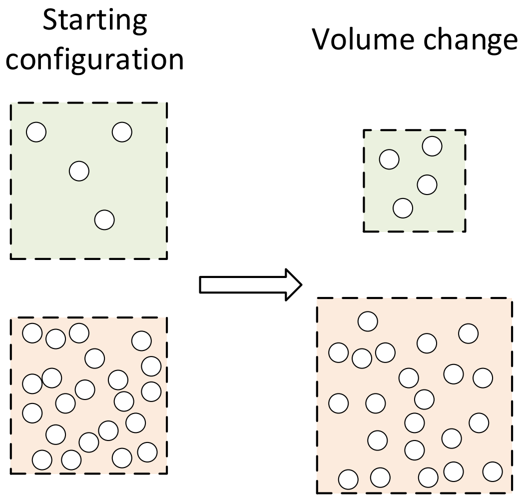

Figure 2.4: Schematic diagram of a volume change move

PARTICLE EXCHANGE

When this trial move is attempted, a random particle is selected from one of the two regions. The selected particle is deleted from its original region and then it is inserted back to a random location of the other region. The schematic representation of a particle exchange trial move can be seen in fig. 2.5. By employing the exchange trial moves of particles, the equality of chemical potentials for all components between the two microscopic region can be satisfied.

$$\mu_I^\alpha = \mu_{II}^\alpha \tag{2.8}$$

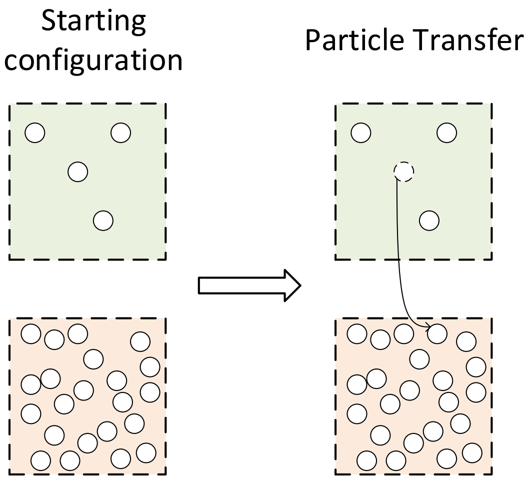

Figure 2.5: Schematic diagram of a particle exchange move

2.4.2. MONTE CARLO IN THE NVT GIBBS ENSEMBLE

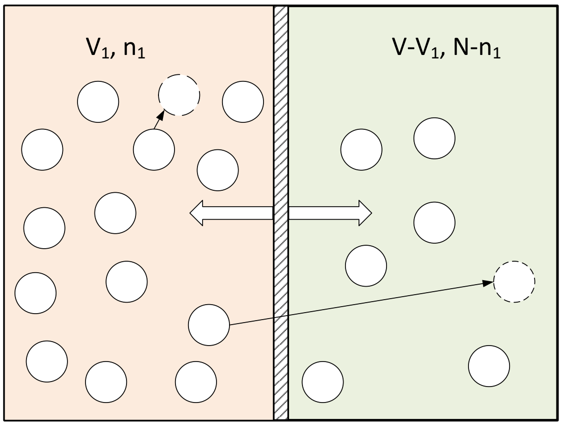

Figure 2.6: Schematic representation of the NVT ensemble

The constant total number of particles (N), constant total volume (V) and constant temperature (T) ensemble is used for simulating one-component systems. The total volume (V) of the system is divided between the two microscopic regions, such as the sum of the volume of region I (V_I) and the volume of region II (V_{II}) is $V = V_I + V_{II}$. The same applies for the total number of particles (N), $n_{II} = N - n_I$, where n_{II} stands for the number of particles in region II and n_I indicates the number of particles in region I. In the Gibbs ensemble the partition function (Q_{NVT}) is given by eq. (2.9)[19].

$$Q_{NVT} = \sum_{n_I=0}^{N} \frac{1}{\Lambda^{3N}\cdot V \cdot n_I! \cdot (N-n_I)!} \cdot \int_0^V dV_I \cdot dV_I^{n_I} \cdot (V-V_I)^{N-n_I} \\ \times \int ds_I^{n_I} \cdot exp\left[-\beta \cdot \mathcal{U}\left(s_I^{n_I}\right)\right] \cdot \int ds_{II}^{N-n_I} \cdot exp\left[-\beta \cdot \mathcal{U}\left(s_{II}^{N-n_I}\right)\right] \tag{2.9}$$

In eq. (2.9) λ indicates the thermal de Broglie wavelength, $s_I^{n_I}$ stands for the scaled coordinates of particles in region I, $\mathcal{U}\left(s_I^{n_I}\right)$ is the potential energy of region I based on the positions of all particles in region I, $s_{II}^{N-n_I}$ indicates the scaled coordinates of particles in region II, $\mathcal{U}\left(s_{II}^{N-n_I}\right)$ stands for the potential energy of region II based on the positions of all particles in region II.

The probability that the system can be found in configuration with certain number of particles (n_I) in certain volume (V_I) and with positions $\left(s_I^{n_I}\ and\ s_{II}^{N-n_I}\right)$ is given by the probability density function $\left(\mathcal{N}\left(n_I, V_I, s_I^{n_I}, s_{II}^{N-n_I}\right)\right)$ of this ensemble. The probability density function is an essential function in order to determine the acceptance probabilities of the different system moves in this NVT ensemble. For a random displacement trial move in one of the regions the probability of acceptance can be expressed by eq. (2.10)[19].

$$acc\,(o \rightarrow n)_{disp} = min\left[1, exp\left[-\beta \cdot \left[\mathcal{U}\left(s_n^{n_I}\right) - \mathcal{U}\left(s_o^{n_I}\right)\right]\right]\right] \tag{2.10}$$

In eq. (2.10) the $\left[\mathcal{U}\left(s_n^{n_I}\right) - \mathcal{U}\left(s_o^{n_I}\right)\right]$ term represents the configurational potential energy change, from the old configuration $\mathcal{U}\left(s_o^{n_I}\right)$ to the new configuration $\mathcal{U}\left(s_n^{n_I}\right)$ which is resulted by a random displacement of a randomly selected molecule. In the NVT ensemble the total system volume is a fixed parameter. It means that any volume change move of any region immediately results an inverse, but in magnitude equal volume change of the other microscopic region.

$$\Delta V_I = -\Delta V_{II} \tag{2.11}$$

$$-\Delta V_I = \Delta V_{II} \tag{2.12}$$

The acceptance probability for a volume change trial move in which the volume of the region I increases with ΔV and the volume of region II decreases with ΔV is given by eq. (2.13)[19]. Superscript n stands for new, while superscript o stands for old.

$$acc\,(o \rightarrow n)_{vol} = min\left[1, \left(\frac{V_I^n}{V_I^o}\right)^{n_I+1} \cdot \left(\frac{V - V_I^n}{V - V_I^o}\right)^{N-n_I+1} \times exp\left[-\beta \cdot \left[\mathcal{U}\left(s_n^N\right) - \mathcal{U}\left(s_o^N\right)\right]\right]\right] \tag{2.13}$$

Last, but not least the probability of acceptance for an exchange move in which a random molecule is selected from region I and transferred to region II is given by eq. (2.14)[19].

$$acc\,(o \rightarrow n)_{exchange} = min\left[1, \left(\frac{n_I \cdot (V - V_I)}{(N - n_I + 1) \cdot V_I}\right) \cdot exp\left[-\beta \cdot \left[\mathcal{U}\left(s_n^N\right) - \mathcal{U}\left(s_o^N\right)\right]\right]\right] \tag{2.14}$$

2.4.3. MONTE CARLO IN THE NPT GIBBS ENSEMBLE

In this thesis for every simulation the NPT ensemble is used due to the fact that most of the time the experiments are performed at constant temperature (T) and at constant pressure (P) conditions. A visual representation of this ensemble can be seen in fig. 2.7. The system has volume V and it is separated from a reservoir of ideal gas with volume V_{res}. The restriction that must be applied is that the total volume of the ensemble V_0 is the sum of the volume of the system V and the volume of the reservoir V_{res}.

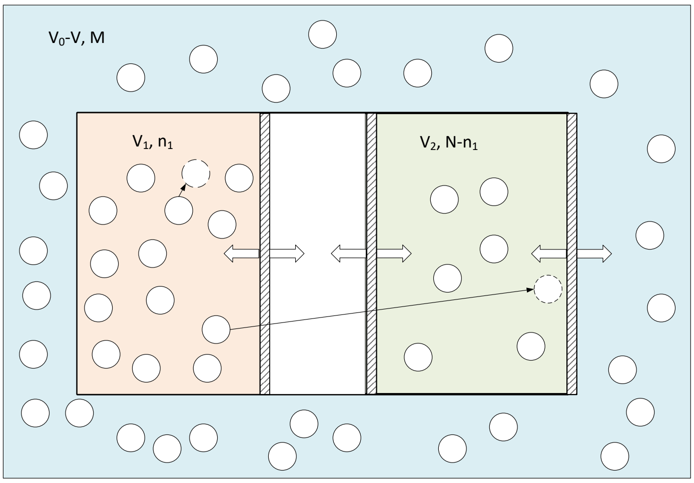

Figure 2.7: Schematic representation of the Isobaric-Isothermal ensemble

$$V_0 = V + V_{res} \tag{2.15}$$

For simplicity the system is assumed to be constructed by identical atoms. After considering this simplification the partition function (eq. (2.16)) for this ensemble is described as [19].

$$Q_{NPT} = \frac{\beta \cdot P}{\Lambda^{3N} \cdot N!} \cdot \int dV V^N \cdot exp\left(-\beta \cdot P \cdot V\right) \cdot \int ds^N \cdot exp\left[-\beta \cdot \mathscr{U}\left(s^N\right)\right] \tag{2.16}$$

Compared to the NVT ensemble there is a major difference among the trial moves. In the NPT ensemble the volume changes of the two regions are not coupled together anymore. It means that the volumes of the regions can change separately, the change of a volume of a region does not affect the volume change of the other region. For a volume change trial move the acceptance probability in the NPT ensemble is described by eq. (2.19)[58].

$$\Delta\mathscr{U}_I = \mathscr{U}_I\left(s_n^{n_I}\right) - \mathscr{U}_I\left(s_o^{n_I}\right) \tag{2.17}$$

$$\Delta\mathscr{U}_{II} = \mathscr{U}_{II}\left(s_n^{N-n_I}\right) - \mathscr{U}_{II}\left(s_o^{N-n_I}\right) \tag{2.18}$$

$$\begin{aligned} acc\left(o \to n\right)_{vol} = min\Bigg[1, \Bigg[exp\Bigg[-\beta\Bigg(\cdot\Delta\mathscr{U}_I + \Delta\mathscr{U}_{II} - n_I \cdot k \cdot T \cdot ln\frac{V_I + \Delta V_I}{V_I} \\ -\left(N - n_I\right) \cdot k \cdot T \cdot ln\frac{V_{II} + \Delta V_{II}}{V_{II}} + P \cdot \left(\Delta V_I + \Delta V_{II}\right)\Bigg)\Bigg]\Bigg]\Bigg] \end{aligned} \tag{2.19}$$

2.5. ADVANCED TECHNIQUES

2.5.1. CONFIGURATIONAL BIAS MONTE CARLO

Configurational Bias Monte Carlo[45–49] is an advanced simulation technique to simulate systems which contain long chain molecules. When such systems are simulated with traditional Monte Carlo most of the attempted system moves are rejected. The reason behind these rejections is the fact that it is difficult to find empty space where a long molecule would fit into without overlapping with others. The result of the increased amount of rejections during simulation is that the system does not converge, cannot reach equilibrium or if it could, it would require too much simulation time.

The principle of this method is that the randomly selected long chain molecule is reconstructed bead-by-bead during the attempted move. During the reconstruction process a trial direction from many, with equal probabilities, is selected for each bead reconstruction attempt. If the reconstructed bead does not overlap with any other component that trial direction is accepted and then the bead is inserted into that position. On the other hand, when a molecule reconstruction is failed due to component overlapping in that selected trial position, the recent bead is deleted from the system and a new reconstruction random trial direction is attempted from the most recent successfully inserted bead. The whole process is repeated until the molecule is fully reconstructed. The schematic view of this process can be seen in fig. 2.8.

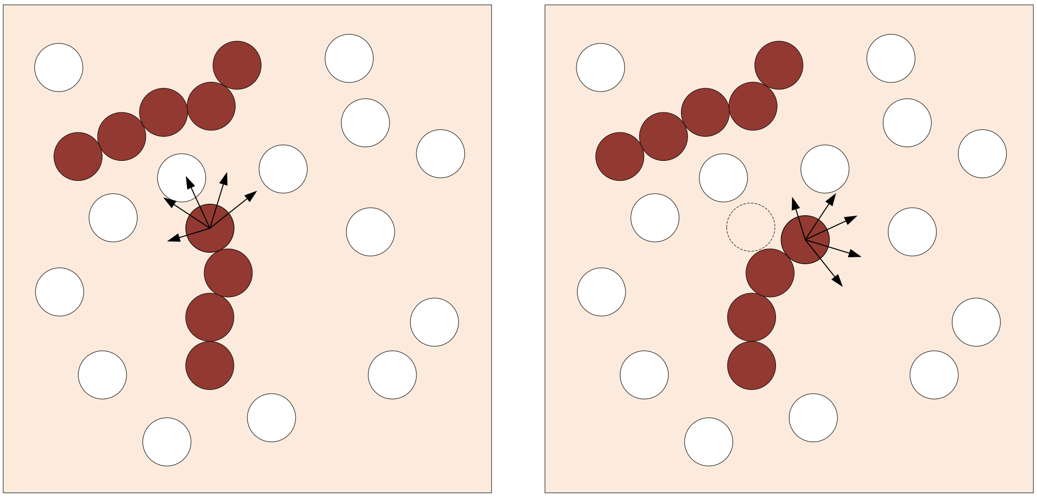

Figure 2.8: Schematic representation of the CBMC technique

2.5.2. Continuous Fractional Component Monte Carlo

An other simulation technique created in order to increase the acceptance probabilities of the different attempted moves for simulation of systems with long molecules or high densities is the so called Continuous Fractional Component Monte Carlo ($CFCMC$) technique[59–62]. Beside the fact that this technique improves the acceptance probabilities, it directly reports the chemical potential of each component in each simulation box. This feature serves as a convenient way to check if the system is in equilibrium.

This method applies fractional molecules. These fractional molecules have scaling parameter (λ) between 0 and 1. This scaling parameter influences the Lennard-Jones interactions of these fractional molecules according to eq. (2.20) by [62].

$$\mathcal{U}_{LJ}\left(r_{ij},\lambda\right) = \lambda \cdot 4 \cdot \epsilon_{ij} \cdot \left[\frac{1}{\left(\frac{1}{2}\cdot(1-\lambda)^2 + \left(\frac{r_{ij}}{\sigma_{ij}}\right)^6\right)^2} - \frac{1}{\left(\frac{1}{2}\cdot(1-\lambda)^2 + \left(\frac{r_{ij}}{\sigma_{ij}}\right)^6\right)} \right] \tag{2.20}$$

During this technique a single fractional molecule per component is present in one of the simulation boxes. Besides the trial move for thermal equilibration and the normal Gibbs ensemble trial moves, three other types of move are attempted in this method. The first extra move tries to change the scaling factor (λ) of the fractional molecule. By doing so, it manipulates the interaction of the fractional molecule with the surrounding based on eq. (2.20). The second and third additional trial moves attempt to transfer the fractional molecule between the simulation boxes. The second move is called swap move and it attempts to swap a fractional molecule between the simulation boxes. The third move is called identity change move. This attempted move randomly selects a whole molecule and a fractional molecule with scaling factor (λ). The only restriction during this move is that the selected whole molecule and fractional molecule should be in the opposite simulation box. Then the whole molecule is transformed into a fractional molecule while inheriting the scaling factor of the selected fractional molecule and at the same time, the fractional molecule will become a whole molecule, identical to the selected one in case of multicomponent systems. These moves are illustrated in fig. 2.9.

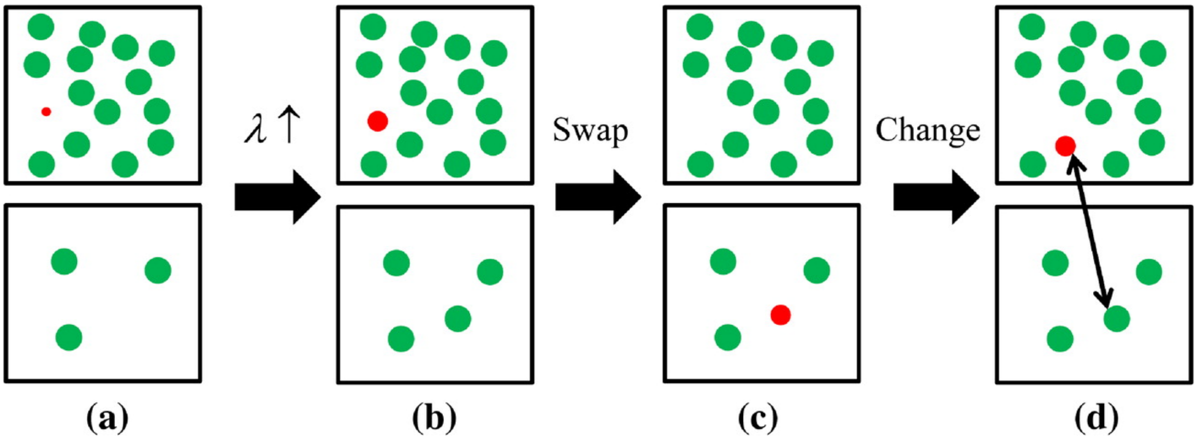

Figure 2.9: Schematic representation of the additional trial moves in CFCMC GE[59, 60]. The red sphere is the fractional molecule and the green spheres are the whole molecules. (a)→(b): changing the scaling parameter with . (b)→(c): swapping the fractional molecule between the boxes. (c)→(d): changing the identity of the fractional molecule with a randomly selected whole molecule in the other simulation box, while keeping the value of constant.

3

MOLECULAR FORCE FIELD

In the previous chapter, the fundamentals of the Monte Carlo simulations were introduced. However, the Monte Carlo methods are only the framework of the simulations. A prerequisite for any successful molecular simulation is the accurate description of the intra- and inter-molecular interactions in the system.

In order to describe the molecular interactions, different force fields were developed in the last decades. Usually two different approaches are considered for dividing the molecules into interaction sites[22]. The first approach treats each carbon and hydrogen atom as an individual interaction site[63]. This is a more realistic concept, although it is computationally expensive[22] due to the large number of interaction sites. The second approach combines the carbon and its bonded hydrogen atoms[64] into a pseudoatom. These formed pseudoatoms (CH_4, CH_3, CH_2, CH and C) are considered as single interaction sites[22]. In this way the number of interaction sites are reduced significantly, thus the required computational burden[22].

3.1. LENNARD-JONES PAIR POTENTIAL

A popular choice to describe the interactions between the interaction sites is the Lennard-Jones[51] pair potential model (eq. (3.1)).

$$\mathscr{U}_{LJ}\left(r_{ij}\right) = 4\cdot\epsilon_{ij}\cdot\left[\left(\frac{\sigma_{ij}}{r_{ij}}\right)^{12} - \left(\frac{\sigma_{ij}}{r_{ij}}\right)^{6}\right] \tag{3.1}$$

In eq. (3.1) $\mathscr{U}_{LJ}\left(r_{ij}\right)$ indicates the interaction energy between interaction sites at distance r_{ij}, ϵ_{ij} stands for the well-depth Lennard-Jones parameter between interaction sites, σ_{ij} indicates the Lennard-Jones diameter parameter between interaction sites, r_{ij} is the distance between interaction site i and j. In eq.(3.2) σ_i and σ_j indicate the Lennard-Jones diameter parameter for interaction sites i and j. In eq.(3.3) ϵ_i and ϵ_j stand for the Lennard-Jones well-depth parameter for interaction sites i and j.

In this description the parameters for the dissimilar interaction sites are calculated by the classical Lorentz-Berthelot combining rules (eq.(3.2),(3.3)) without binary interaction parameter k_{ij}.

$$\sigma_{ij} = \frac{1}{2}\cdot\left(\sigma_i + \sigma_j\right), \tag{3.2}$$

$$\epsilon_{ij} = \left(\epsilon_i\cdot\epsilon_j\right)^{\frac{1}{2}}, \tag{3.3}$$

The interaction sites attract each other at large distances. This area is indicated with green color in fig. 3.1. At short distances, the interaction sites repel each other. The corresponding area for this type of interaction is highlighted with red color in fig. 3.1. On the x-axis where the value of the interaction energy is equal to 0 the attractive and repulsive van der Waals forces cancel each other, there is no interaction between the interaction sites. The deepest point of the energy well ϵ_{min} indicates the point where the interaction between the sites are the most attractive. For this interaction energy, there is a corresponding most favorable distance between the sites which is indicated by σ_{min}.

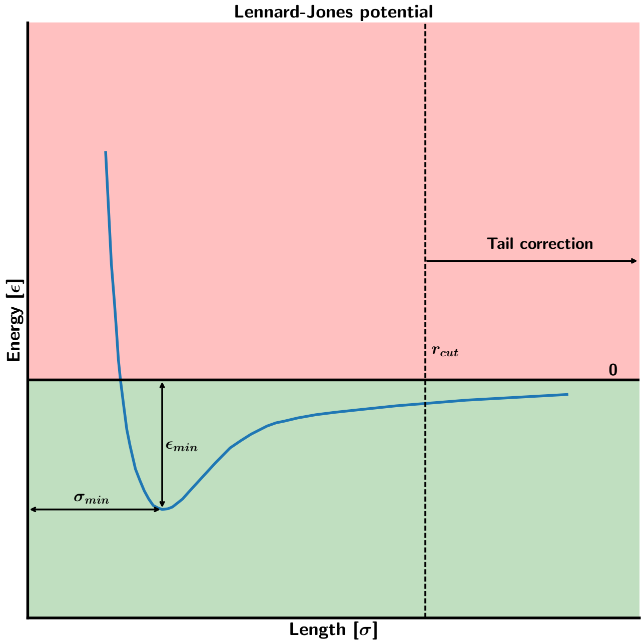

Figure 3.1: Lennard-Jones pair potential model

Truncation of the Lennard-Jones potential is usually applied in molecular simulations in order to reduce the computational burden. Simple truncation is one of the most popular truncation in simulations and it is used in this thesis as well. In this method, if the distance between the interacting sites are larger than r_{cut}, the Lennard-Jones potentials (u^{lj}) for the interactions are not calculated (eq. (3.4)).

$$u^{trunc}(r) = \begin{cases} u^{lj}(r) & r \leq r_{cut} \\ 0 & r > r_{cut} \end{cases} \tag{3.4}$$

In this description, the potential change at r_{cut} is discontinuous. This feature makes the simple truncation method not suitable for Molecular Dynamics simulations, but it can be used for Monte Carlo simulations[19]. An other feature of any truncation is that it introduces a systematic error in the nonbonded potential energy calculations. This error can be compensated by applying an analytical tail correction function. This analytical tail correction function adds the approximate potential of the neglected long range interactions $\mathscr{U}_{tail}$ to the nonbonded potentional energy term $\mathscr{U}_{nonbonded}$ of the molecular potential energy $\mathscr{U}_{molecule}$(eq. (3.14)). The applied energy tail correction function for this Lennard-Jones potential can be seen in eq. (3.5)[19].

$$\mathscr{U}^{tail} = \frac{8}{3} \cdot \pi \cdot \epsilon_{ij} \cdot \rho \cdot \sigma_{ij}^3 \cdot \left[\frac{1}{3} \cdot \left(\frac{\sigma_{ij}}{r_{cut}} \right)^9 - \left(\frac{\sigma_{ij}}{r_{cut}} \right)^3 \right] \tag{3.5}$$

3.2. FORCE FIELDS

Over the decades, multiple force fields were developed to describe the intra- and inter-molecular interactions. *AMBER*[25, 26, 65–67] is a collection of programs and force fields that allow users to perform molecular simulations, particularly on bio-molecules. The development of the package started in the early 1980's[66]. Since then, due to parametrization efforts different force fields were created in order to match the simulated data to experiments for the different bio-molecules. For example, the outcome of this efforts are the AMBER ff98 nucleic acid force field and the ff99-bsc0 force field. The *OPLS* force field, proposed by Jorgensen *et al.*[20], yields accurate liquid densities and heat of vaporization but only for short *n*-alkanes. In the *OPLS* force field the ethane's methyl group Lennard-Jones parameter of diameter $\sigma_{CH_3}^{ethane}$ is different from any other *n*-alkane's methyl group diameter parameter σ_{CH_3} and the diameter parameter of the methylene group σ_{CH_2} is identical to the methyl group's diameter parameter in case of any *n*-alkanes except ethane (eq.(3.6)). In this force field description the well-depth parameter is different for methylene ϵ_{CH_2} and for methyl groups ϵ_{CH_3} for any *n*-alkanes, additionally, the methyl's group well-depth parameter is also different in case of ethane $\epsilon_{CH_3}^{ethane}$ compared to any other *n*-alkane's well-depth parameter ϵ_{CH_3} (eq.(3.7)).

$$\sigma_{CH_3}^{ethane} \neq \sigma_{CH_3} = \sigma_{CH_2} \tag{3.6}$$

$$\epsilon_{CH_3}^{ethane} \neq \epsilon_{CH_3} \neq \epsilon_{CH_2} \tag{3.7}$$

The drawback of this force field is that it overestimates the critical temperatures of medium and long *n*-alkanes[22]. In order to solve the problems of the *OPLS* force field, the *SKS* force field[21] was developed. The positive result of this new force field is that it returns improved vapor-liquid phase equilibrium results for medium and long chain *n*-alkanes[22]. However, the weakness of this new force field is that it yields overestimated critical temperatures for short *n*-alkanes. The reason behind this outcome is that the *SKS* force field utilizes the same Lennard-Jones diameter parameters for methylene and for methyl groups regardless the type of *n*-alkane (eq.(3.8)), nevertheless it uses different well-depth parameters for these groups (eq.(3.9)).

$$\sigma_{CH_3} = \sigma_{CH_2} \tag{3.8}$$

$$\epsilon_{CH_3} \neq \epsilon_{CH_2} \tag{3.9}$$

3.2.1. TRAPPE

TraPPE[22–24, 68] was developed in the last decades in order to improve the vapor-liquid phase equilibria calculations of the existing force field models, such as *OPLS*[20] or *SKS*[21], mainly for hydrocarbons. The major improvement of the *TraPPE* force field is that it applies different diameter and well-depth Lennard-Jones parameters for the methyl and methylene groups (eq.(3.10,3.11)). This change resulted in accurate descriptions of vapor-liquid coexistence curves and critical properties of linear alkanes from methane to dodecane. On the other hand, a small deviation from experimental results were observed for vapor densities and pressures[22].

$$\sigma_{CH_3} \neq \sigma_{CH_2} \tag{3.10}$$

$$\epsilon_{CH_3} \neq \epsilon_{CH_2} \tag{3.11}$$

In this work *TraPPE* is the selected force field for simulations. Firstly, the article reviews ([22–24, 68]) of the *TraPPE* force field revealed that accurate vapor-liquid phase equilibrium predictions can be achieved for pure *n*-alkanes and for some binary mixtures of *n*-alkanes by employing this force field. Secondly, this force field is not tested yet for the selected binary mixtures of light/heavy hydrocarbons that are the interest of this thesis.

Furthermore, $TraPPE$ force field will be applied with united atom description in this work. The potential energy of a molecule $\mathscr{U}_{molecule}$ is built up from the energy of the bonded $\mathscr{U}_{bonded}$ and nonbonded $\mathscr{U}_{nonbonded}$ interactions (eq. (3.12)).

$$\mathscr{U}_{molecule} = \mathscr{U}_{bonded} + \mathscr{U}_{nonbonded} \tag{3.12}$$

Bonded interactions are those that involve pseudoatoms that are not separated by more than three bonds and belong to the same molecule. On the other hand, the nonbonded interactions are those interactions which involve pseudoatoms that are separated by at least four bonds or belong to different molecules. The overall potential energy of the simulated system $\mathscr{U}_{system}$ is the sum of the potential energies of the constituent molecules of the system(eq. (3.13)).

$$\mathscr{U}_{system} = \sum_{i=0}^{n} \mathscr{U}_{molecule} \tag{3.13}$$

NONBONDED INTERACTIONS

The Lennard-Jones pair potential parameters of the $TraPPE$ force field for the relevant pseudoatoms of alkanes can be seen in table 3.1. The charge of these individual pseudoatoms are 0 in the TraPPE force field description. This means that the Coulomb interaction term in eq. (3.1) can be neglected, due to that fact that its contribution to the nonbonded potentials are 0.

Furthermore, according the work of Siepmann *et al.*[22], the applied value of the cut-off radius is always $r_{cut} = 14$ $\AA$ in case of $TraPPE$ force field.

$$\mathscr{U}_{nonbonded} = \mathscr{U}_{LJ}\left(r_{ij}\right) + \mathscr{U}^{tail} \tag{3.14}$$

Pseudoatom	$\epsilon/k_B[K]$	$\sigma[\AA]$	q[e]
CH_3	98	3.75	0
CH_2	46	3.95	0
CH	48	3.74	0
C	21	3.88	0

Table 3.1: Lennard-Jones pair potential parameters for TraPPE force field[69]

BONDED INTERACTIONS

Bond-stretching potential The resulted potential when a bond stretches and contracts is described by a harmonic oscillator (eq. (3.15)) equation in the $TraPPE$ force field.

$$\mathscr{U}_{bond} = \frac{1}{2} \cdot k \cdot (r - r_0)^2 \tag{3.15}$$

In eq. (3.15) k is the force constant, r is the length of the bond and r_0 is the reference length of the bond. $TraPPE$ force field, just like $OPLS$ and SKS, applies a fix bond length between pseudoatoms. In $TraPPE$ this fixed bond length is 1.54 $\AA$[22]. In order to maintain the fixed lengths between interaction sites, constraint algorithms are used. These algorithms solve Newton's second law. In $RASPA$, these applied constraint algorithms are the $SHAKE$ and $RATTLE$ algorithms[57]. The constraint of applying fixed bond lengths in these previously mentioned force fields increases the computational efficiency, thus the simulations are faster.

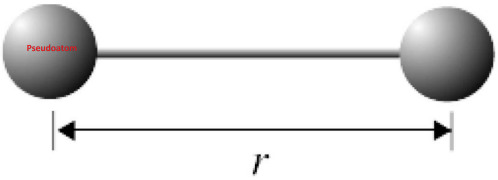

Figure 3.2: Representation of bond stretching

Bending potential $TraPPE$ force field applies harmonic potential[57] description to calculate the bending potential(eq. (3.16)).

$$\mathscr{U}_{bend}(\theta) = \frac{1}{2} \cdot k_\theta \cdot (\theta - \theta_0)^2 \tag{3.16}$$

In eq. (3.16) k_θ is the bending potential constant with value of 62500 $\frac{K}{rad^2}$, the θ_0 is the reference angle between the bonds which is 114°, in case of $TraPPE$ force field and the θ represents the actual angle between the bonds during simulations.

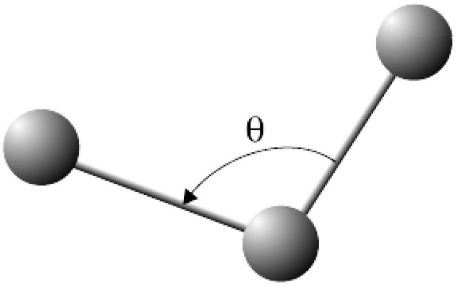

Figure 3.3: Representation of bond bending

Torsional potential In order to calculate the molecular energy change that occurs during intramolecular rotation around bonds, conformational changes, $TraPPE$ applies the TraPPE-dihedral equation[57], which is presented in eq. (3.17). In this equation c_0, c_1, c_2 and c_3 are constants and their values can be seen in table 3.2. ϕ indicates the dihedral angle.

$$\mathscr{U}_{torsion}(\phi) = c_0 + c1 \cdot (1 + cos\phi) + c_2 \cdot (1 - cos(2 \cdot \phi)) + c_3 \cdot (1 + cos(3 \cdot \phi)) \tag{3.17}$$

Constants	Values [K]
c_0	0
c_1	355.03
c_2	-68.19
c_3	791.32

Table 3.2: Torsion potential constants for TraPPE[69]

Overall, it can be said that in the $TraPPE$ force field description the total molecular energy $\mathscr{U}_{molecule}$ is built up from the Lennard-Jones potential, the tail correction, the bending potential and from the torsional potential terms (eq. (3.18)).

$$\mathscr{U}_{molecule} = \mathscr{U}_{LJ}(r_{ij}) + \mathscr{U}^{tail} + \mathscr{U}_{bend}(\theta) + \mathscr{U}_{torsion}(\phi) \tag{3.18}$$

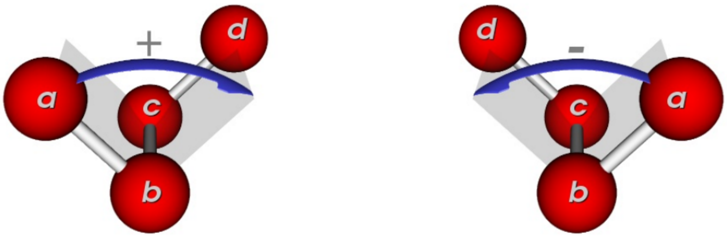

Figure 3.4: Representation of the dihedral angle in the torsinal potential equation[57]

4

RESULTS AND DISCUSSION

In this chapter the Monte Carlo simulation results for vapor-liquid phase equilibrium and volumetric predictions of the binary mixtures of methane-dodecane ($C_1 - C_{12}$), methane-tetradecane ($C_1 - C_{14}$), methane-hexadecane ($C_1 - C_{16}$), methane-icosane ($C_1 - C_{20}$), methane-tetracosane ($C_1 - C_{24}$) and methane-toluene ($C_1 - Toluene$) are presented.

During the simulation phase, four simulations per state point were performed for the methane-dodecane, methane-tetradecane, methane-toluene and for the methane-hexadecane binary systems. For the methane-icosane and methane-tetracosane binary systems, this was increased to six simulations per state point. Moreover, 15000 to 35000 equilibration cycles and 20000 to 50000 production cycles were used for the simulations of the different binary mixtures. The total number of particles in the system per simulation ranges from 800 to 1500. The standard deviation (x_{std}) of the simulation results was calculated by eq. (4.2).

$$\overline{x} = \frac{\sum_{i=1}^{N} x_i}{N} \tag{4.1}$$

$$x_{std} = \sqrt{\frac{1}{N} \cdot \sum_{i=1}^{N} \left(x_i - \overline{x}\right)^2} \tag{4.2}$$

In eq. (4.2) N stands for the number of simulations per state point, x_i being the value of property of the interest of the simulation and $\overline{x}$ stands for the average value of the property of interest of the simulations.

In order to assess the performance of the $TraPPE$ force field for these binary mixtures, multiple simulations in the Gibbs ensemble were performed at different state points. Firstly, the simulated results were validated against experimental data. Then, simulations for these mixtures were performed at extrapolated state points, covering the range of $400 - 650\ K$ and $5 - 50\ MPa$.

In this work the presented $PC-SAFT$ predictions were received from a collaborating research group led by Professor Ioannis Economou (Texas A & M University at Qatar and NCSR Demokritos). The used $PC - SAFT$ input parameters, such as number of segments m, segment diameter σ and segment energy ϵ for their equation of state calculations can be seen in table 4.1.

If the reliability of the simulated results by Monte Carlo proved to be valid, this work would also provide the possibility to determine or to refit the binary interaction parameters k_{ij} applied in the $PC - SAFT$ equation of state calculations (table 4.2).

component	m	$\sigma\,[\mathring{A}]$	$\epsilon/k_B\,[K]$
C_1	1	3.7039	150.03
$n-C_{12}$	5.306	3.8959	249.21
$n-C_{14}$	5.9002	3.9396	254.21
$n-C_{16}$	6.6485	3.9552	254.7
$n-C_{20}$	7.9849	3.9869	257.75
$n-C_{24}$	9.6836	3.9709	254.69

Table 4.1: Applied PC-SAFT parameters [70]

mixture	C_1–C_{12}	C_1-C_{14}	C_1–C_{16}	C_1–C_{20}	C_1–C_{24}
k_{ij}	0.0103	0.0329	0.0189	0.0172	0.0223

Table 4.2: Applied binary interaction parameters in the PC-SAFT calculations[71]

4.1. FORCE FIELD VALIDATION

Due to the nature of computer simulations, the first thing that must be checked is the reliability of the simulated results. In order to assess the reliability of the results of the $TraPPE$ force field for binary mixtures of light/heavy hydrocarbon systems, the simulated data must be compared to available experimental data. The literature study (table 1.1, table 1.2, table 1.3, table 1.4) in chapter 1 introduced available experimental data.

Simulations were performed at the state points (table 4.3) of the experimental data in the Gibbs ensemble with Configurational Bias Monte Carlo technique. The simulated methane's mole fraction in the liquid and vapor phase and the liquid and vapor densities for the binary mixtures by $TraPPE$ force field are in almost total agreement with the experimental data (table 4.3). The results can be seen in fig. 4.1 to fig. 4.8.

Mixtures	C_1-C_{12}	C_1-C_{14}	C_1-C_{16}		C_1-C_{20}	C_1-C_{24}	$C_1-Toluene$		
Temperatures [K]	374.05	373	462.45	623.15	423.2	374	277.65	293.15	313.15
Pressures [MPa]	10	2.1	2.08	2.13	1.68	2.15	6.02	3.26	2.68
	15	3.56	3.52	3.23	3.87	7.9	8.1	3.93	4.11
	20	5.06	5.08	5.12	5.1	17.2	13.19	4.77	
	25	6.56	10.28	10.03	6.72	37.2		7.56	
	30	8.03	14.95		7.67	55.36		10.41	
	35	9.5	20.08		8.66	62.88			
	40		25.57		10.6				

Table 4.3: Simulation state points for force field validation

The deviations (eq. (4.3)) of the simulated results (val_{sim}) compared to experimental data (val_{exp}) are also calculated in case of methane-dodecane binary system. The deviations (x_{dev}) can be seen in table 4.4 and in table 4.5.

$$x_{dev} = \frac{val_{exp} - val_{sim}}{val_{exp}} \cdot 100 \tag{4.3}$$

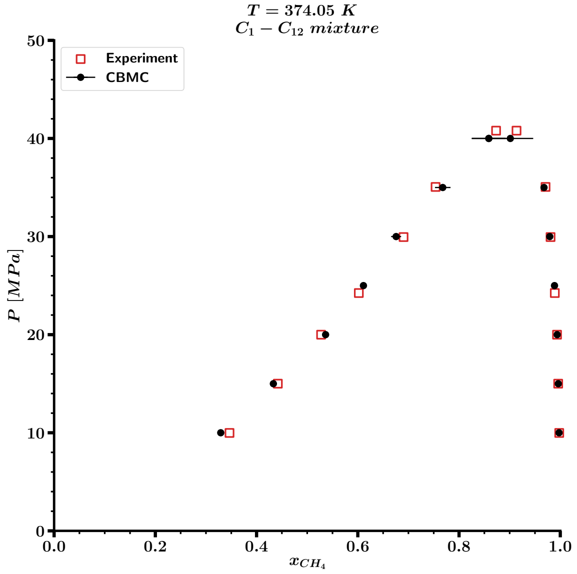

Figure 4.1: Vapor-liquid coexistance curve for Methane - Dodecane system. Experimental coexistence data[34] are shown as red squares. Simulated methane mole fractions for TraPPE force field with CBMC are shown as black dots.

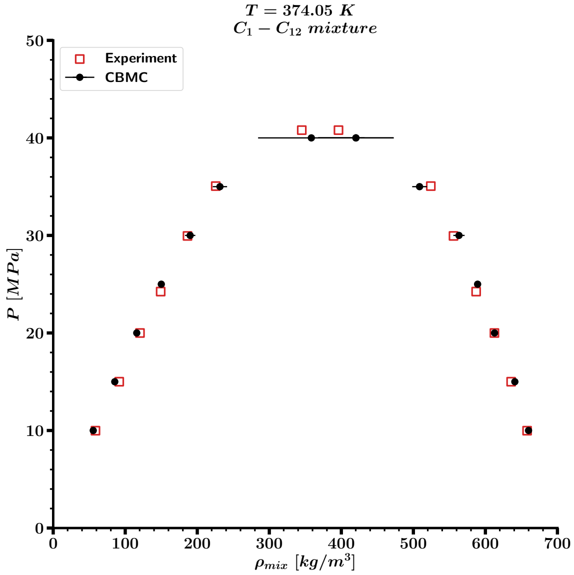

Figure 4.2: Vapor-liquid coexistance curve for Methane - Dodecane system. Experimental coexistence data[34] are shown as red squares. Simulated methane mole fractions for TraPPE force field with CBMC are shown as black dots.

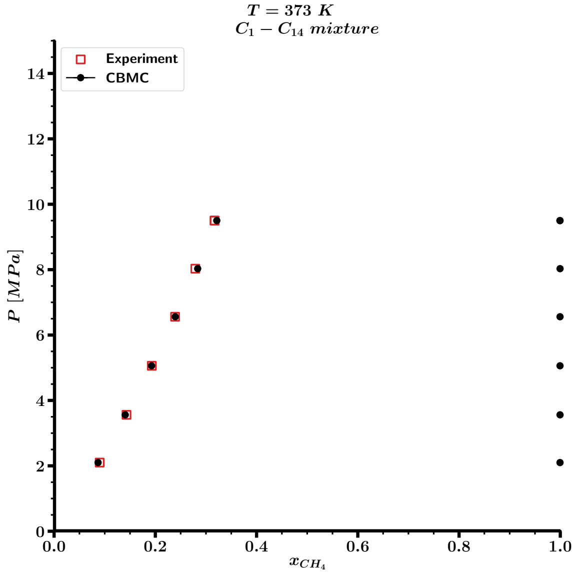

Figure 4.3: Vapor-liquid coexistance curve for Methane - Tetradecane system. Experimental coexistence data[37] are shown as red squares. Simulated methane mole fractions for TraPPE force field with CBMC are shown as black dots.

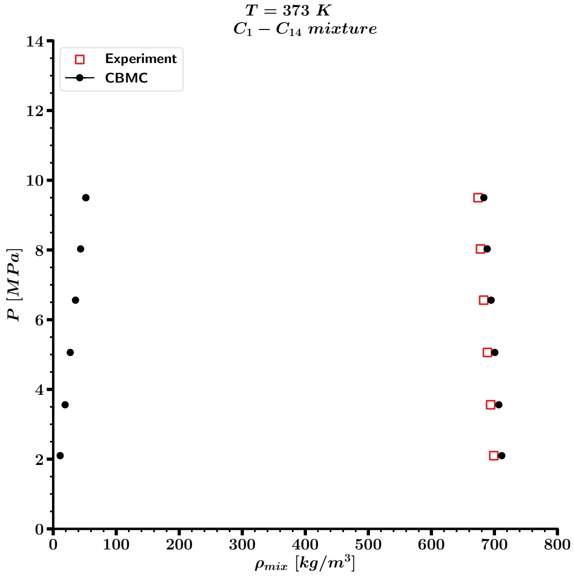

Figure 4.4: Vapor-liquid coexistance curve for Methane - Tetradecane system. Experimental coexistence data[37] are shown as red squares. Simulated methane mole fractions for TraPPE force field with CBMC are shown as black dots.

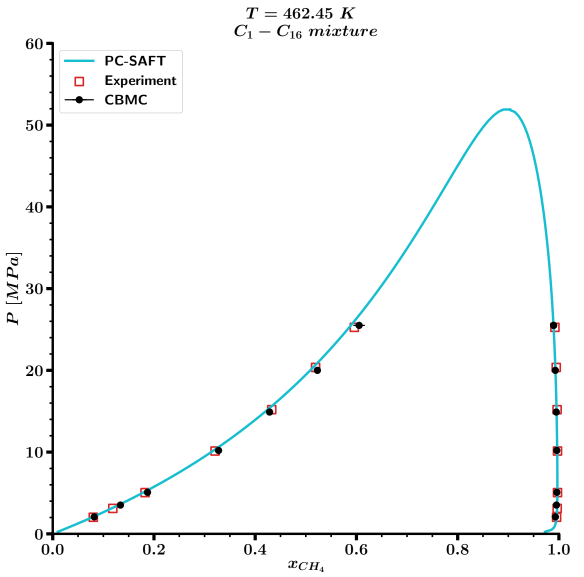

Figure 4.5: Vapor-liquid coexistance curve for Methane - Hexadecane system. Experimental coexistence data[28] are shown as red squares. Coexistence data predicted by PC-SAFT is shown as long cian line. Simulated methane mole fractions for TraPPE force field with CBMC are shown as black dots.

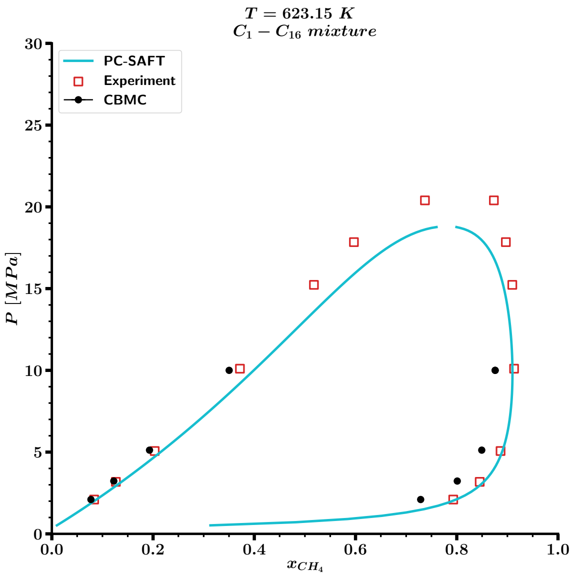

Figure 4.6: Vapor-liquid coexistance curve for Methane - Hexadecane system. Experimental coexistence data[28] are shown as red squares. Coexistence data predicted by PC-SAFT is shown as long cian line. Simulated methane mole fractions for TraPPE force field with CBMC are shown as black dots.

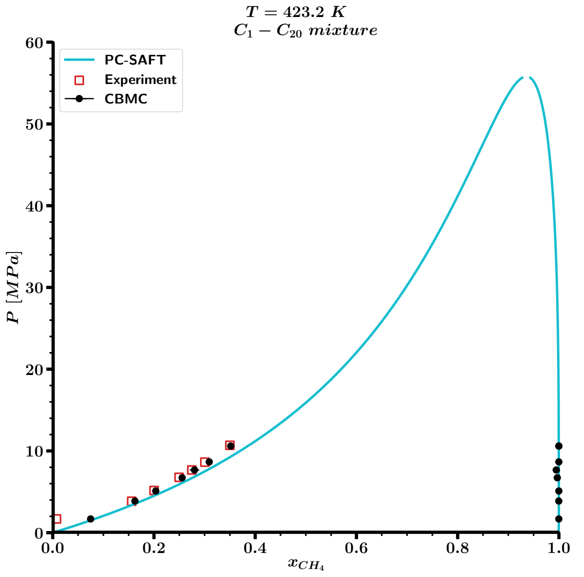

Figure 4.7: Vapor-liquid coexistance curve for Methane - Icosane system. Experimental coexistence data[41] are shown as red squares. Coexistence data predicted by PC-SAFT is shown as long cian line. Simulated methane mole fractions for TraPPE force field with CBMC are shown as black dots.

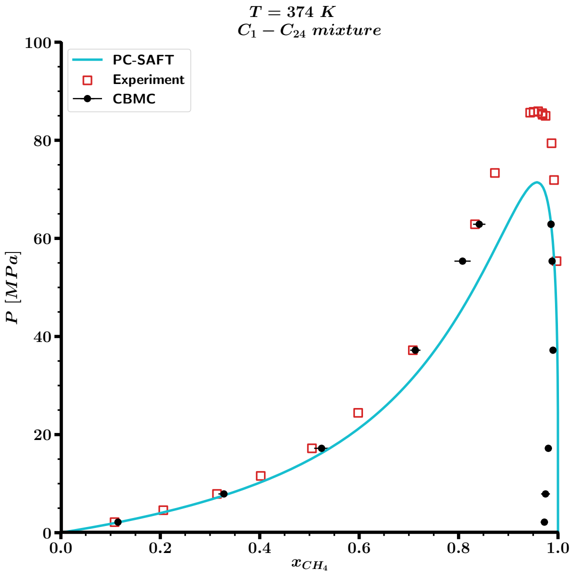

Figure 4.8: Vapor-liquid coexistance curve for Methane - Tetracosane system. Experimental coexistence data[42] are shown as red squares. Coexistence data predicted by PC-SAFT is shown as long cian line. Simulated methane mole fractions for TraPPE force field with CBMC are shown as black dots.

The highest deviation between the simulated and experimental densities among the different state points in case of methane-dodecane binary system is approximately ±3 %. The deviation between the simulated and experimental methane mole fractions for the same binary system ranges from −1.6 % to +5 %. These low deviation values mean that the $TraPPE$ force field with united atom description, introduced in chapter 3, is capable of accurately describing the methane-dodecane binary system.

mixture	$C_1 - C_{12}$					
Temperature[K]	374.05					
Pressures [MPa]	Experiment	Simulation	Deviation	Experiment	Simulation	Deviation
	ρ_{liquid} $[kg/m^3]$		[%]	ρ_{vapor} $[kg/m^3]$		[%]
10	657.891	659.882	-0.303	58.671	55.584	5.262
15	635.738	640.886	-0.810	91.652	85.474	6.740
20	612.535	612.716	-0.029	120.472	115.978	3.731
25	587.146	589.204	-0.351	149.196	150.066	-0.584
30	555.727	563.321	-1.366	186.425	190.113	-1.979
35	524.222	508.607	2.979	225.667	231.457	-2.566
40	396.059	358.370	9.516	345.086	420.239	-21.778

Table 4.4: Simulated and experimental liquid and vapor densities for the methane-dodecane binary system (fig. 4.2)

mixture	$C_1 - C_{12}$					
Temperature[K]	374.05					
Pressures [MPa]	Experiment	Simulation	Deviation	Experiment	Simulation	Deviation
	x_{CH_4}		[%]	y_{CH_4}		[%]
10	0.347	0.329	4.995	0.998	0.998	0.033
15	0.442	0.433	1.990	0.996	0.996	-0.018
20	0.527	0.536	-1.683	0.994	0.994	-0.028
25	0.602	0.611	-1.515	0.989	0.989	0.060
30	0.690	0.676	2.126	0.981	0.979	0.165
35	0.754	0.768	-1.878	0.971	0.968	0.307
40	0.873	0.901	-3.223	0.914	0.859	5.995

Table 4.5: Simulated and experimental methane's mole fractions in the liquid and vapor phase for the methane-dodecane binary system (fig. 4.1)

The exact deviation values are calculated only for the methane-dodecane binary system. However, according to the results of the methane-dodecane binary mixture and by the data represented in fig. 4.1 to fig. 4.8, it can be stated that the $TraPPE$ force field with the united atom description is overall capable of describing the simulated light/heavy binary hydrocarbon systems (C_1 $with$ C_{12}, C_{14}, C_{16}, C_{20} and $with$ C_{24}) accurately.

During validation, state points close to the critical point for every binary mixture were neglected. This choice will be discussed in the following subsections.

As indicated in the results presented already, $TraPPE$ force field demonstrates high performance in reproducing the experimental vapor-liquid phase equilibrum data for binary mixtures of methane with various n-alkanes. Based on these results, the performance of the $TraPPE$ force field for mixtures including aromatic hydrocarbons, particularly the mixture of methane with toluene is assessed as well. The $CBMC$ simulation results for the 10-site toluene and the corresponding experimental data are presented in fig. 4.9, fig. 4.11 and in fig. 4.12. At 313 K the simulations show almost total match with the available experimental data[72].

On the other hand, at 277 K and at 293 K, the deviations of the methane's mole fraction in the liquid phase between the simulations and experiments are significant (15 %) and even higher than the average deviation of binaries of methane with various n-alkanes ($-1.6-5\%$). In order to determine the reason behind this behavior the methane's mole fraction changes over the simulations cycles at different state points were analyzed.

In fig. 4.10 it can be seen that at 277 K the system has not reached equilibrium during initialization cycles and have not even reached equilibrium during production cycles in one of the four simulations. This means that the ensemble average calculation was corrupted by these non-equilibrated results. In order to obtain proper averages, the non-equilibrated simulations at this temperature must be restarted from the system configuration where the simulations were finished.

Furthermore, if one thoroughly checks fig. 4.11, an obvious mistaken simulation point at 4.773 MPa can be seen in the liquid phase. Monte Carlo is a statistical method using random numbers, which means that it is highly unlikely to obtain four different simulations at a state point in which the methane's mole fraction is identical with others. However, for this specific state point this is what fig. 4.13 shows, indicating that the simulations were not ran properly, thus the results of this state point must be neglected.

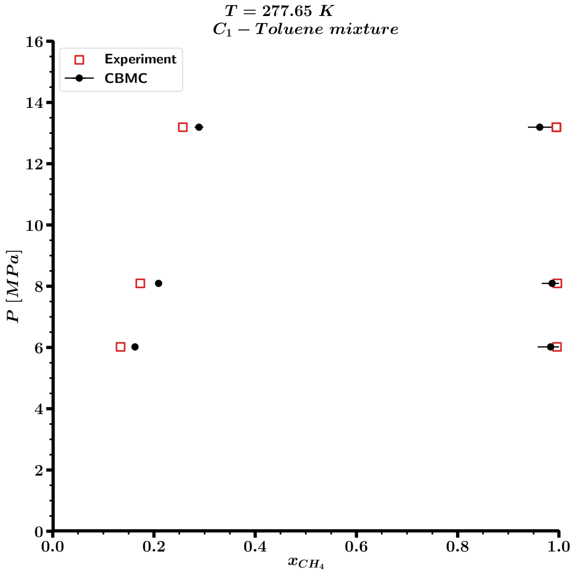

Figure 4.9: Vapor-liquid coexistance curve for Methane - Toluene system. Experimental coexistence data[72] are shown as red squares. Simulated methane mole fractions for TraPPE force field with CBMC are shown as black dots.

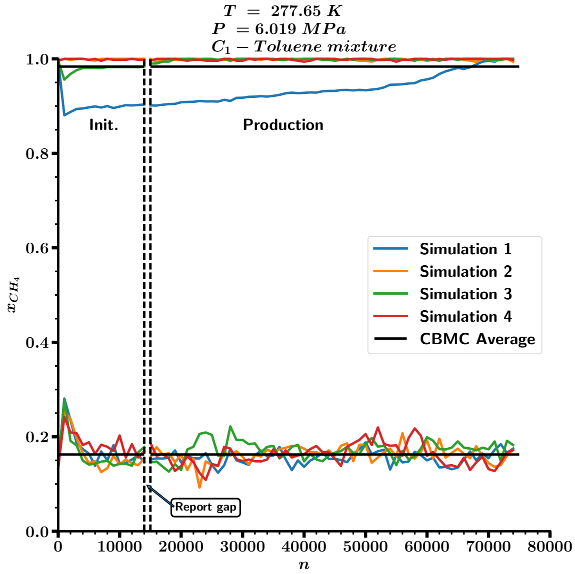

Figure 4.10: Methane's mole fraction change as a function of Monte Carlo cycles

Despite the fact that most of the simulations have not reached equilibrium during initialization cycles, the represented $CBMC$ results show good agreement with the experimental values for the methane-toluene mixture. However, further runs are needed in order to increase the accuracy of the results.

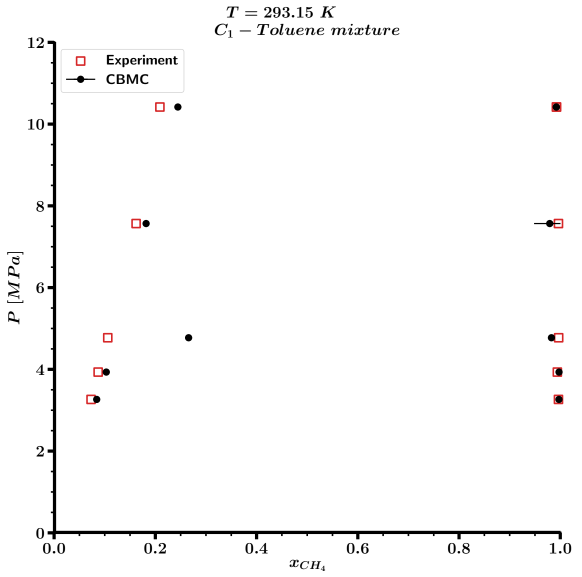

Figure 4.11: Vapor-liquid coexistance curve for Methane - Toluene system. Experimental coexistence data[72] are shown as red squares. Simulated methane mole fractions for TraPPE force field with CBMC are shown as black dots.

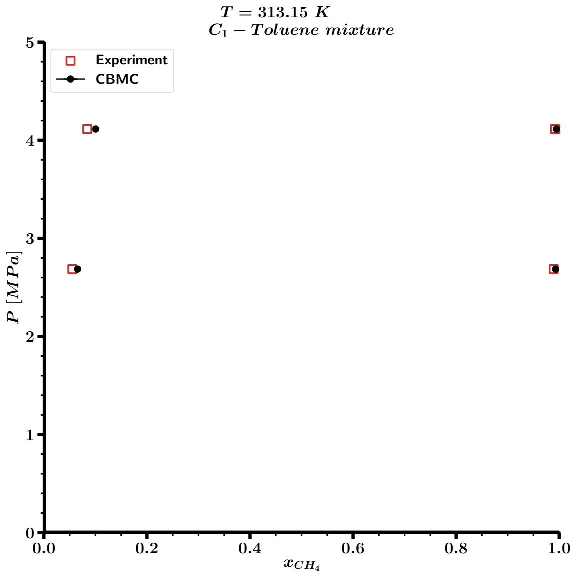

Figure 4.12: Vapor-liquid coexistance curve for Methane - Toluene system. Experimental coexistence data[72] are shown as red squares. Simulated methane mole fractions for TraPPE force field with CBMC are shown as black dots.

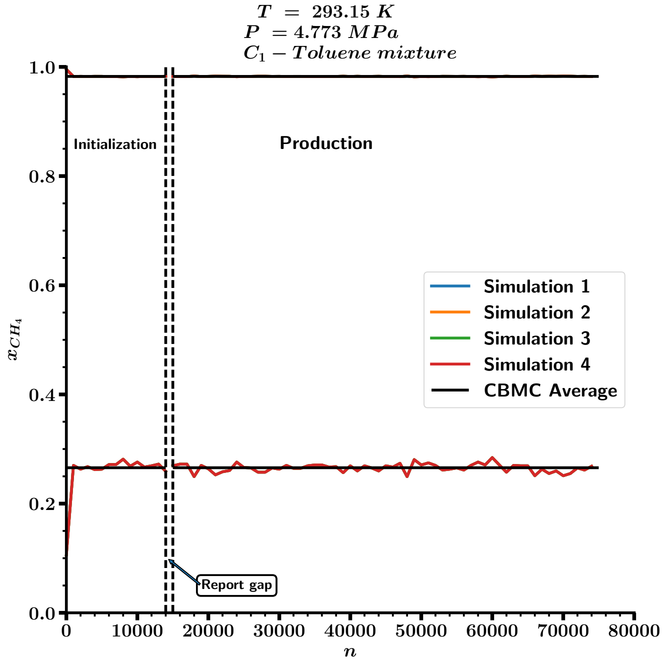

Figure 4.13: Methane's mole fraction change as a function of Monte Carlo cycles

Overall, it was shown that the *TraPPE* force field with united atom description is capable of accurately predicting the vapor-liquid phase equilibrium for the binary mixtures of light/heavy hydrocarbons. The results are very promising, since the original parametrization of *TraPPE* was based on pure components and more specifically on alkanes of low carbon number.

4.2. SIMULATIONS AT EXTRAPOLATED CONDITIONS

As shown in the previous section, $TraPPE$ can accurately describe the phase and volumetric behavior of binary mixtures of light/heavy hydrocarbons. This means that vapor-liquid phase and volumetric behaviors at elevated temperatures and pressures for the different binary mixtures of light/heavy hydrocarbons can be simulated. The $CBMC$ simulation results are compared to $PC-SAFT$ predictions which were done by the collaborating research group led by Professor Ioannis Economou.

In my work binary mixtures of methane with various n-alkanes are investigated. A distinctive feature of these systems is that the methane is much more volatile than the other constituent component of the binary system. Therefore most of the methane is expected to be found in the vapor phase and the less volatile component is expected to be found in the liquid phase at low pressures. As the pressure increases more of the light and volatile component is expected to be found in the liquid phase. As shown in fig. 4.14, this behavior is captured by the $TraPPE$ force field.

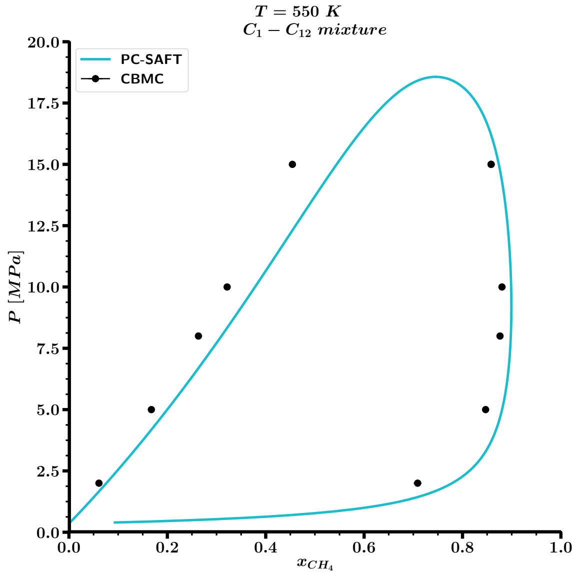

Figure 4.14: Vapor-liquid coexistance curve for Methane - Dodecane system. Coexistence data predicted by PC-SAFT is shown as long cian line. Simulated methane mole fractions for TraPPE force field with CBMC are shown as black dots.

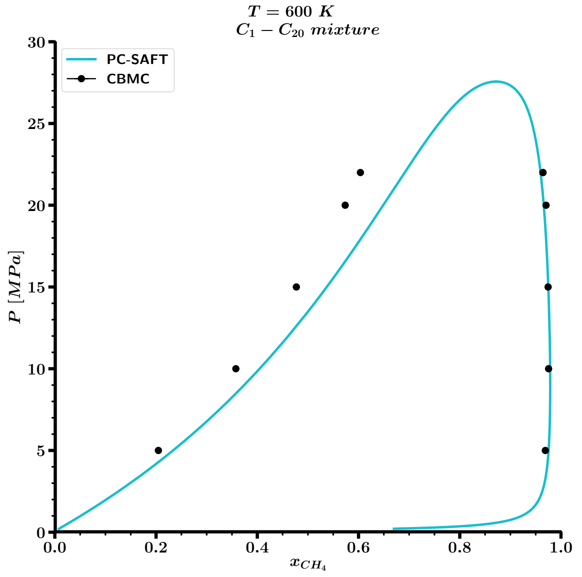

Figure 4.15: Vapor-liquid coexistance curve for Methane - Icosane system. Coexistence data predicted by PC-SAFT is shown as long cian line. Simulated methane mole fractions for TraPPE force field with CBMC are shown as black dots.

Retrograde behavior of a mixture means that liquid forms by isothermal decrease in pressure or by isobaric increase in temperature[14]. $TraPPE$ can capture the retrograde behavior of the simulated binary mixtures of light/heavy hydrocarbons and this can be seen in fig. 4.14.

Based on fig. 4.14, fig. 4.15 and on the figures in Appendix-B, it can be stated that the $CBMC$ simulation results and the data predicted by the $PC-SAFT$ equation of state slightly deviate from each other. This is more pronounced in the liquid phase. Such deviations are expected since the binary interaction parameter fitting for the $PC-SAFT$ equation of state was performed at lower temperatures and pressures [71] than the state points of the extrapolated simulations. However, the $CBMC$ simulation results at the extrapolated state points can serve as reference data for parameter adjustments for the $PC-SAFT$ equation of state. The modification of the $PC-SAFT$ parameters could enhance the vapor-liquid phase equilibrium predictions. Additionally, it would enable vapor-liquid phase equilibrium calculations at those intermediate state points of the extrapolated range that were not simulated by *CBMC*.

4.3. SIMULATIONS NEAR THE CRITICAL POINT

Gibbs ensemble technique uses two simulation boxes. Simulations should remain in a state in which the simulation boxes, representing the vapor and liquid phases, have distinct densities far from each other. In this case the free energy penalty for formation of interfaces in both regions are large[56]. On the other hand, in the vicinity of a critical point the free energy penalty reduces significantly.

In fig. 4.16 a simulation can be seen far away from the critical point. In this plot, the fluctuations of the mole fractions of the methane in the gas phase are negligible, while the fluctuations in the liquid phase are moderate. Additionally, identity changes of the simulation boxes cannot be observed.

First way to identify the approach of the critical point is the appearance of high amplitude fluctuations in the properties of the two regions and the frequent identity changes of the two simulation boxes[56]. This can be seen in fig. 4.17. The second way to identify the approach of the critical point is to create a histogram of the frequency of occurrence of the densities in both regions.[56]. Far from the critical point, equilibrium densities appear as peaks of the probability distribution function. However, in simulations close to the critical point, these distinct peaks cannot be identified.

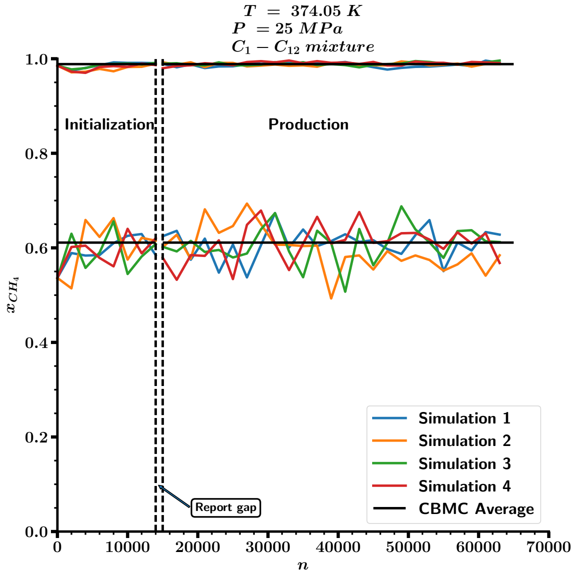

Figure 4.16: Methane's mole fraction change as a function of Monte Carlo cycles

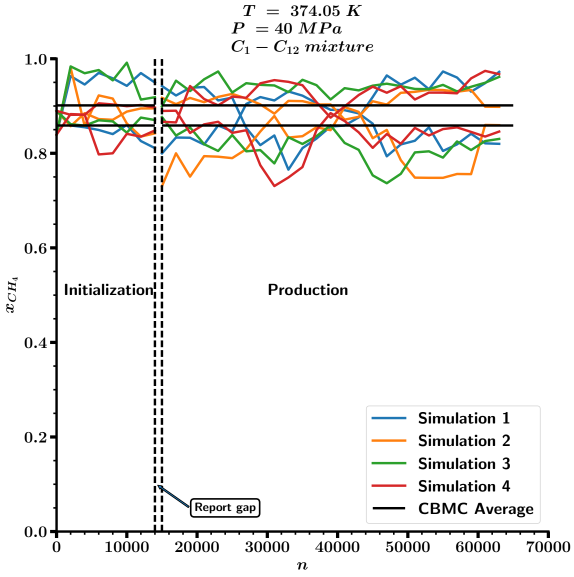

Figure 4.17: Methane's mole fraction change as a function of Monte Carlo cycles

In fig. 4.18 a density distribution function can be seen for a simulation far away from the critical point. In this plot two distinct and separated peaks can be observed which correspond to the equilibrium densities of the liquid and vapor phase. Furthermore, all of the occurred density values are within a relatively narrow range in both phases.

On the other hand, in fig. 4.19 a completely different characteristic can be observed. In this plot, distinct peaks of densities cannot be recognized, the distribution of the occurred values of the den-

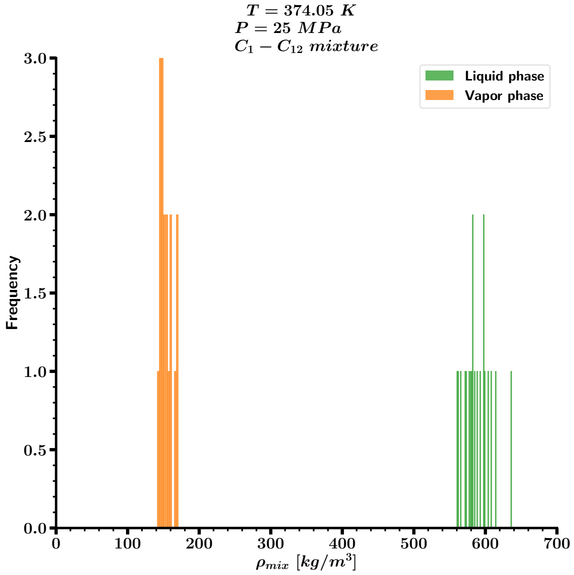

Figure 4.18: Density probability function for the simulation of Methane-Dodecane system at 374.05 K and at 25 MPa

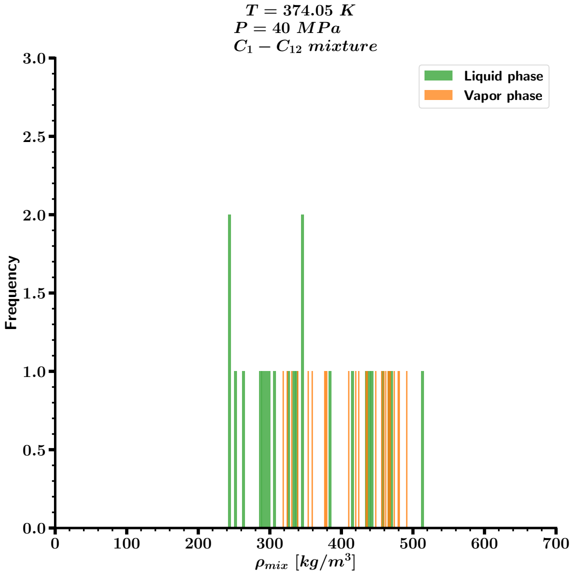

Figure 4.19: Density probability function for the simulation of Methane-Dodecane system at 374.05 K and at 40 MPa

sities in both regions are almost even and they cover a much wider range compared to fig. 4.18. These signs are distinctive features of a simulation which approaches a critical point.

The third way to realize the possible approach of the critical point is the fact that in most of the cases due to the vivid change of the volume of the simulation boxes, the size of one of the simulation boxes goes below the value of twice of the applied cut-off radius. This effect leads to failure of the simulations because in the applied periodic boundary condition only those fluctuations are allowed that have a wavelength compatible with the periodic lattice[19].

Overall, it has been shown that the approach of the critical point can be identified in the Gibbs ensemble, but the calculated properties of the regions cannot be trusted due to the high fluctuations over the simulation cycles.

4.4. EFFECT OF TEMPERATURE

The effects of the temperature on the simulations are described in this section. For this purpose, the results of the $CBMC$ simulations for the methane-dodecane, methane-tetradecane, methane-hexadecane, methane-icosane and methane-tetracosane systems in the range of $400-650\ K$ and $2-40\ MPa$ and the results of the $PC-SAFT$ predictions are presented in fig. 4.20 to fig. 4.29.

The first thing that can be observed is that the $TraPPE$ force field is capable of describing the retrograde behavior of these mixtures. As the temperature increases, the area of the retrograde region increases, the cricondenbar decreases and the shape of the coexistence region widens toward to the liquid phase.

In these plots (fig. 4.20 to fig. 4.29) the poorly fitted binary interaction parameters k_{ij} of the $PC-SAFT$ equation of state can also be observed. The deviations between the liquid phase results of the $CBMC$ technique and the results of the $PC-SAFT$ calculations increase with temperature. Furthermore, the $PC-SAFT$ equation of state underestimates the density of the liquid phase.

On the other hand, the vapor phase results predicted by $CBMC$ and by $PC-SAFT$ are in almost perfect agreement with each other. Moreover, the deviations between the $CBMC$ and $PC-SAFT$ results also increase as the pressure gets higher.

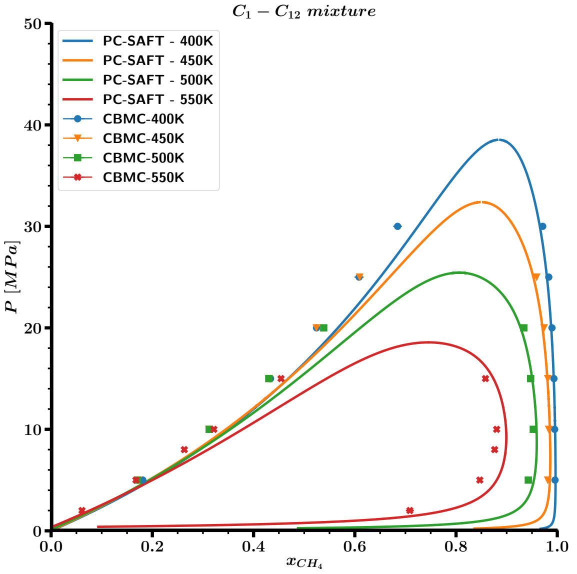

Figure 4.20: Vapor - liquid coexistence curves for Methane - Dodecane binary systems at different temperatures

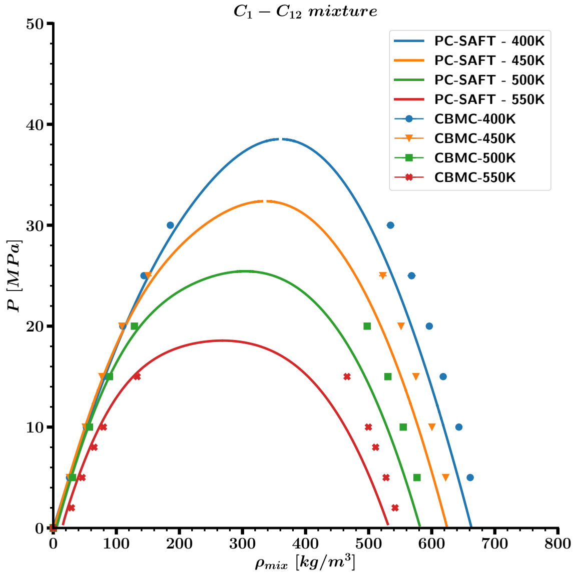

Figure 4.21: Vapor - liquid coexistence curves for Methane - Dodecane binary systems at different temperatures

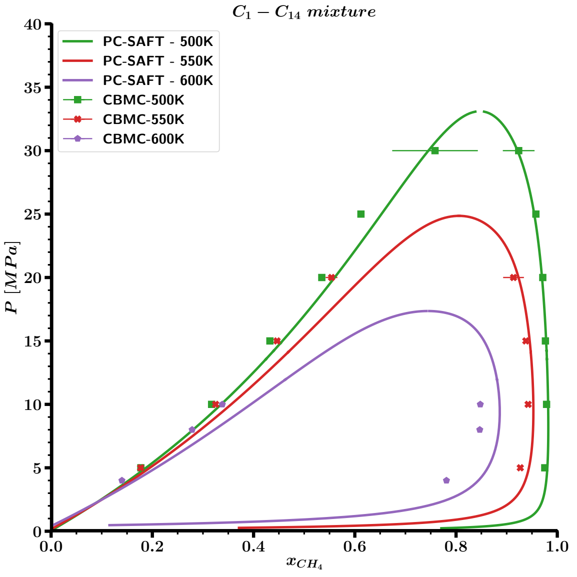

Figure 4.22: Vapor - liquid coexistence curves for Methane - Tetradecane binary systems at different temperatures

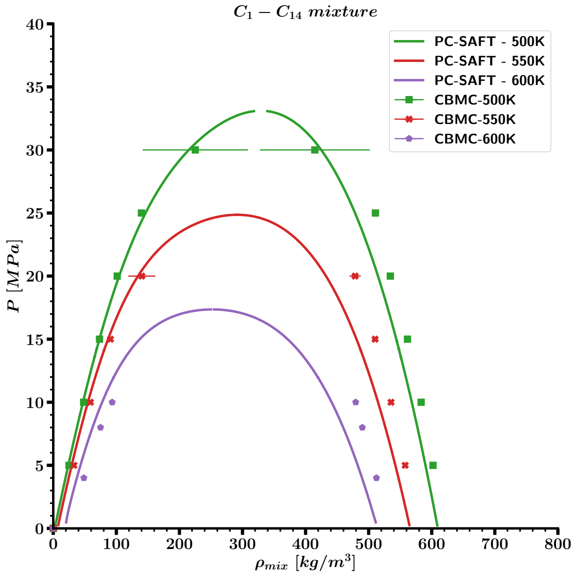

Figure 4.23: Vapor - liquid coexistence curves for Methane - Tetradecane binary systems at different temperatures

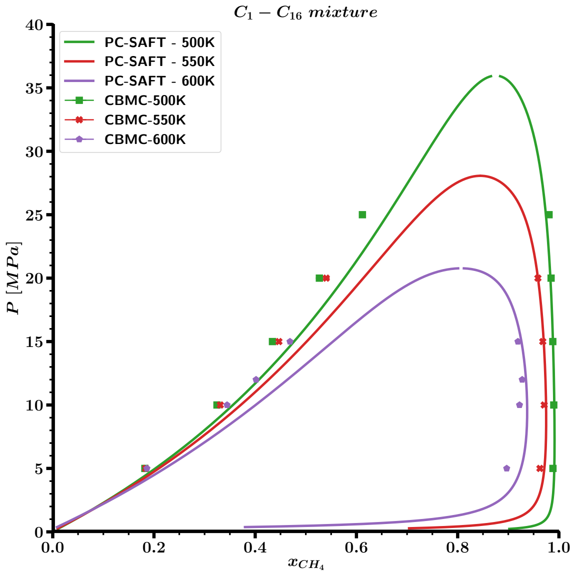

Figure 4.24: Vapor - liquid coexistence curves for Methane - Hexadecane binary systems at different temperatures

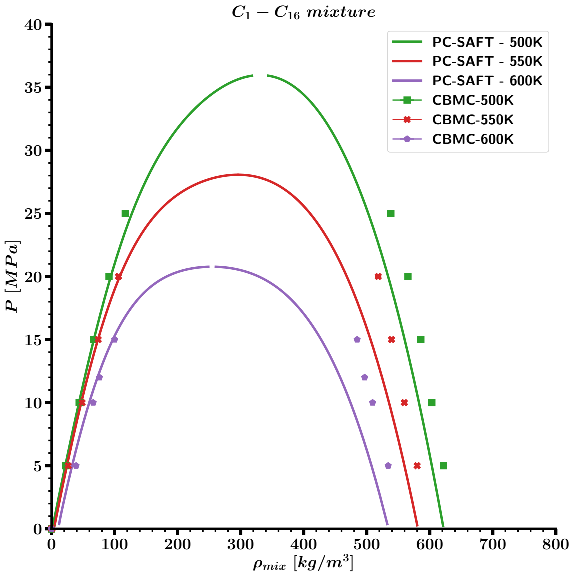

Figure 4.25: Vapor - liquid coexistence curves for Methane - Hexadecane binary systems at different temperatures

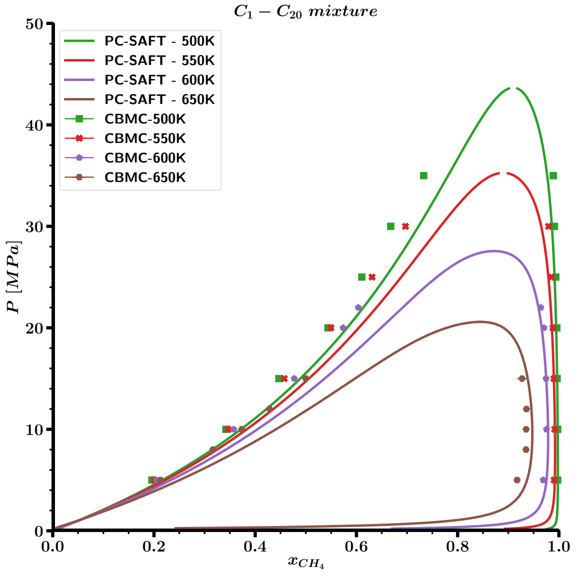

Figure 4.26: Vapor - liquid coexistence curves for Methane - Icosane binary systems at different temperatures

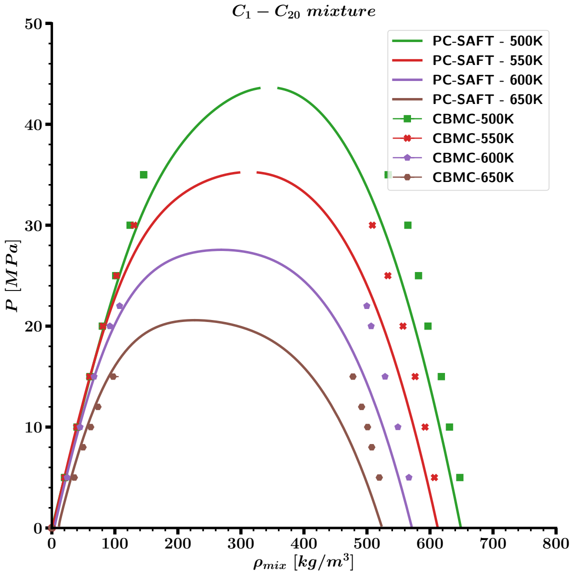

Figure 4.27: Vapor - liquid coexistence curves for Methane - Icosane binary systems at different temperatures

Overall, it can be stated that proper binary interaction parameter adjustment at elevated temperatures and pressures for the $PC-SAFT$ equation of state is required. This can be done by utilizing the created $CBMC$ results.

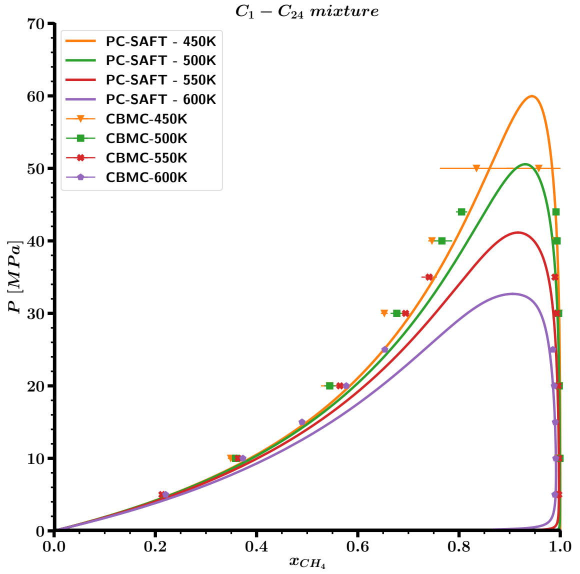

Figure 4.28: Vapor - liquid coexistence curves for Methane - Tetracosane binary systems at different temperatures

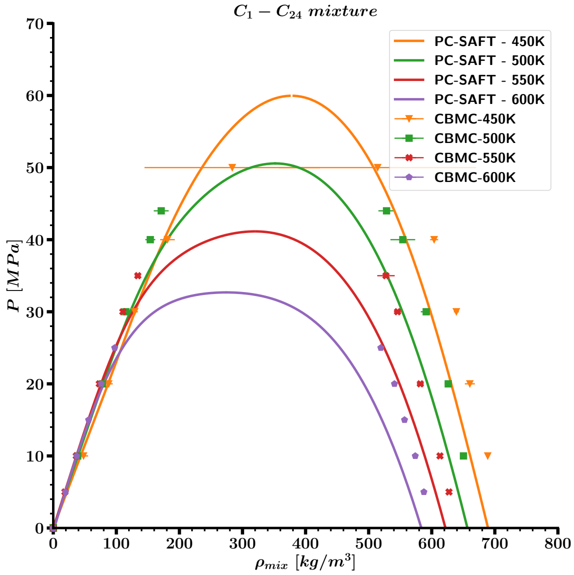

Figure 4.29: Vapor - liquid coexistence curves for Methane - Tetracosane binary systems at different temperatures

4.5. EFFECTS OF CARBON NUMBER

The effects of the heavy component's carbon number on the simulations are described in this section. For this purpose, the results of the $CBMC$ simulations for the methane-dodecane, methane-tetradecane, methane-hexadecane, methane-icosane and methane-tetracosane systems at 550 K and in range of $2-40$ MPa and the results of the $PC-SAFT$ predictions are presented in fig. 4.30 and in fig. 4.31.

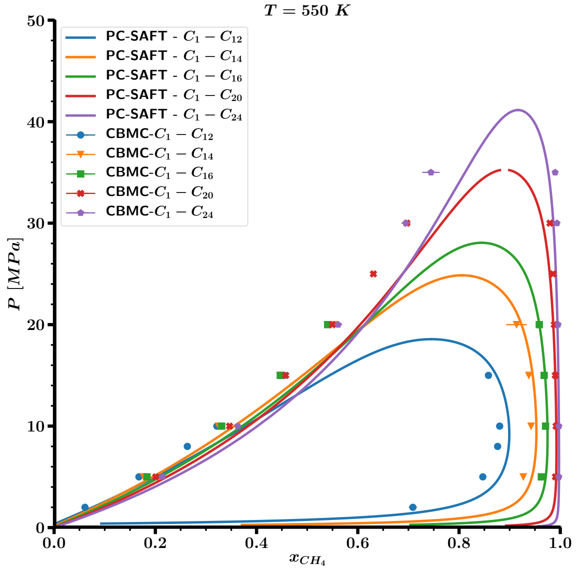

Figure 4.30: Vapor - liquid coexistence curves for different binary systems at $T =$ 550 K

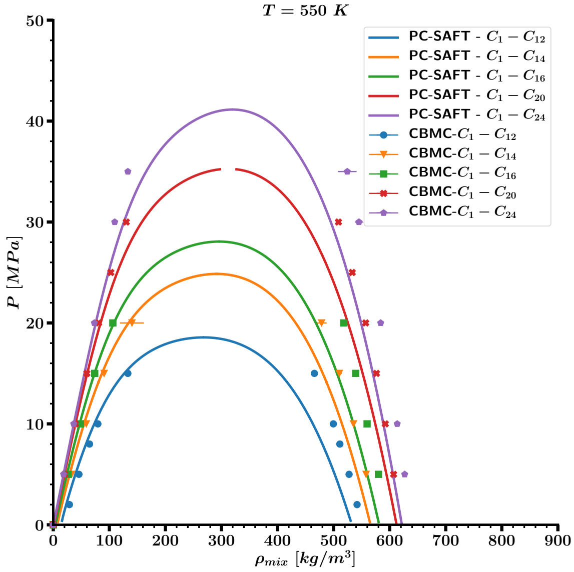

Figure 4.31: Vapor - liquid coexistence curves for different binary systems at $T =$ 550 K

The first thing that can be seen in these plots is the fact that the $TraPPE$ force field accurately predicts the retrograde behavior for these simulated binary mixtures of light/heavy hydrocarbons. As the carbon number of the heavy component decreases, the phase envelopes of the mixtures show increased retrograde behavior.

Furthermore, it can be observed in fig. 4.30 and in fig. 4.31 that the increment of the carbon number of the heavy component does not influence the deviations between the $CBMC$ and $PC-SAFT$ results. The deviations are identical at the same pressure state points for the different mixtures.

Moreover, in these figures (fig. 4.30 and fig. 4.31) the effect of the poorly fitted binary interaction parameters of the $PC-SAFT$ can be also observed. The difference between the $CBMC$ and $PC-SAFT$ results, particularly for the liquid phase are non negligible. For the vapor phase, the results of the $CBMC$ and $PC-SAFT$ are in almost perfect agreement with each other. However, as the pressure increases, the difference between the results become more pronounced for both phases.

4.6. CFCMC SIMULATIONS

Previously, it was shown that the $TraPPE$ force field with united atom description is capable of achieving accurate vapor-liquid phase and volumetric predictions with Configurational Bias Monte Carlo ($CBMC$) technique.

In order to determine the performance of the applied $CBMC$ method, simulations were performed at 462.45 K and 25.5 MPa for the methane-hexadecane and at 600 K and 22 MPa for the methane-icosane binary mixtures with Continuous Fractional Component Monte Carlo($CFCMC$) simulation technique. The results can be seen in fig. 4.32 and in fig. 4.33.

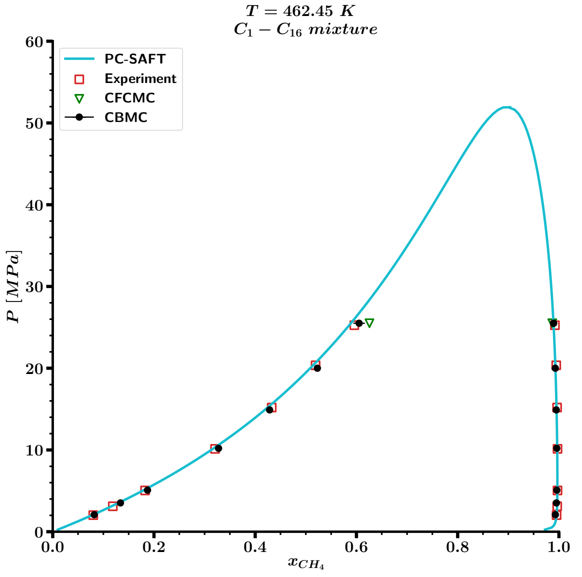

Figure 4.32: Vapor-liquid coexistance curve for Methane - Hexadecane system. Experimental coexistence data[28] are shown as red squares. Coexistence data predicted by PC-SAFT is shown as long cian line. Simulated methane mole fractions for TraPPE force field with CBMC are shown as black dots. Simulated methane mole fractions for TraPPE force field with CFCMC are shown as green triangles.

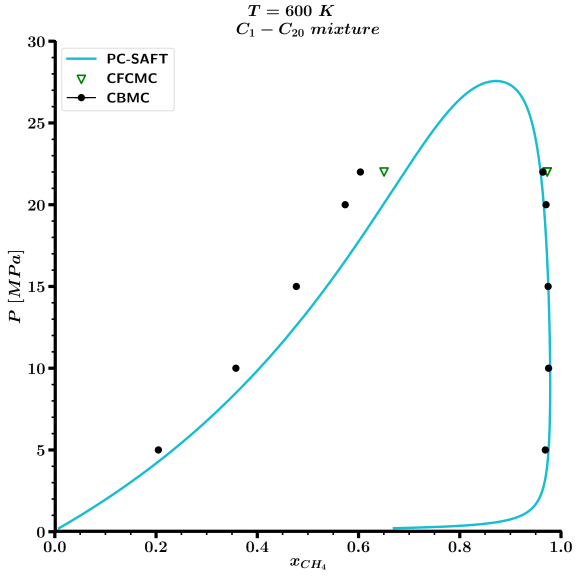

Figure 4.33: Vapor-liquid coexistance curve for Methane - Icosane system. Coexistence data predicted by PC-SAFT is shown as long cian line. Simulated methane mole fractions for TraPPE force field with CBMC are shown as black dots. Simulated methane mole fractions for TraPPE force field with CFCMC are shown as green triangles.

The vapor phase results of both techniques are perfectly identical to each other. On the other hand, the predicted properties of the liquid phases diverge from each other. In case of methane-hexadecane binary mixture the difference between the $CBMC$ and $CFCMC$ result is negligible. In case of methane-icosane binary mixture the divergence is significant. The $CFCMC$ technique predicts better solubility of methane in the liquid phase than the $CBMC$ technique. Furthermore, the $CFCMC$ result of the liquid phase is closer to the $PC-SAFT$ prediction.

This observation could imply that the difference between the liquid phase results of the $CBMC$ and $CFCMC$ would increase with the increment of the carbon number. It must also be mentioned that the $CFCMC$ results are not ensemble averages, due to the fact that only one simulation per state point was performed. In order to clarify the effect of the carbon number more simulations are required.

Overall, based on the good results of the methane-hexadecane system, the applied $CBMC$ technique is suitable for vapor-liquid phase and volumetric calculations for these binary mixtures of light/heavy hydrocarbons.

5

CONCLUSIONS

Gibbs ensemble Monte Carlo is one of the most popular methods to calculate vapor-liquid phase equilibrium for binary mixtures. However, the acceptance probabilities for the different system moves are low for systems which contain long chain molecules. For this reason, in this work Configurational Bias Monte Carlo technique using $TraPPE$ force field was employed in order to calculate the vapor-liquid phase equilibrium and volumetric behavior of binary mixtures of light/heavy hydrocarbons.

At first, the simulation results were validated against the available experimental data for the binary mixtures of methane with dodecane, tetradecane, hexadecane, icosane, tetracosane and toluene. Based on our results, $TraPPE$ model with united atom description was able to predict the vapor-liquid phase equilibrium data for these mixtures very accurately, although initial parametrization of this force field was based on pure alkanes.

Given the high performance of the combination of the $CBMC$ method and $TraPPE$ force field, simulations were performed at extrapolated conditions, temperatures up to 650 K and pressures up to 50 MPa, for which experimental data are not available in the open literature. The calculated results of the molecular simulations were compared to $PC-SAFT$ predictions.

The simulation results at extrapolated conditions showed that there is a slight deviation between the $CBMC$ and $PC-SAFT$ results, which is more pronounced for the liquid phase. Such differences are expected because the initial parameter fitting of the $PC-SAFT$ was performed at lower temperatures and pressures. As a consequence, new parametrization of the $PC-SAFT$ equation of state is necessary for these state points, which can be done by utilizing the results of the $CBMC$ simulations.

Afterwards, it was shown that an inherent problem of the Gibbs ensemble simulations is the poor sampling close to the critical points, due to high fluctuations of the simulations boxes. Therefore, the state points in the vicinity of the critical point need further investigation. Furthermore, different techniques were introduced, such as histogram of frequency of occurrence of densities, in order to recognize the approach of the critical point.

Then, the effect of temperature on the simulations were examined. For the liquid phase properties, it was shown that as the temperature increases, the deviation between $CBMC$ and $PC-SAFT$ results tend to increase. Similarly, the results indicated that as the pressure increases, the discrepancy between the molecular simulations and the equation of state modeling becomes more pronounced.

On the other hand, there is no difference in the predicted vapor phase properties by both methods as the temperature increases.

The effect of the length of the long hydrocarbon component in the binary mixtures was assessed as well. It was shown that the predictive ability of the $CBMC$ technique with $TraPPE$ force field does not deteriorate even when the asymmetry of the mixtures becomes higher (e.g. $C_1 - C_{20}$, $C_1 - C_{24}$).

Lastly, the performance of the applied $CBMC$ simulation method was assessed. State points were selected for simulations by both $CBMC$ and $CFCMC$. The outcome of these simulations indicated that there is a slight difference between the results of the applied methods. However, the predicted values by both methods were still consistent and close to each other. This means that the $CBMC$ simulation method is suitable for modeling binary mixtures of light/heavy hydrocarbons.

Overall, it was shown that the applied $CBMC$ technique and the $TraPPE$ force field with united atom description in the Gibbs ensemble is suitable to determine accurate vapor-liquid phase equilibria for binary mixtures of light/heavy hydrocarbons. New data were produced in order to fill the gap in the available literature. The analyzes of these new data showed that adjustment of the applied $PC-SAFT$ parameters at these elevated temperature and pressure state points would be necessary in order to achieve better equation of state predictions. Furthermore, this thesis could be the foundation of further research topics, such as assessing the applicability of the $TraPPE$ force field for ternary mixtures of hydrocarbons.

BIBLIOGRAPHY

[1] U. S. Energy Information Administration. International energy outlook 2016, 2016.

[2] International Energy Agency. World energy outlook 2016 - executive summary - english version, 2016.

[3] N. A. Owen, O. R. Inderwildi, and David A. King. The status of conventional world oil reserves — hype or cause for concern? *Energy Policy*, 38(8):4743 – 4749, 2010.

[4] H. Wang, F. Ma, X. Tong, Z. Liu, X. Zhang, Z. Wu, D. Li, B. Wang, Y. Xie, and L. Yang. Assessment of global unconventional oil and gas resources. *Petroleum Exploration and Development*, 43(6):925 – 940, 2016.

[5] S. Sleep, J. M. McKellar, J. A. Bergerson, and H. L. MacLean. Expert assessments of emerging oil sands technologies. *Journal of Cleaner Production*, 144:90 – 99, 2017.

[6] M. Ding, Y. Wang, D. Liu, W. Wang, and W. Chen. Mutual interactions of co2/oil and natural gas/oil systems and their effects on the eor process. *Petroleum Science and Technology*, 33(23-24):1890 – 1900, 2015.

[7] O. Redlich and J. N. S. Kwong. On the thermodynamics of solutions. v. an equation of state. fugacities of gaseous solutions. *Chemical Reviews*, 44(1):233–244, 1949.

[8] D. Peng and D. B. Robinson. A new two-constant equation of state. *Industrial & Engineering Chemistry Fundamentals*, 15(1):59–64, 1976.

[9] G. Soave. Equilibrium constants from a modified redlich-kwong equation of state. *Chemical Engineering Science*, 27(6):1197 – 1203, 1972.

[10] W. G. Chapman, K. E. Gubbins, G. Jackson, and M. Radosz. New reference equation of state for associating liquids. *Industrial & Engineering Chemistry Research*, 29(8):1709–1721, 1990.

[11] W. G. Chapman, K. E. Gubbins, G. Jackson, and M. Radosz. Saft: Equation-of-state solution model for associating fluids. *Fluid Phase Equilibria*, 52:31–38, 1989.

[12] J. Gross and G. Sadowski. Perturbed-chain saft:- an equation of state based on a perturbation theory for chain molecules. *Industrial & Engineering Chemistry Research*, 40(4):1244–1260, 2001.

[13] J. D. Waals and J. S. Rowlinson. *J.D. van der Waals: on the continuity of the gaseous and liquid states*. Studies in statistical mechanics. North-Holland, 1988.

[14] C.H. Whitson, M.R. Brulé, and Society of Petroleum Engineers (U.S.). *Phase Behavior*. Henry L. Doherty series. Henry L. Doherty Memorial Fund of AIME, Society of Petroleum Engineers, 2000.

[15] A. Danesh. *PVT and phase behaviour of petroleum reservoir fluids*, volume 47. Elsevier, 1998.

[16] W. C. Edmister. *Applied hydrocarbon thermodynamics: Volume 2*. Gulf Publishing Company, Houston, TX, 1988.

[17] M. B. Standing. *Volumetric and phase behavior of oil field hydrocarbon systems: Society of Petroleum Engineers.* California Research Corp., 1977.

[18] G. M. Kontogeorgis and G. K. Folas. *Thermodynamic models for industrial applications: from classical and advanced mixing rules to association theories.* John Wiley & Sons, 2009.

[19] D. Frenkel and B. Smit. *Understanding molecular simulation : From algorithms to applications*, volume Volume 1 of *Computational science series.* Academic Press, San Diego,CA, second edition, 2002.

[20] W.L. Jorgensen, J.D. Madura, and C.J. Swenson. Optimized intermolecular potential functions for liquid hydrocarbons. *J. Phys. Chem. Soc.*, 106:6638 – 6646, 1984.

[21] J.I. Siepmann, S. Karaborni, and B. Smit. Simulating the critical behaviour of complex fluids. *Nature*, 365:330 – 332, 1993.

[22] M. G. Martin and J. I. Siepmann. Transferable potentials for phase equilibria. 1. united-atom description of n-alkanes. *J. Phys. Chem. B*, 102(14):2569 – 2577, 1998.

[23] M. G. Martin and J. I. Siepmann. Novel configurational-bias monte carlo method for branched molecules. transferable potentials for phase equilibria. 2. united-atom description of branched alkanes. *The Journal of Physical Chemistry B*, 103(21):4508–4517, 1999.

[24] C. D. Wick, M. G. Martin, and J. I. Siepmann. Transferable potentials for phase equilibria. 4. united-atom description of linear and branched alkenes and alkylbenzenes. *The Journal of Physical Chemistry B*, 104(33):8008–8016, 2000.

[25] R. Salomon-Ferrer, D. A. Case, and R. C. Walker. An overview of the amber biomolecular simulation package. *Wiley Interdisciplinary Reviews: Computational Molecular Science*, 3(2):198–210, 2013.

[26] D. A. Case, T. E. Cheatham, T. Darden, H. Gohlke, R. Luo, K. M. Merz, A. Onufriev, C. Simmerling, B. Wang, and R. J. Woods. The amber biomolecular simulation programs. *Journal of Computational Chemistry*, 26(16):1668–1688, 2005.

[27] M. Mohammed, F. Ciotta, and J. P. M. Trusler. Viscosities and densities of binary mixtures of hexadecane with dissolved methane or carbon dioxide at temperatures from (298 to 473) k and at pressures up to 120 mpa. *Journal of Chemical & Engineering Data*, 62(1):422–439, 2017.

[28] H. Lin, H. M. Sebastian, and K. Chao. Gas-liquid equilibrium in hydrogen + n-hexadecane and methane + n-hexadecane at elevated temperatures and pressures. *Journal of Chemical and Engineering Data*, 25(3):252–254, 1980.

[29] D. Suleiman and C. A. Eckert. Phase equilibria of alkanes in natural gas systems. 1. alkanes in methane. *Journal of Chemical and Engineering Data*, 40(1):2–11, 1995.

[30] S. Le Roy, E. Behar, and P. Ungerer. Vapour-liquid equilibrium data for synthetic hydrocarbon mixtures. application to modelling of migration from source to reservoir rocks. *Fluid phase equilibria*, 135(1):63–82, 1997.

[31] A. Fenghour, J. P. M. Trusler, and W. A. Wakeham. Phase behaviour and density of model reservoir fluids at high temperature and pressure. *Fluid phase equilibria*, 158:783–794, 1999.

[32] M. Rijkers, V. B. Maduro, C. J. Peters, and J. de S. Arons. Measurements on the phase behavior of binary mixtures for modeling the condensation behavior of natural gas: Part ii. the system methane+ dodecane. *Fluid Phase Equilibria*, 72:309–324, 1992.

[33] A. Böttger, Á. P. Kamps, and G. Maurer. An experimental investigation on the solubility of methane in 1-octanol and n-dodecane at ambient temperatures. *Fluid Phase Equilibria*, 427:566–574, 2016.

[34] J. Delhommelle, A. Boutin, B. Tavitian, A. D. Mackie, and A. H. Fuchs. Vapour-liquid coexistence curves of the united-atom and anisotropic united-atom force fields for alkane mixtures. *Molecular Physics*, 96(10):1517–1524, 1999.

[35] A. D. Mackie, B. Tavitian, A. Boutin, and A. H. Fuchs. Vapour-liquid phase equilibria predictions of methane–alkane mixtures by monte carlo simulation. *Molecular Simulation*, 19(1):1–15, 1997.

[36] J. F. Arnaud. *Caractirisat ion des propriitis physiques et thermodynamiques des fluides pétroliers á haute pression.* PhD thesis, Université de Pau, 1995.

[37] H. Nourozieh, M. Kariznovi, and J. Abedi. Vapor - liquid equilibrium measurement and thermodynamic modeling of binary systems (methane+n-tetradecane). *Fluid Phase Equilibria*, 318:96–101, 2012.

[38] T. J. Hughes, M. E. Kandil, B. F. Graham, K. N. Marsh, S. H. Huang, and E. F. May. Phase equilibrium measurements of (methane+ benzene) and (methane+ methylbenzene) at temperatures from (188 to 348) k and pressures to 13mpa. *The Journal of Chemical Thermodynamics*, 85:141–147, 2015.

[39] H. Lin, H. M. Sebastian, J. J. Simnick, and K. Chao. Gas-liquid equilibrium in binary mixtures of methane with n-decane, benzene, and toluene. *Journal of Chemical and Engineering Data*, 24(2):146–149, 1979.

[40] M. Elbishlawi and J. R. Spencer. Equilibrium relations of two methane-aromatic binary systems at 150° f. *Industrial & Engineering Chemistry*, 43(8):1811–1815, 1951.

[41] N. A. Darwish, J. Fathikalajahi, K. A. M. Gasem, and R. L. Robinson Jr. Solubility of methane in heavy normal paraffins at temperatures from 323 to 423 k and pressures to 10.7 mpa. *Journal of Chemical and Engineering Data*, 38(1):44–48, 1993.

[42] E. Flöter, T. W. D. Loos, and J. de S. Arons. High pressure solid-fluid and vapour-liquid equilibria in the system (methane+ tetracosane). *Fluid phase equilibria*, 127(1-2):129–146, 1997.

[43] J. F. Arnaud, P. Ungerer, E. Behar, G. Moracchini, and J. Sanchez. Excess volumes and saturation pressures for the system methane+ n-tetracosane at 374 k. representation by improved eos mixing rules. *Fluid phase equilibria*, 124(1-2):177–207, 1996.

[44] M. Christov and R. Dohrn. High-pressure fluid phase equilibria: experimental methods and systems investigated (1994-1999). *Fluid Phase Equilibria*, 202(1):153–218, 2002.

[45] J. Harris and S. A. Rice. A lattice model of a supported monolayer of amphiphile molecules: Monte carlo simulations. *The Journal of chemical physics*, 88(2):1298–1306, 1988.

[46] D. Frenkel, G. C. A. M. Mooij, and B. Smit. Novel scheme to study structural and thermal properties of continuously deformable molecules. *Journal of Physics: Condensed Matter*, 4(12):3053–3076, 1992.

[47] J. I. Siepmann and D. Frenkel. Configurational bias monte carlo: a new sampling scheme for flexible chains. *Molecular Physics*, 75(1):59–70, 1992.

[48] J. J. de Pablo, M. Laso, and U. W. Suter. Simulation of polyethylene above and below the melting point. *The Journal of chemical physics*, 96(3):2395–2403, 1992.

[49] Styliani Consta, T. J. H. Vlugt, J. W. Hoeth, B. Smit, and D. Frenkel. Recoil growth algorithm for chain molecules with continuous interactions. *Molecular physics*, 97(12):1243–1254, 1999.

[50] D. J. Earl and M. W. Deem. *Monte Carlo Simulations*. Humana Press, Totowa, NJ, 2008.

[51] T. J. H. Vlugt, J. P. J. M. van der Eerden, M. Dijkstra, B. Smit, and D. Frenkel. *Introduction to molecular simulation and statistical thermodynamics*. http://www.phys.uu.nl/ vlugt/imsst, 2009.

[52] D. A. McQuarrie. *Statistical Mechanics*. Harper and Row, 1973.

[53] B. Smit, P. D. Smedt, and D. Frenkel. Computer simulations in the gibbs ensemble. *Molecular physics*, 68(4):931–950, 1989.

[54] A.Z. Panagiotopoulos, N. Quirke, M. Stapleton, and D.J. Tildesley. Phase equilibria by simulation in the gibbs ensemble. *Molecular Physics*, 63(4):527–545, 1988.

[55] A. Z. Panagiotopoulos. Direct determination of phase coexistence properties of fluids by monte carlo simulation in a new ensemble. *Molecular Physics*, 61(4):813–826, 1987.

[56] M. Baus, L. F. Rull, Ryckaert, and J. Ryckaert. Observation, prediction and simulation of phase transitions in complex fluid. *NATO ASI Series C*, 460:463 – 501, 1995.

[57] D. Dubbeldam, S. Calero, D. E. Ellis, and R. Q. Snurr. Raspa: molecular simulation software for adsorption and diffusion in flexible nanoporous materials. *Molecular Simulation*, 42(2):81–101, 2016.

[58] A. Z. Panagiotopoulos, N. Quirke, M. Stapleton, and D. J. Tildesley. Phase equilibria by simulation in the gibbs ensemble: alternative derivation, generalization and application to mixture and membrane equilibria. *Molecular Physics*, 63(4):527–545, 1988.

[59] A. Poursaeidesfahani, A. Rahbari, A. Torres-Knoop, D. Dubbeldam, and T. J. H. Vlugt. Computation of thermodynamic properties in the continuous fractional component monte carlo gibbs ensemble. *Molecular Simulation*, 43(3):189–195, 2017.

[60] A. Poursaeidesfahani, A. Torres-Knoop, David Dubbeldam, and T. J. H. Vlugt. Direct free energy calculation in the continuous fractional component gibbs ensemble. *Journal of chemical theory and computation*, 12(4):1481–1490, 2016.

[61] W. Shi and E.J. Maginn. Continuous fractional component monte carlo: an adaptive biasing method for open system atomistic simulations. *Journal of chemical theory and computation*, 3(4):1451–1463, 2007.

[62] W. Shi and E. J. Maginn. Improvement in molecule exchange efficiency in gibbs ensemble monte carlo: development and implementation of the continuous fractional component move. *Journal of computational chemistry*, 29(15):2520–2530, 2008.

[63] D. E. Williams. Nonbonded potential parameters derived from crystalline hydrocarbons. *The Journal of Chemical Physics*, 47(11):4680–4684, 1967.

[64] J. Ryckaert and A. Bellemans. Molecular dynamics of liquid alkanes. *Faraday Discuss. Chem. Soc.*, 66:95–106, 1978.

[65] D. A. Pearlman, D.A. Case, J. W. Caldwell, W. S. Ross, T. E. Cheatham, S. DeBolt, D. Ferguson, G. Seibel, and P. Kollman. Amber, a package of computer programs for applying molecular mechanics, normal mode analysis, molecular dynamics and free energy calculations to simulate the structural and energetic properties of molecules. *Computer Physics Communications*, 91(1-3):1–41, 1995.

[66] J. W. Ponder and D. A. Case. Force fields for protein simulations. *Advances in protein chemistry*, 66:27–85, 2003.

[67] T. E. Cheatham and D. A. Case. Twenty-five years of nucleic acid simulations. *Biopolymers*, 99(12):969–977, 2013.

[68] M. G. Martin and J. I. Siepmann. Predicting multicomponent phase equilibria and free energies of transfer for alkanes by molecular simulation. *Journal of the American Chemical Society*, 119(38):8921–8924, 1997.

[69] University of Minnesota. The siepmann group, 2017. http://chem-siepmann.oit.umn.edu/siepmann/trappe/index.html.

[70] J. Gross and G. Sadowski. Perturbed-chain saft: An equation of state based on a perturbation theory for chain molecules. *Industrial & engineering chemistry research*, 40(4):1244–1260, 2001.

[71] W. Yan, F. Varzandeh, and E. H. Stenby. Pvt modeling of reservoir fluids using pc-saft eos and soave-bwr eos. *Fluid Phase Equilibria*, 386:96–124, 2015.

[72] T. J. Hughes, M. E. Kandil, B. F. Graham, K. N. Marsh, S. H. Huang, and E. F. May. Phase equilibrium measurements of (methane + benzene) and (methane + methylbenzene) at temperatures from (188 to 348) k and pressures to 13 {MPa}. *The Journal of Chemical Thermodynamics*, 85:141 – 147, 2015.

A

APPENDIX-A

A.1. METHANE - DODECANE BINARY MIXTURE

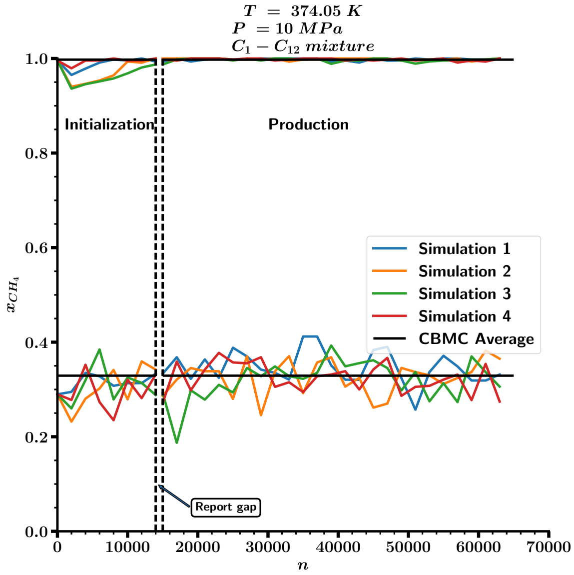

Figure A.1: Methane's mole fraction change as a function of Monte Carlo cycles at $T = 374.05\ K$ and at $P = 10\ MPa$

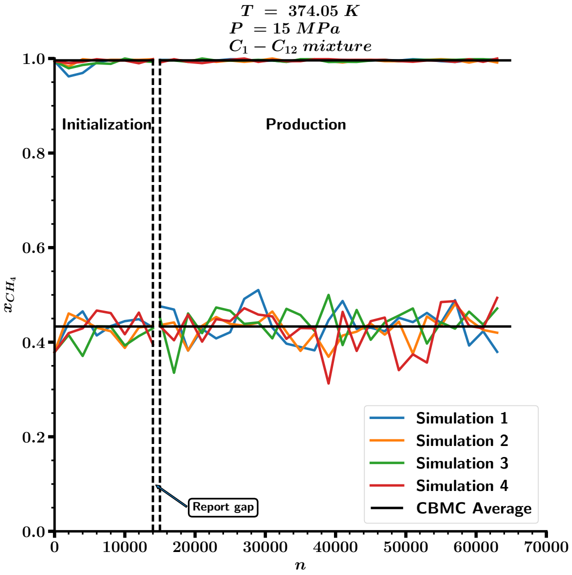

Figure A.2: Methane's mole fraction change as a function of Monte Carlo cycles at $T = 374.05\ K$ and at $P = 15\ MPa$

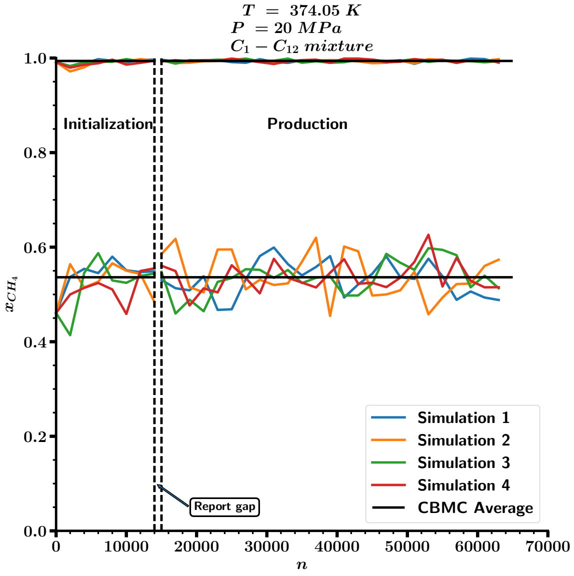

Figure A.3: Methane's mole fraction change as a function of Monte Carlo cycles $T = 374.05\ K$ and at $P = 20\ MPa$

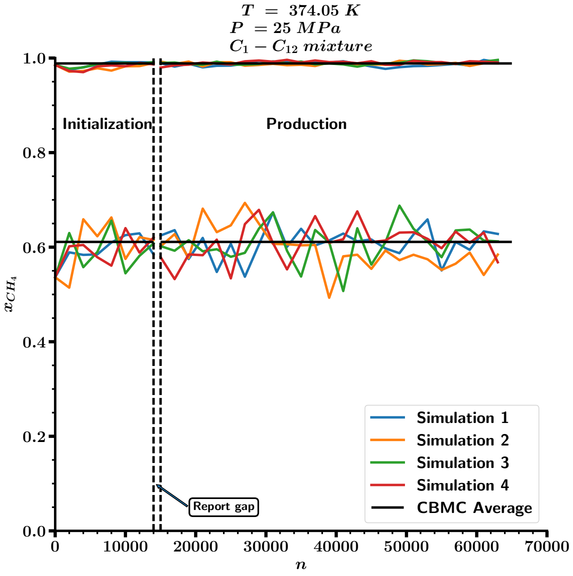

Figure A.4: Methane's mole fraction change as a function of Monte Carlo cycles $T = 374.05\ K$ and at $P = 25\ MPa$

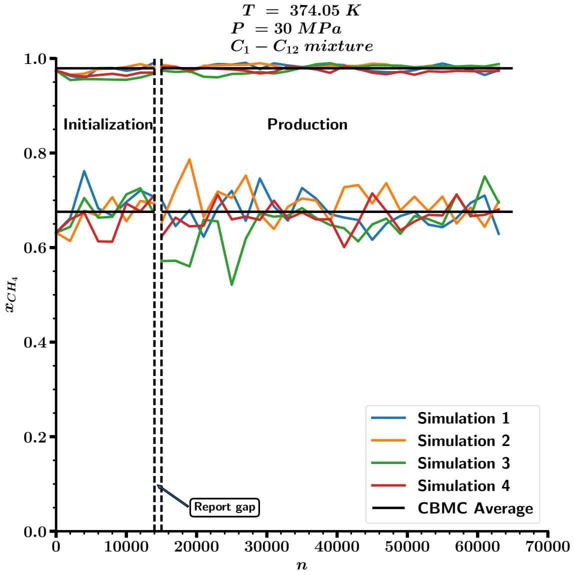

Figure A.5: Methane's mole fraction change as a function of Monte Carlo cycles at $T = 374.05\ K$ and at $P = 30\ MPa$

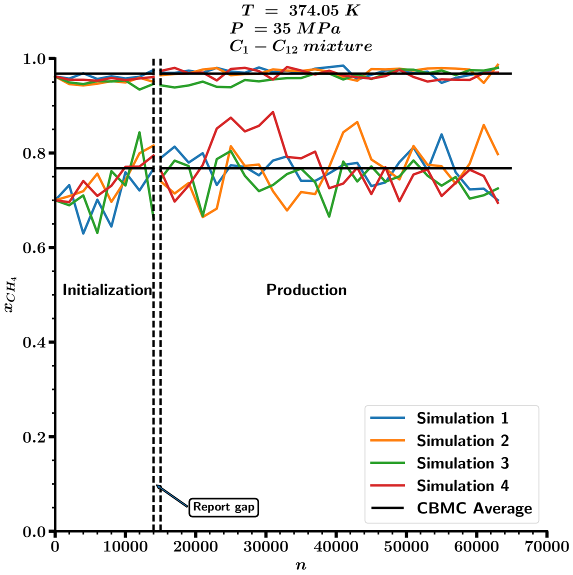

Figure A.6: Methane's mole fraction change as a function of Monte Carlo cycles at $T = 374.05\ K$ and at $P = 35\ MPa$

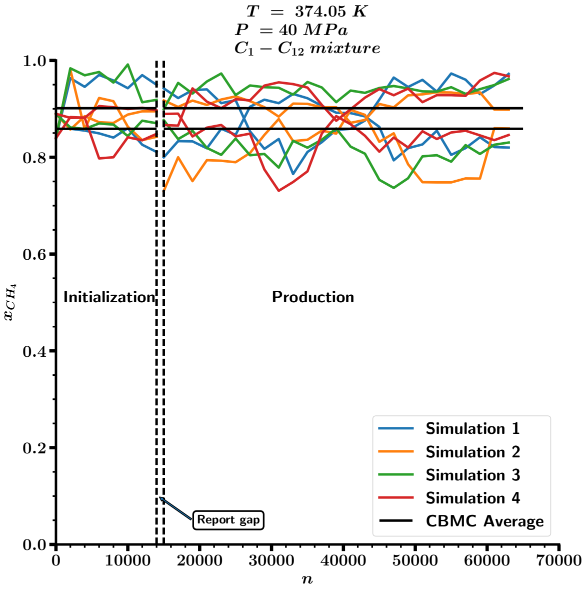

Figure A.7: Methane's mole fraction change as a function of Monte Carlo cycles at $T = 374.05\ K$ and at $P = 40\ MPa$

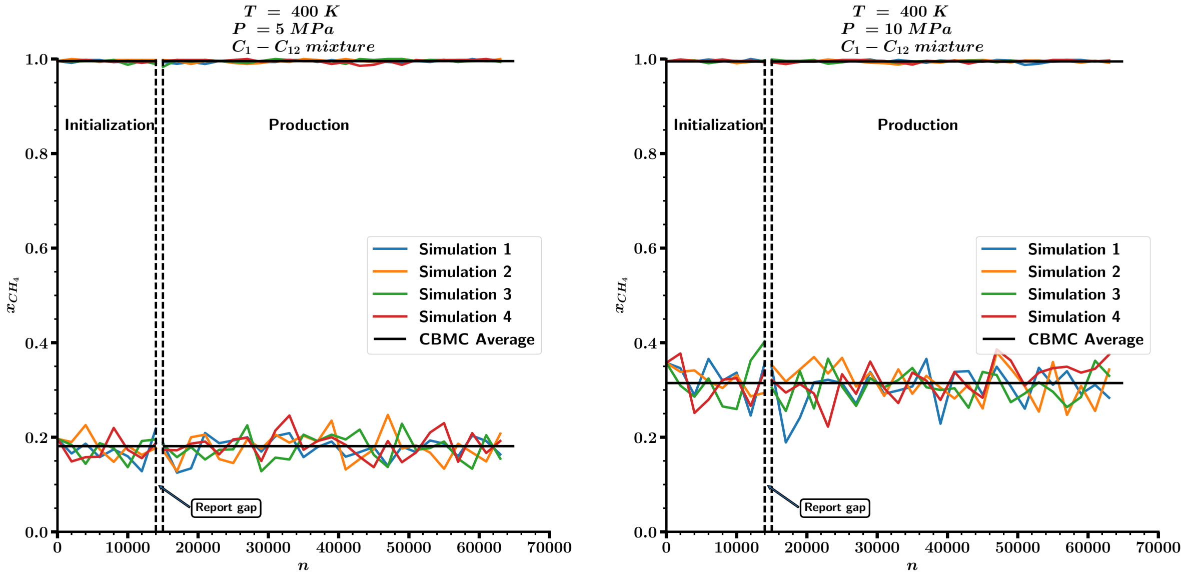

Figure A.8: Methane's mole fraction change as a function of Monte Carlo cycles at $T = 400\ K$ and at $P = 5\ MPa$

Figure A.9: Methane's mole fraction change as a function of Monte Carlo cycles at $T = 400\ K$ and at $P = 10\ MPa$

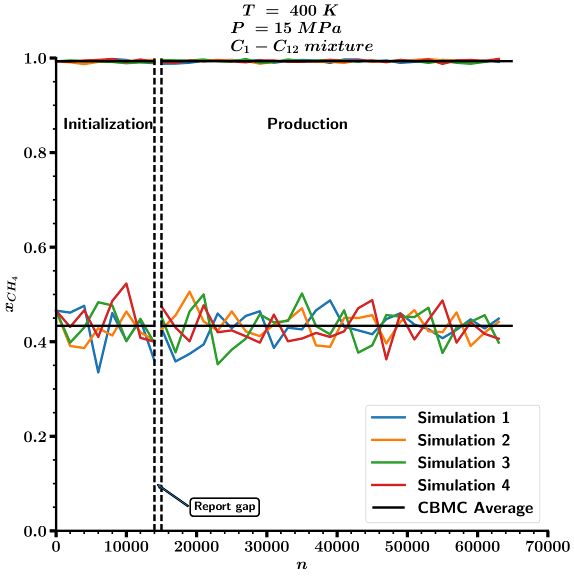

Figure A.10: Methane's mole fraction change as a function of Monte Carlo cycles at $T = 400\ K$ and at $P = 15\ MPa$

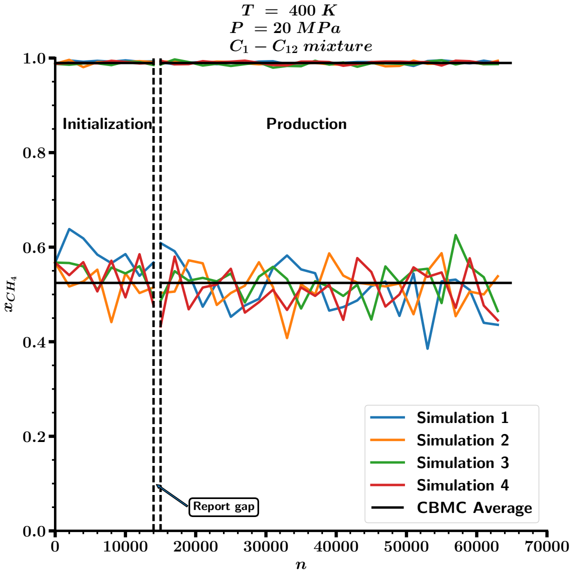

Figure A.11: Methane's mole fraction change as a function of Monte Carlo cycles at $T = 400\ K$ and at $P = 20\ MPa$

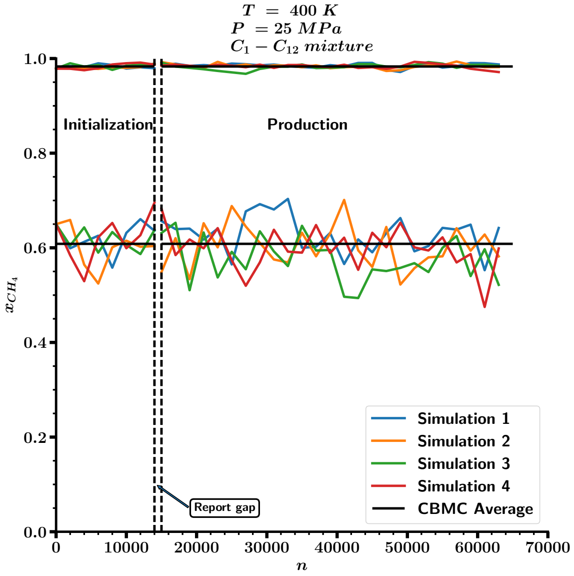

Figure A.12: Methane's mole fraction change as a function of Monte Carlo cycles at $T = 400\ K$ and at $P = 25\ MPa$

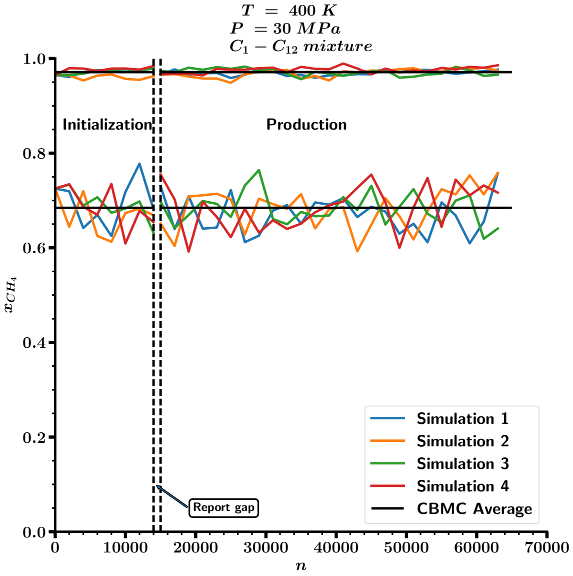

Figure A.13: Methane's mole fraction change as a function of Monte Carlo cycles at $T = 400\ K$ and at $P = 30\ MPa$

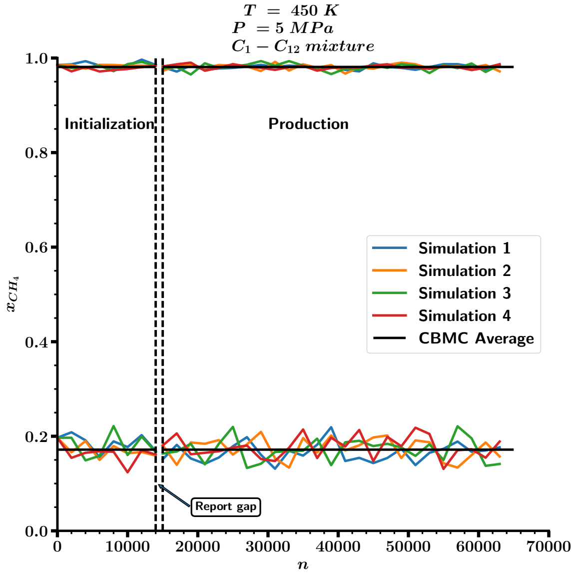

Figure A.14: Methane's mole fraction change as a function of Monte Carlo cycles at $T = 450\ K$ and at $P = 5\ MPa$

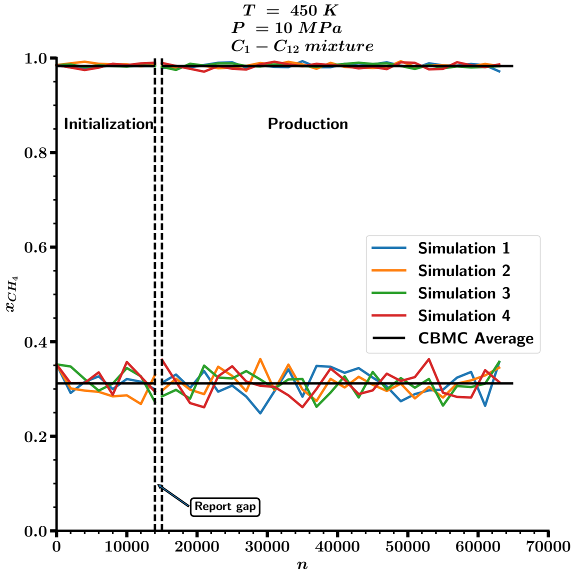

Figure A.15: Methane's mole fraction change as a function of Monte Carlo cycles at $T = 450\ K$ and at $P = 10\ MPa$

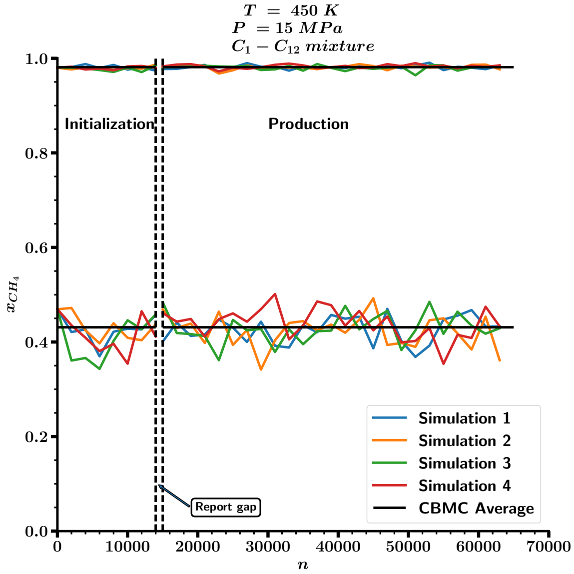

Figure A.16: Methane's mole fraction change as a function of Monte Carlo cycles at $T = 450\ K$ and at $P = 15\ MPa$

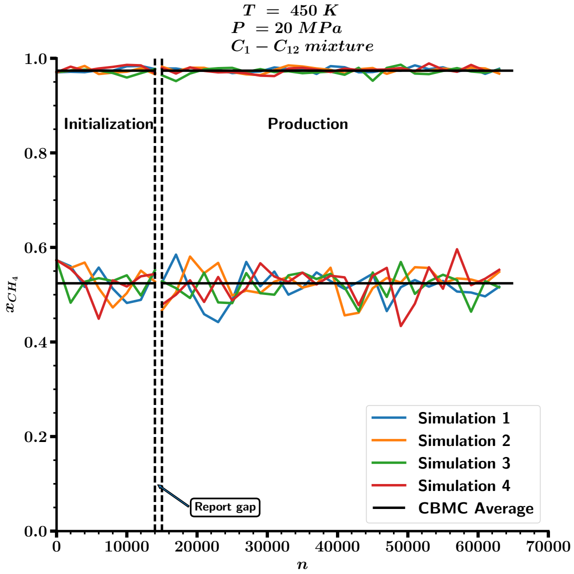

Figure A.17: Methane's mole fraction change as a function of Monte Carlo cycles at $T = 450\ K$ and at $P = 20\ MPa$

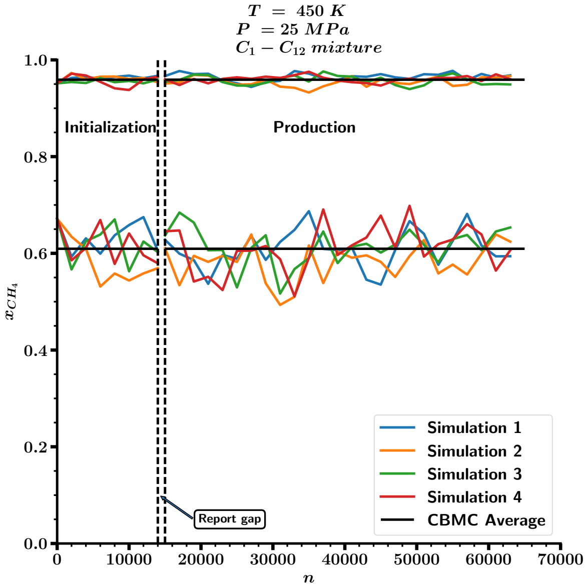

Figure A.18: Methane's mole fraction change as a function of Monte Carlo cycles at $T = 450\ K$ and at $P = 25\ MPa$

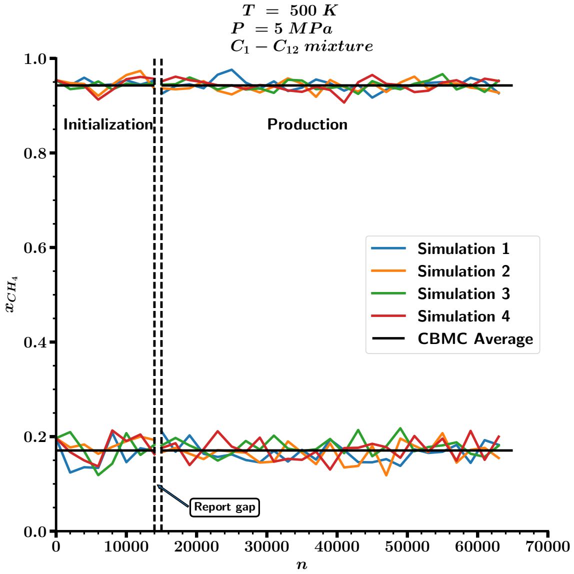

Figure A.19: Methane's mole fraction change as a function of Monte Carlo cycles at $T = 500\ K$ and at $P = 5\ MPa$

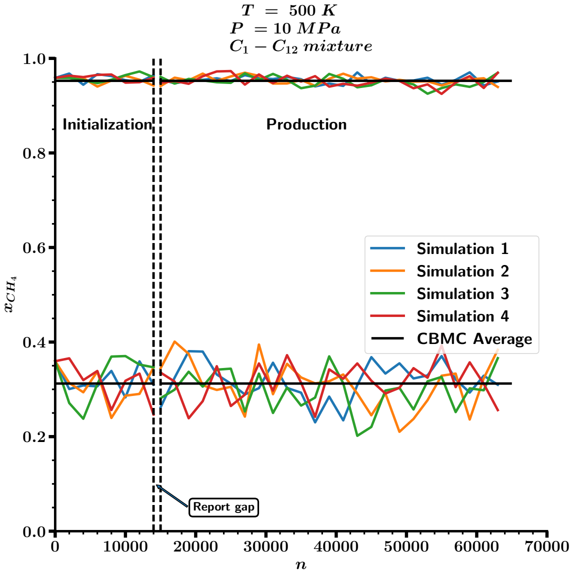

Figure A.20: Methane's mole fraction change as a function of Monte Carlo cycles at $T = 500\ K$ and at $P = 10\ MPa$

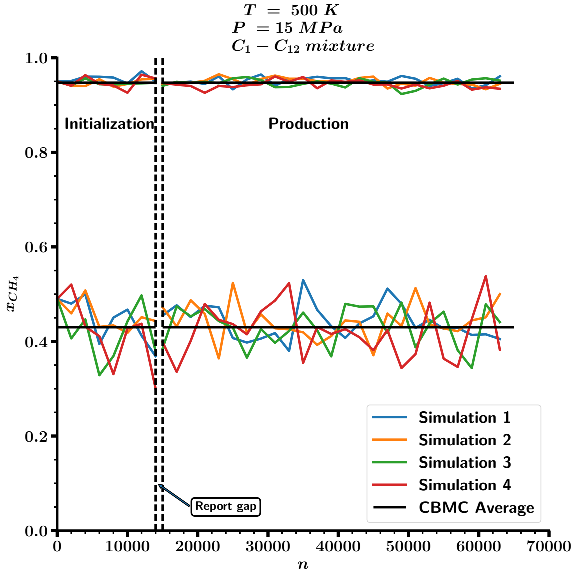

Figure A.21: Methane's mole fraction change as a function of Monte Carlo cycles at $T = 500\ K$ and at $P = 15\ MPa$

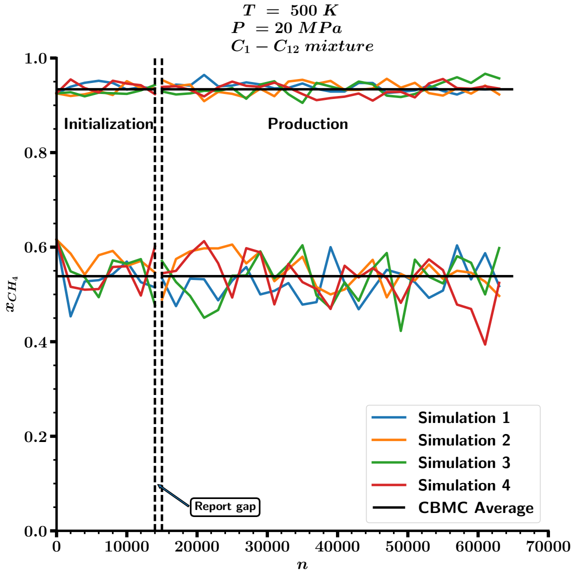

Figure A.22: Methane's mole fraction change as a function of Monte Carlo cycles at $T = 500\ K$ and at $P = 20\ MPa$

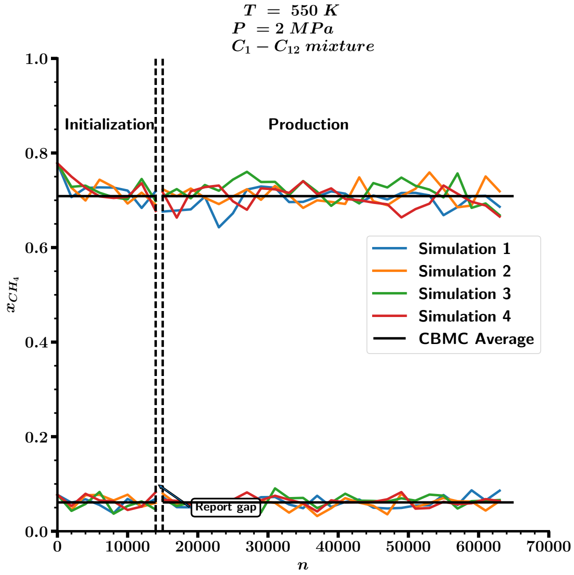

Figure A.23: Methane's mole fraction change as a function of Monte Carlo cycles at $T = 550\ K$ and at $P = 2\ MPa$

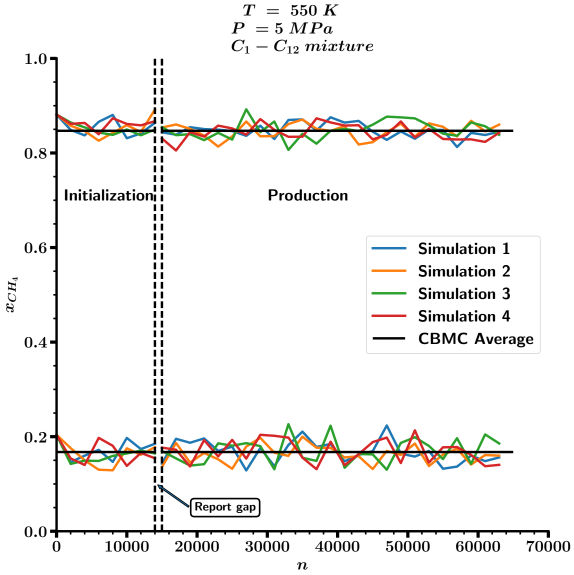

Figure A.24: Methane's mole fraction change as a function of Monte Carlo cycles at $T = 550\ K$ and at $P = 5\ MPa$

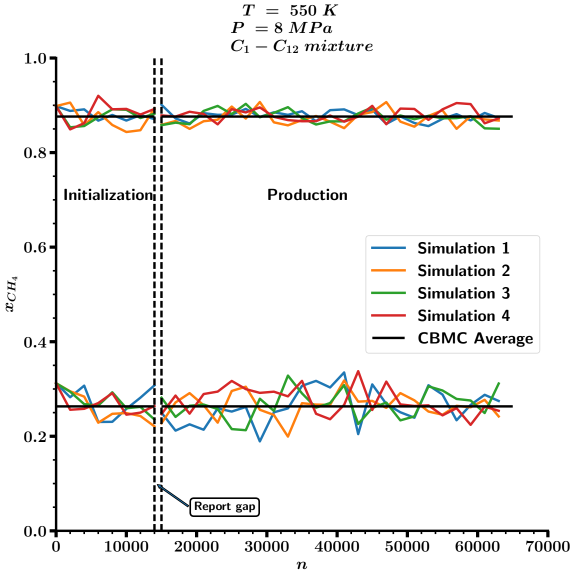

Figure A.25: Methane's mole fraction change as a function of Monte Carlo cycles at $T = 550\ K$ and at $P = 8\ MPa$

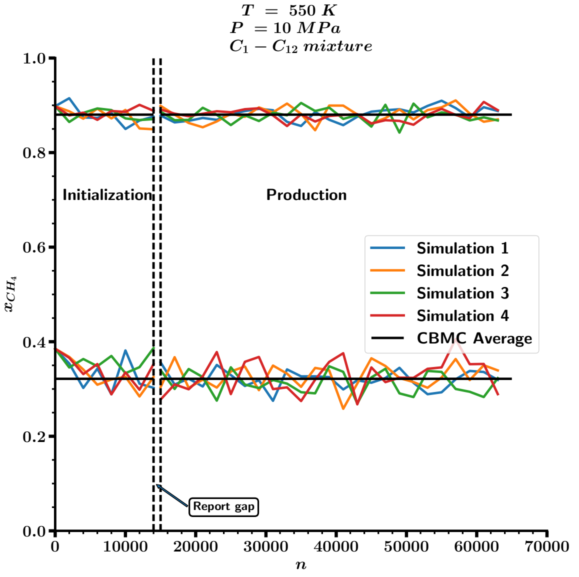

Figure A.26: Methane's mole fraction change as a function of Monte Carlo cycles at $T = 550\ K$ and at $P = 10\ MPa$

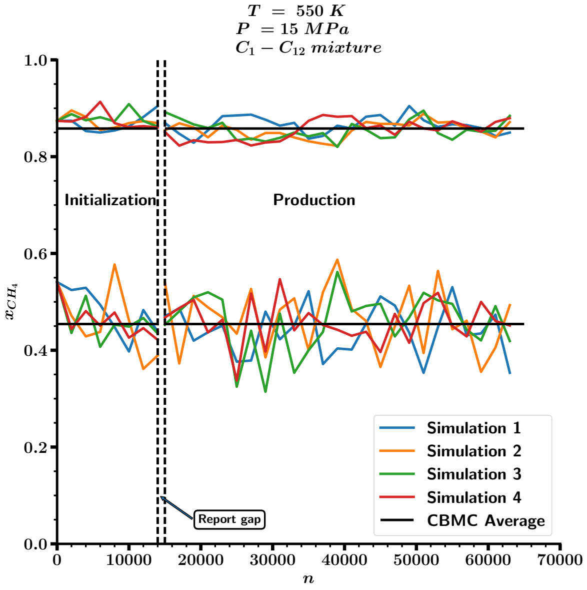

Figure A.27: Methane's mole fraction change as a function of Monte Carlo cycles at $T = 550\ K$ and at $P = 15\ MPa$

A.2. METHANE - TETRADECANE BINARY MIXTURE

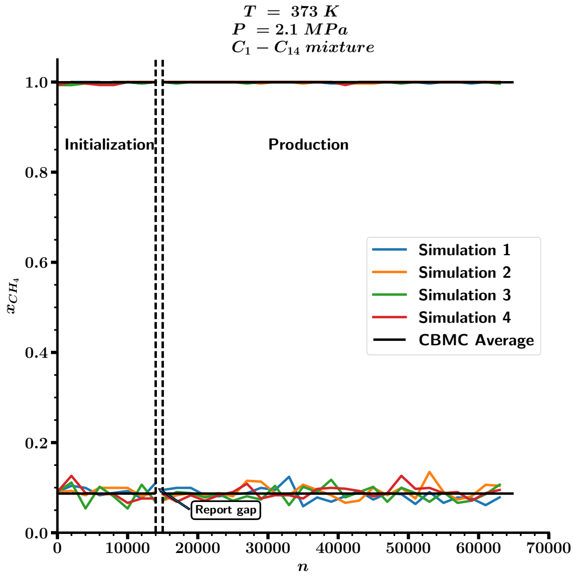

Figure A.28: Methane's mole fraction change as a function of Monte Carlo cycles at $T\ =\ 373\ K$ and at $P\ =\ 2.1\ MPa$

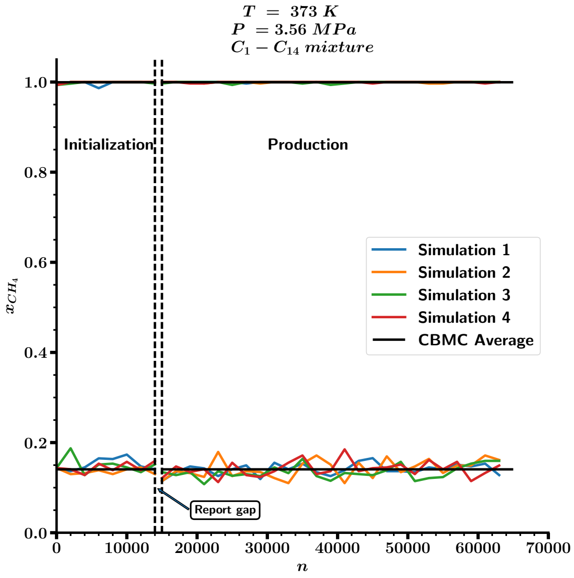

Figure A.29: Methane's mole fraction change as a function of Monte Carlo cycles at $T\ =\ 373\ K$ and at $P\ =\ 3.56\ MPa$

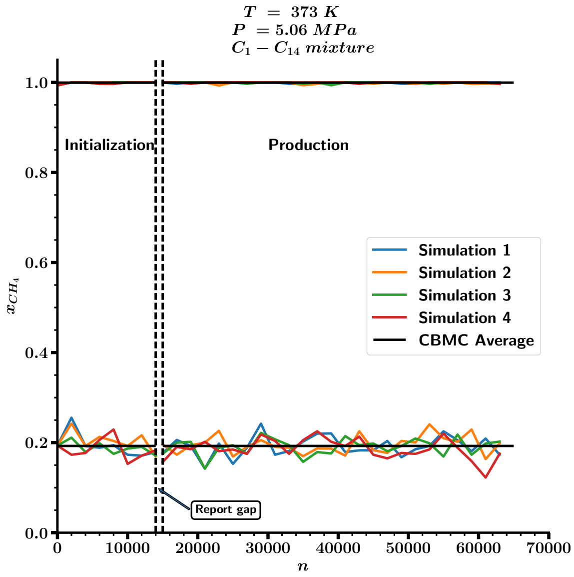

Figure A.30: Methane's mole fraction change as a function of Monte Carlo cycles at $T\ =\ 373\ K$ and at $P\ =\ 5.06\ MPa$

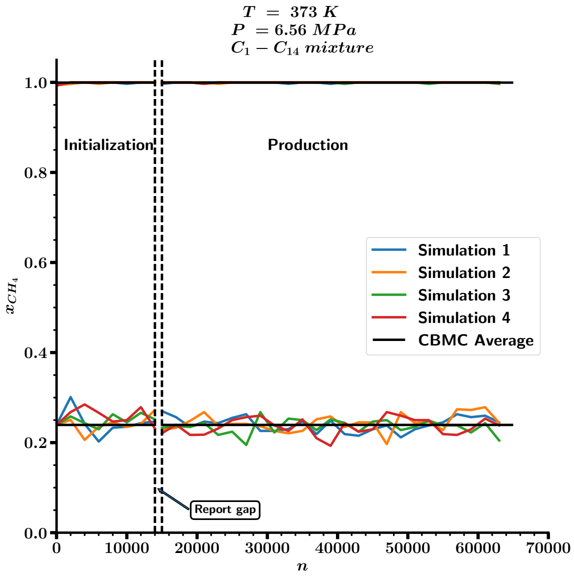

Figure A.31: Methane's mole fraction change as a function of Monte Carlo cycles at $T\ =\ 373\ K$ and at $P\ =\ 6.56\ MPa$

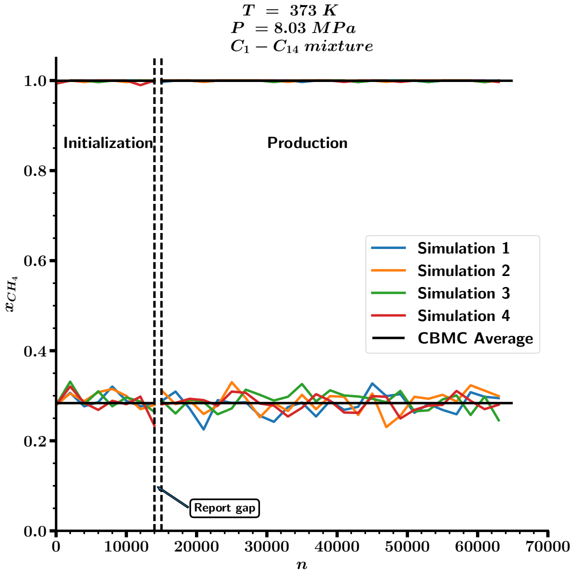

Figure A.32: Methane's mole fraction change as a function of Monte Carlo cycles at $T = 373\ K$ and at $P = 8.03\ MPa$

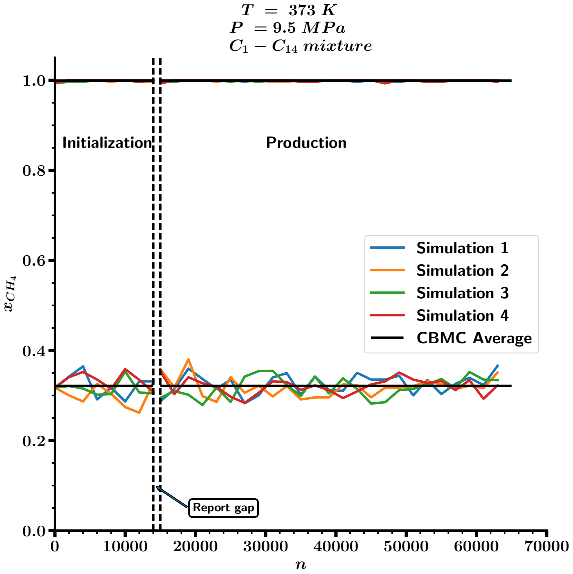

Figure A.33: Methane's mole fraction change as a function of Monte Carlo cycles at $T = 373\ K$ and at $P = 9.5\ MPa$

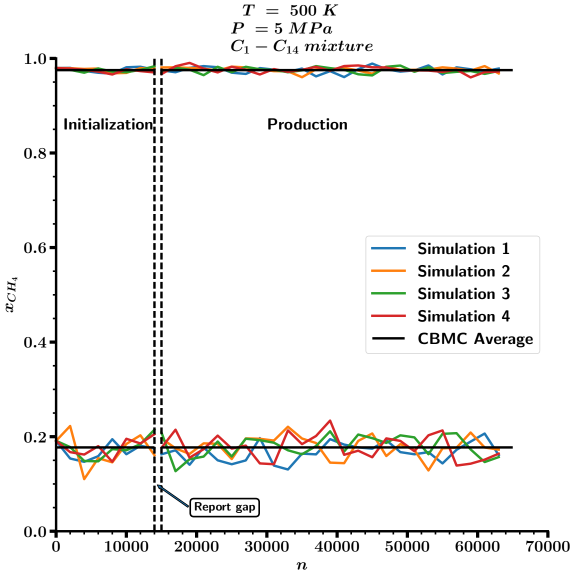

Figure A.34: Methane's mole fraction change as a function of Monte Carlo cycles at $T = 500\ K$ and at $P = 5\ MPa$

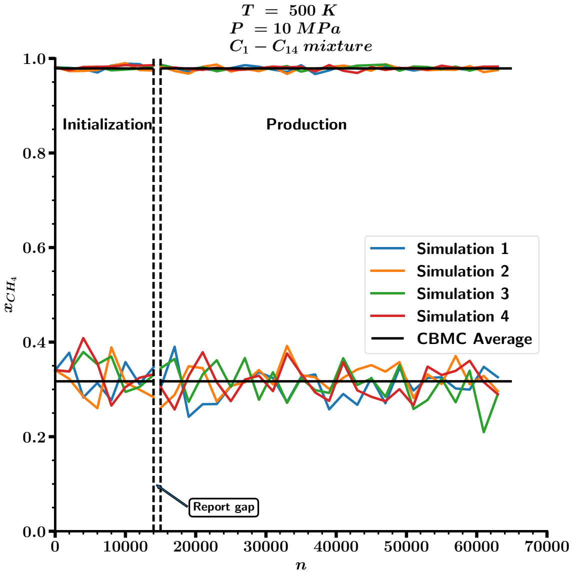

Figure A.35: Methane's mole fraction change as a function of Monte Carlo cycles at $T = 500\ K$ and at $P = 10\ MPa$

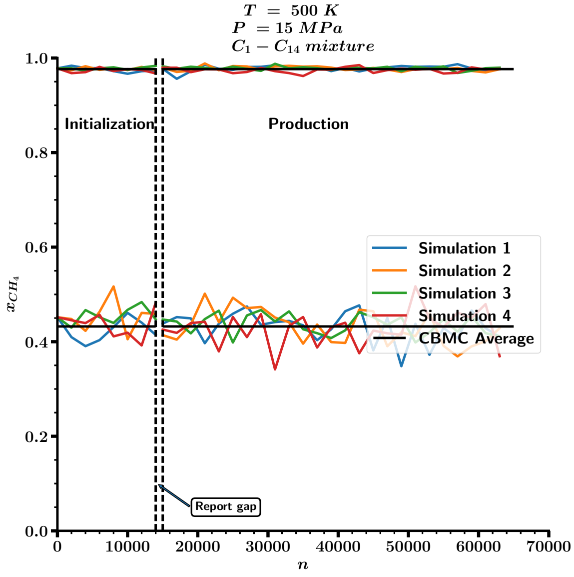

Figure A.36: Methane's mole fraction change as a function of Monte Carlo cycles at $T = 500\ K$ and at $P = 15\ MPa$

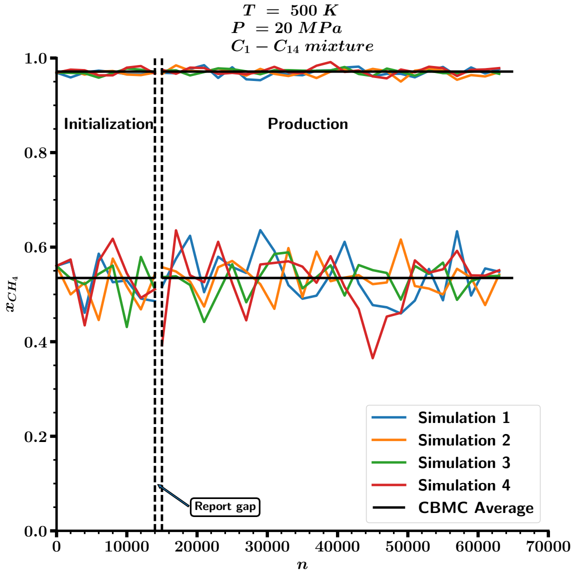

Figure A.37: Methane's mole fraction change as a function of Monte Carlo cycles at $T = 500\ K$ and at $P = 20\ MPa$

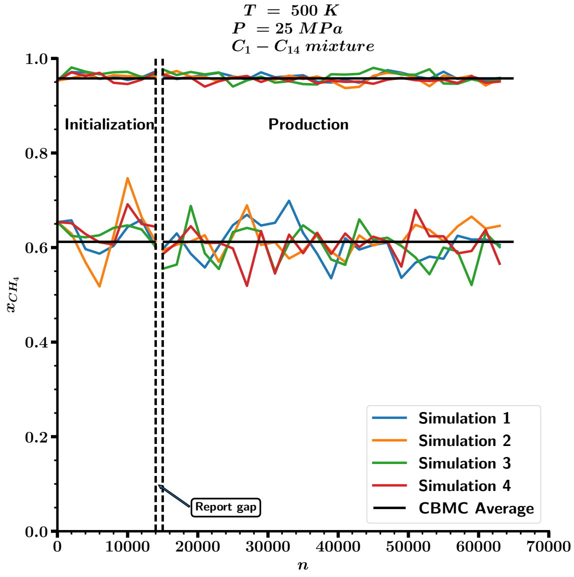

Figure A.38: Methane's mole fraction change as a function of Monte Carlo cycles at $T = 500\ K$ and at $P = 25\ MPa$

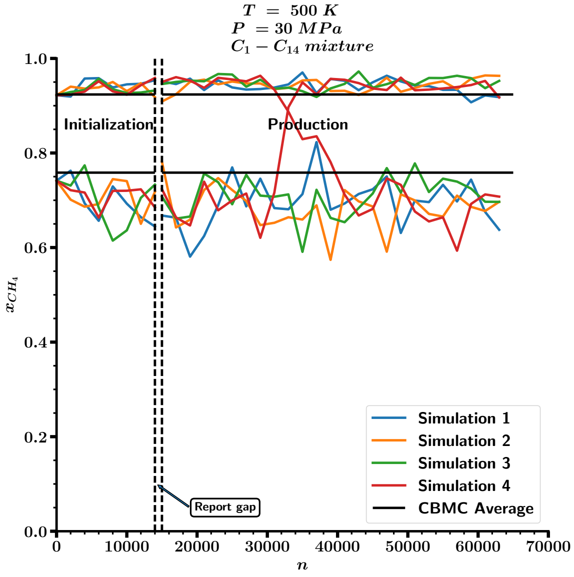

Figure A.39: Methane's mole fraction change as a function of Monte Carlo cycles at $T = 500\ K$ and at $P = 30\ MPa$

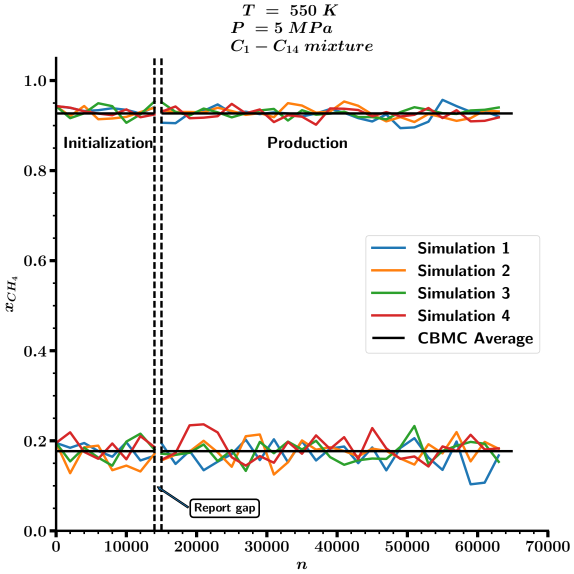

Figure A.40: Methane's mole fraction change as a function of Monte Carlo cycles at $T = 550\ K$ and at $P = 5\ MPa$

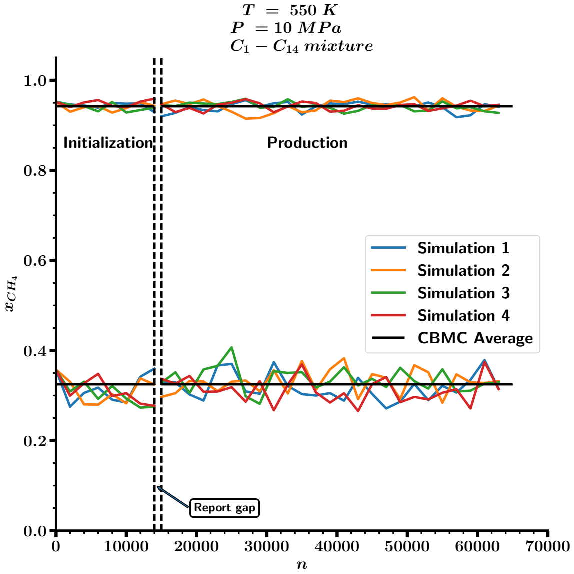

Figure A.41: Methane's mole fraction change as a function of Monte Carlo cycles at $T = 550\ K$ and at $P = 10\ MPa$

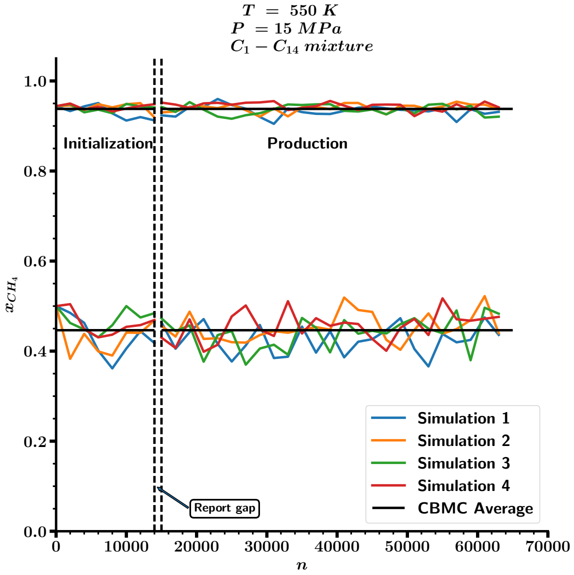

Figure A.42: Methane's mole fraction change as a function of Monte Carlo cycles at $T = 550\ K$ and at $P = 15\ MPa$

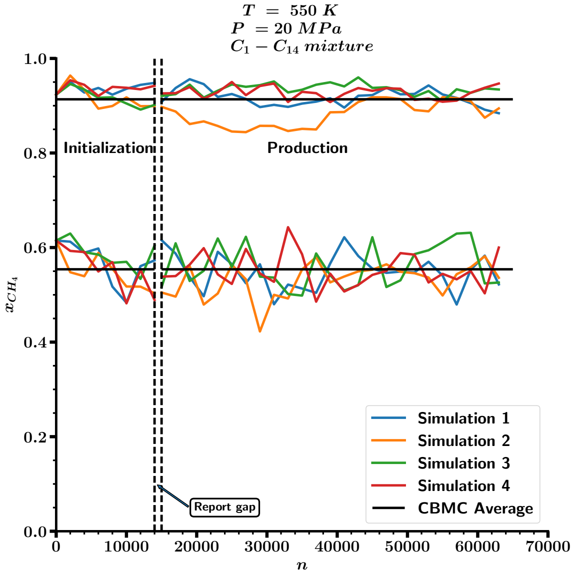

Figure A.43: Methane's mole fraction change as a function of Monte Carlo cycles at $T = 550\ K$ and at $P = 20\ MPa$

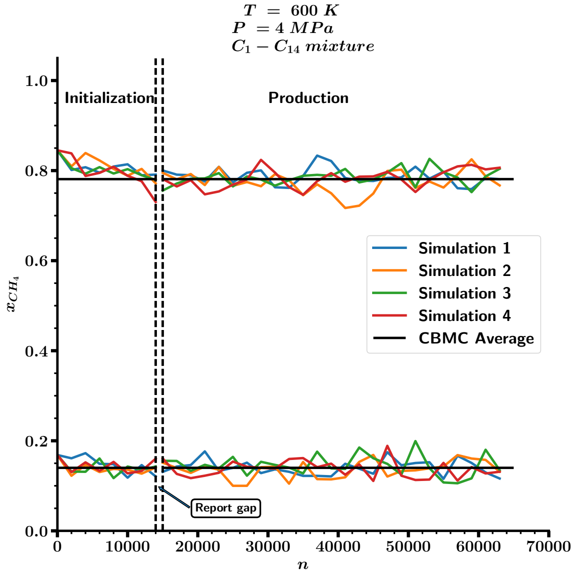

Figure A.44: Methane's mole fraction change as a function of Monte Carlo cycles at $T\ =\ 600\ K$ and at $P\ =\ 4\ MPa$

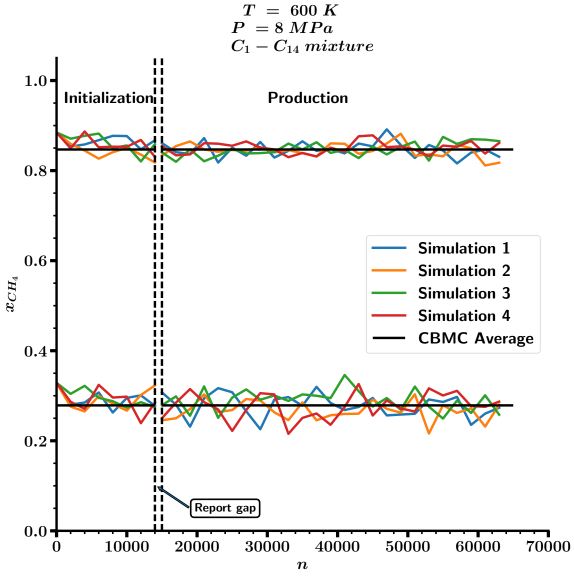

Figure A.45: Methane's mole fraction change as a function of Monte Carlo cycles at $T\ =\ 600\ K$ and at $P\ =\ 8\ MPa$

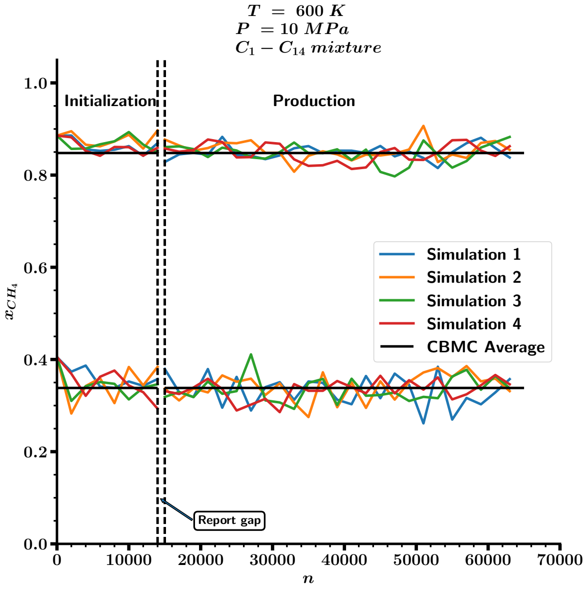

Figure A.46: Methane's mole fraction change as a function of Monte Carlo cycles at $T\ =\ 600\ K$ and at $P\ =\ 10\ MPa$

A.3. METHANE - HEXADECANE BINARY MIXTURE

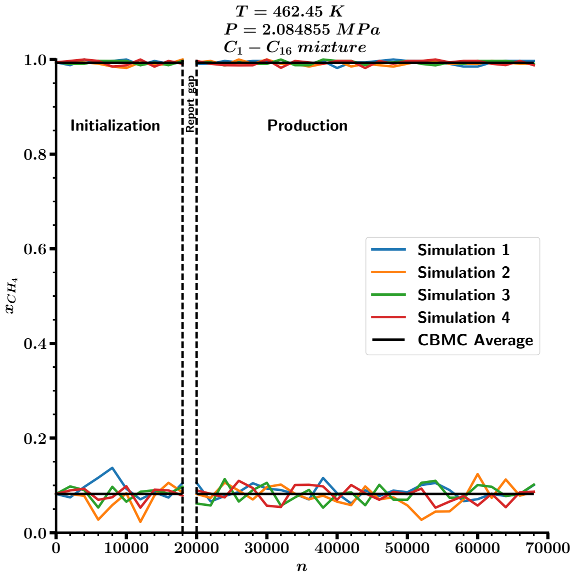

Figure A.47: Methane's mole fraction change as a function of Monte Carlo cycles at $T = 462.45\ K$ and at $P = 2.08\ MPa$

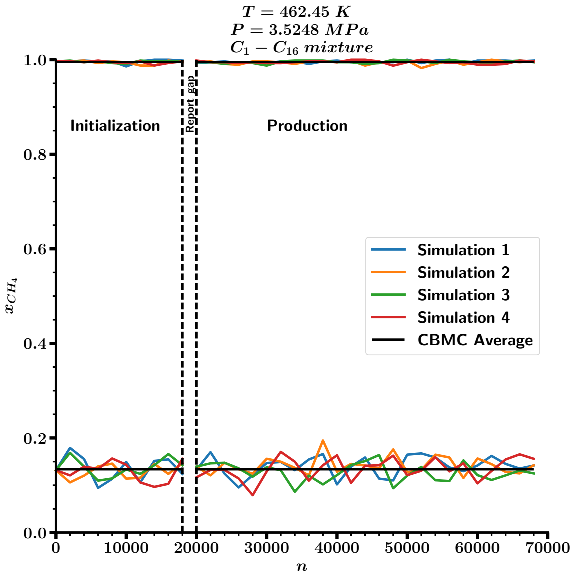

Figure A.48: Methane's mole fraction change as a function of Monte Carlo cycles at $T = 462.45\ K$ and at $P = 3.52\ MPa$

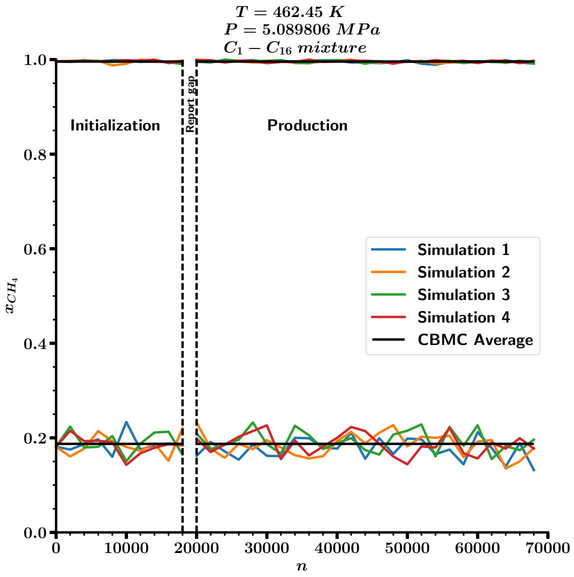

Figure A.49: Methane's mole fraction change as a function of Monte Carlo cycles at $T = 462.45\ K$ and at $P = 5.089\ MPa$

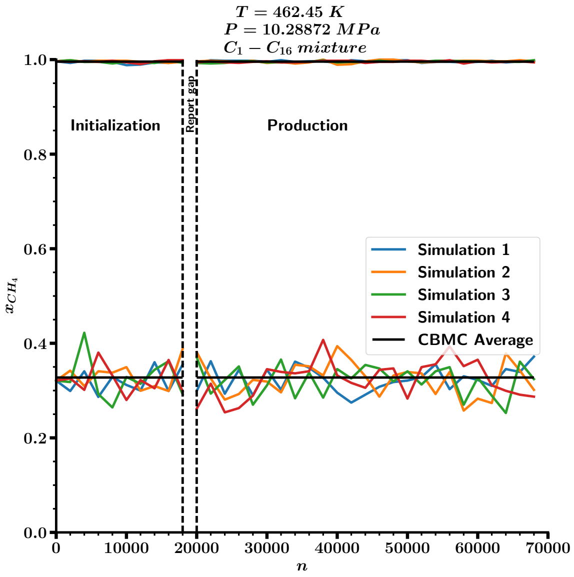

Figure A.50: Methane's mole fraction change as a function of Monte Carlo cycles at $T = 462.45\ K$ and at $P = 10.28\ MPa$

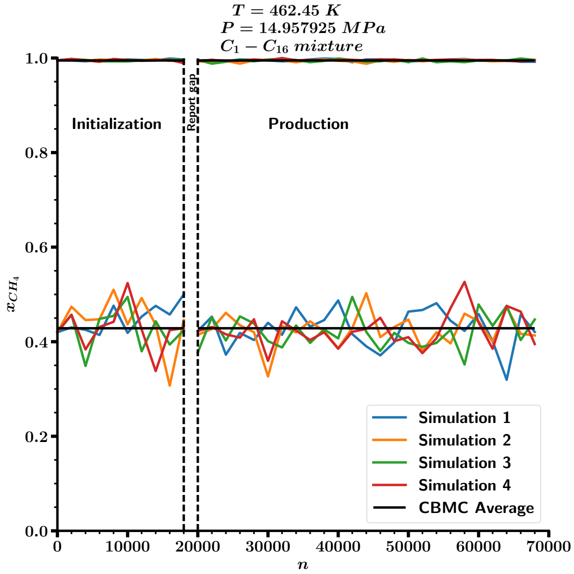

Figure A.51: Methane's mole fraction change as a function of Monte Carlo cycles at $T = 462.45\ K$ and at $P = 14.96\ MPa$

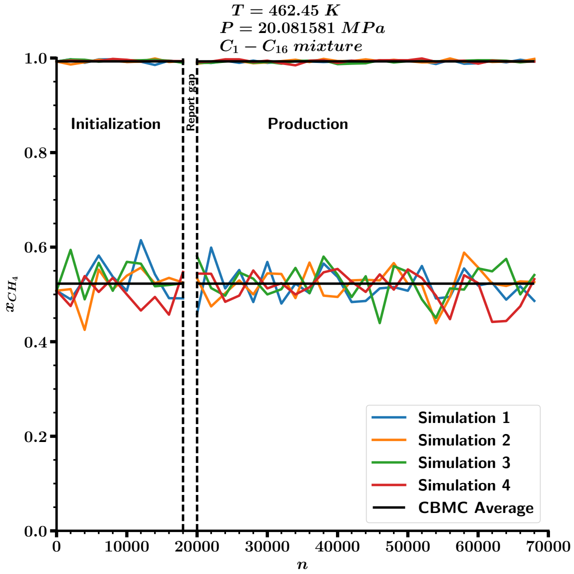

Figure A.52: Methane's mole fraction change as a function of Monte Carlo cycles at $T = 462.45\ K$ and at $P = 20.08\ MPa$

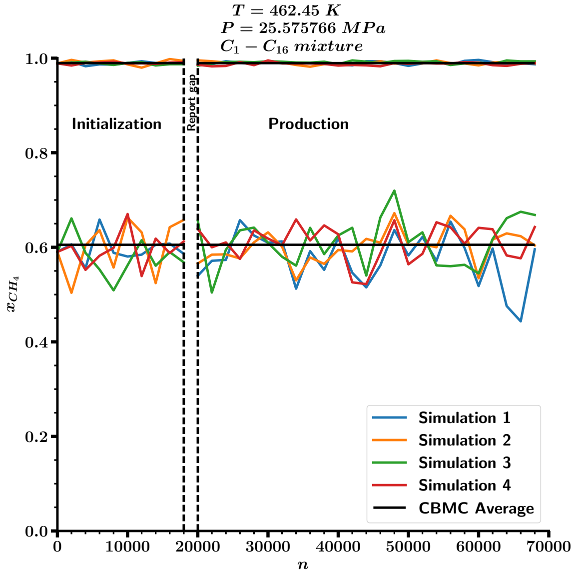

Figure A.53: Methane's mole fraction change as a function of Monte Carlo cycles at $T = 462.45\ K$ and at $P = 25.57\ MPa$

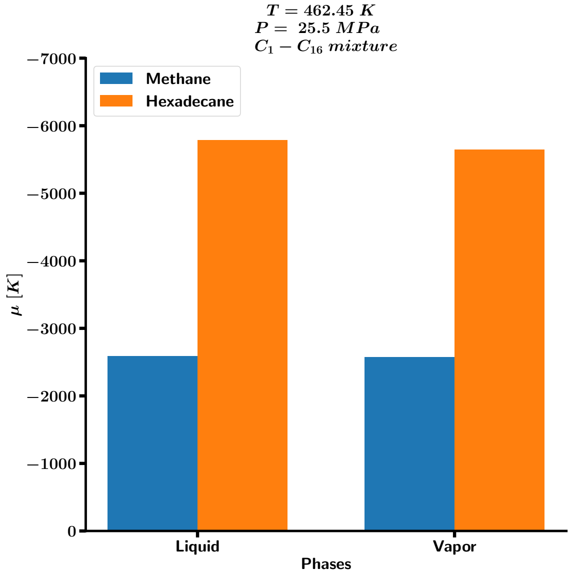

Figure A.54: Chemical potential of each component in both phase

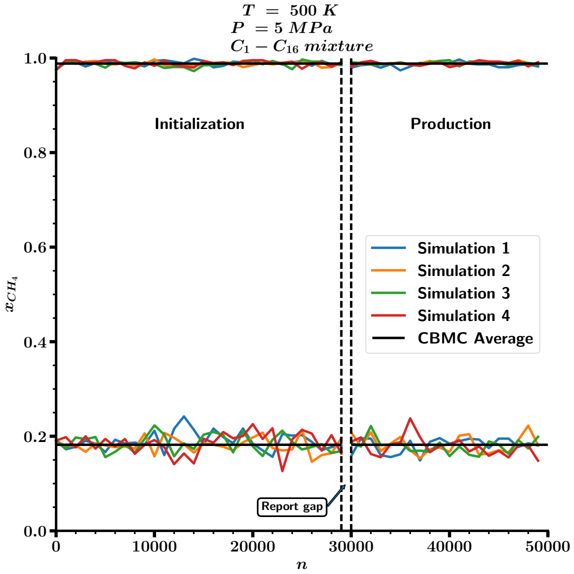

Figure A.55: Methane's mole fraction change as a function of Monte Carlo cycles at $T = 500\ K$ and at $P = 5\ MPa$

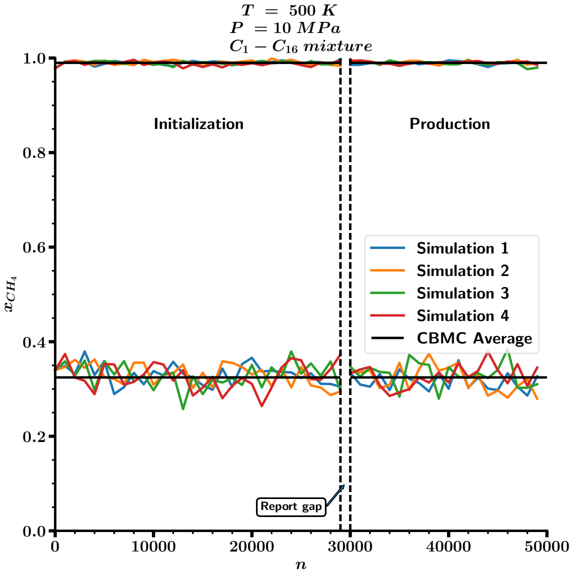

Figure A.56: Methane's mole fraction change as a function of Monte Carlo cycles at $T = 500\ K$ and at $P = 10\ MPa$

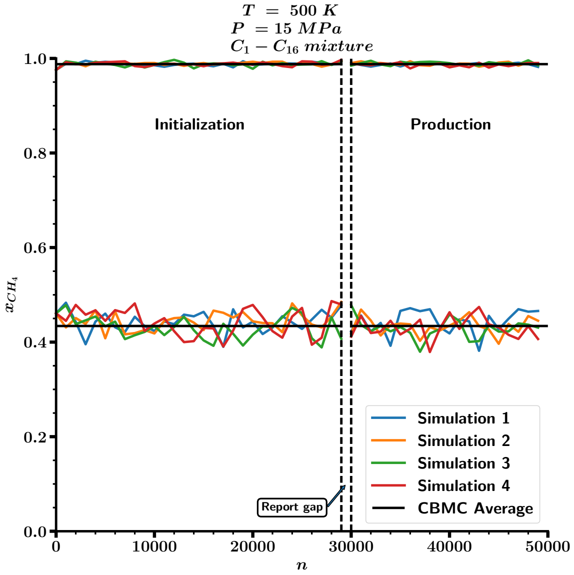

Figure A.57: Methane's mole fraction change as a function of Monte Carlo cycles at $T = 500\ K$ and at $P = 15\ MPa$

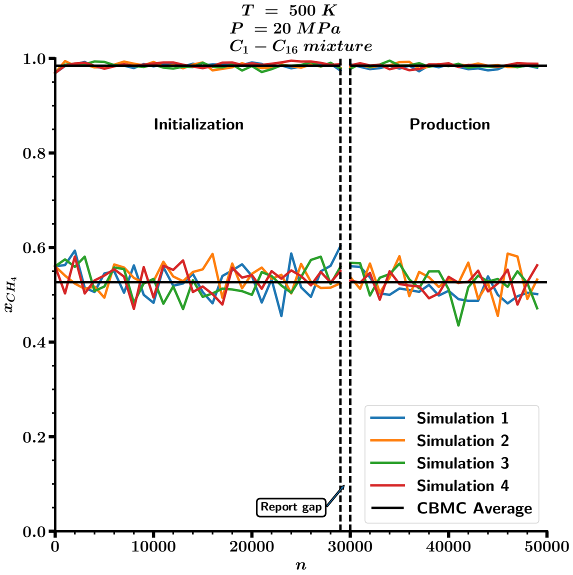

Figure A.58: Methane's mole fraction change as a function of Monte Carlo cycles at $T = 500\ K$ and at $P = 20\ MPa$

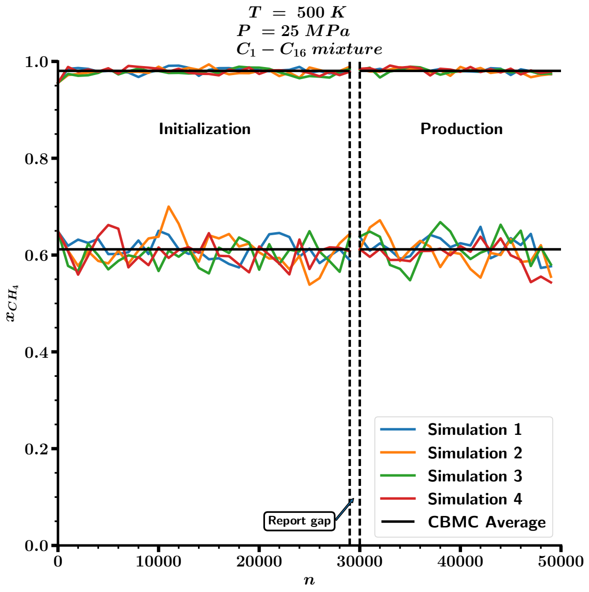

Figure A.59: Methane's mole fraction change as a function of Monte Carlo cycles at $T\ =\ 500\ K$ and at $P\ =\ 25\ MPa$

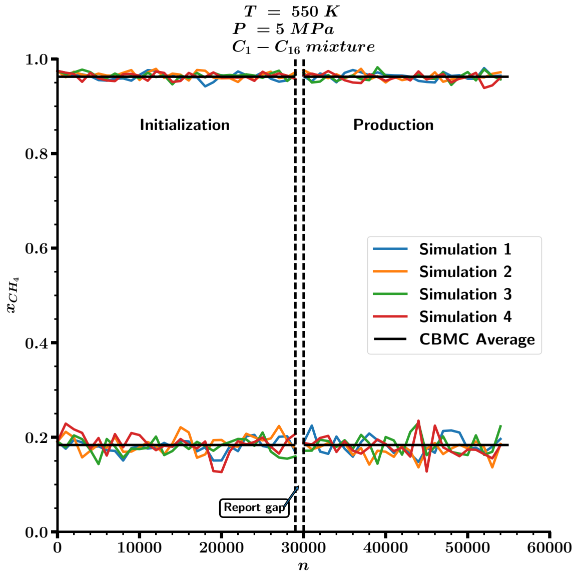

Figure A.60: Methane's mole fraction change as a function of Monte Carlo cycles at $T\ =\ 550\ K$ and at $P\ =\ 5\ MPa$

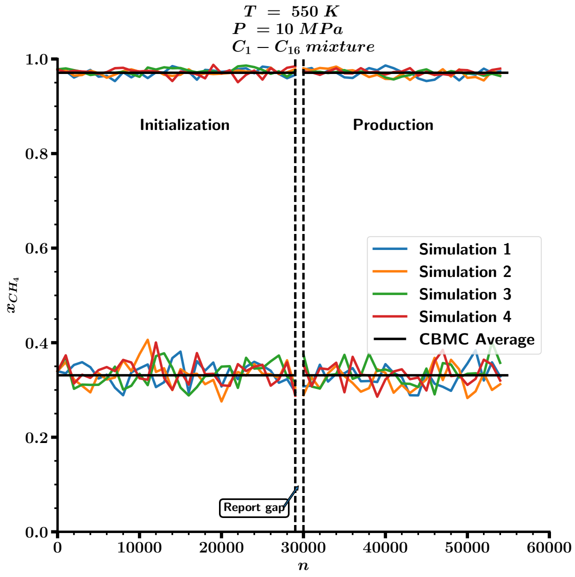

Figure A.61: Methane's mole fraction change as a function of Monte Carlo cycles at $T\ =\ 550\ K$ and at $P\ =\ 10\ MPa$

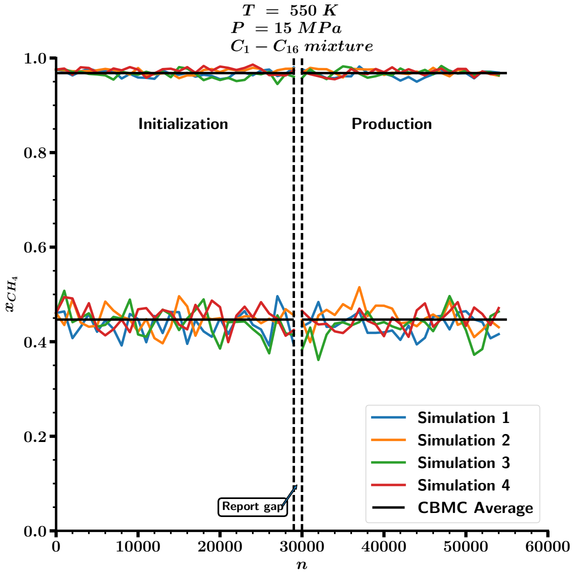

Figure A.62: Methane's mole fraction change as a function of Monte Carlo cycles at $T\ =\ 550\ K$ and at $P\ =\ 15\ MPa$

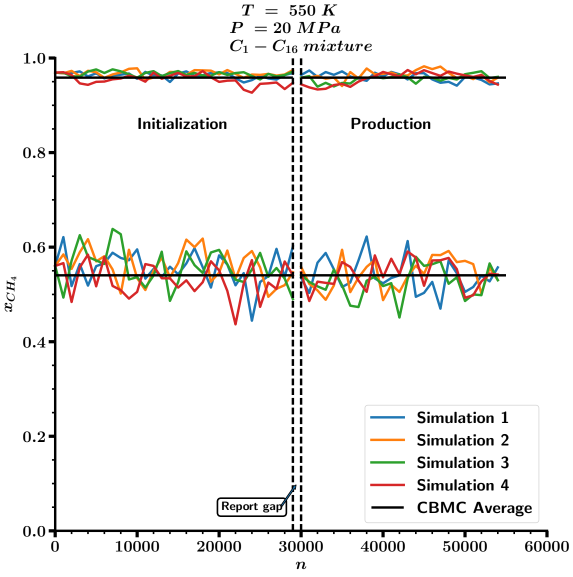

Figure A.63: Methane's mole fraction change as a function of Monte Carlo cycles at $T\ =\ 550\ K$ and at $P\ =\ 20\ MPa$

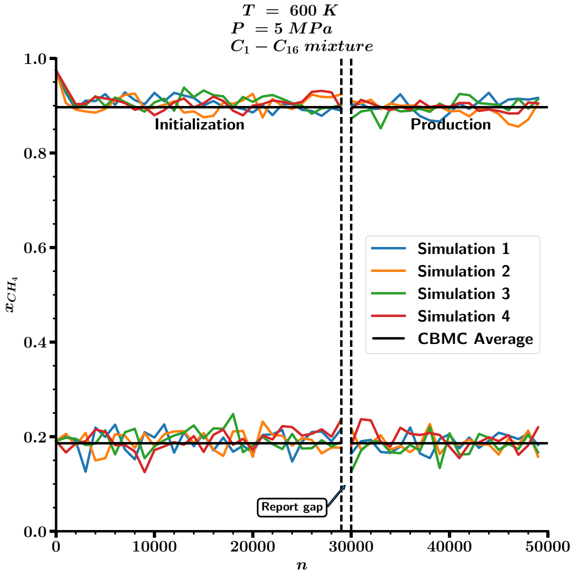

Figure A.64: Methane's mole fraction change as a function of Monte Carlo cycles at $T\ =\ 600\ K$ and at $P\ =\ 5\ MPa$

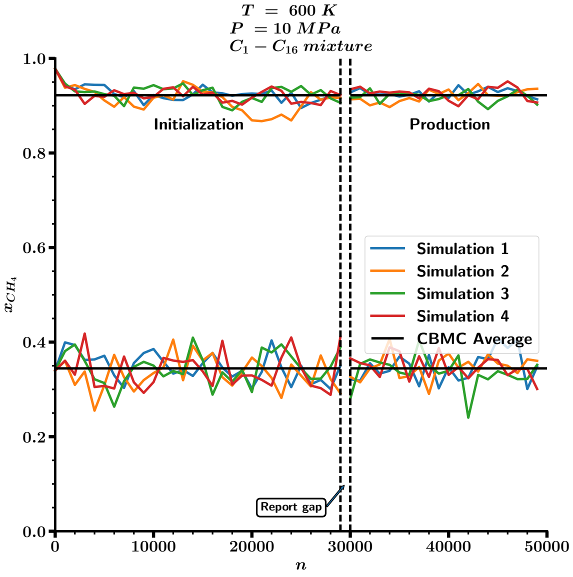

Figure A.65: Methane's mole fraction change as a function of Monte Carlo cycles at $T\ =\ 600\ K$ and at $P\ =\ 10\ MPa$

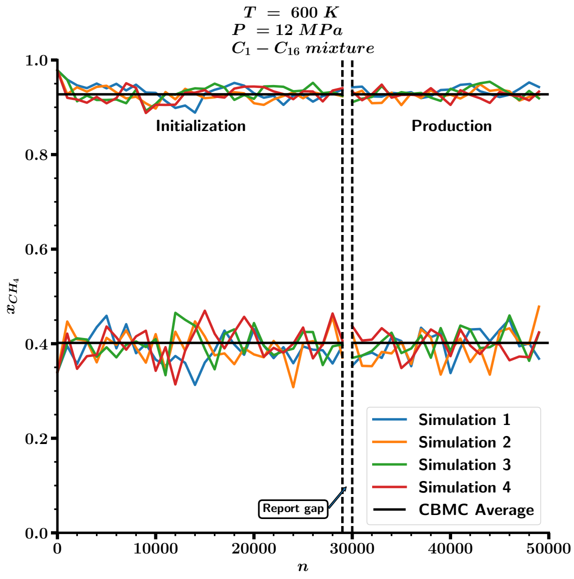

Figure A.66: Methane's mole fraction change as a function of Monte Carlo cycles at $T\ =\ 600\ K$ and at $P\ =\ 12\ MPa$

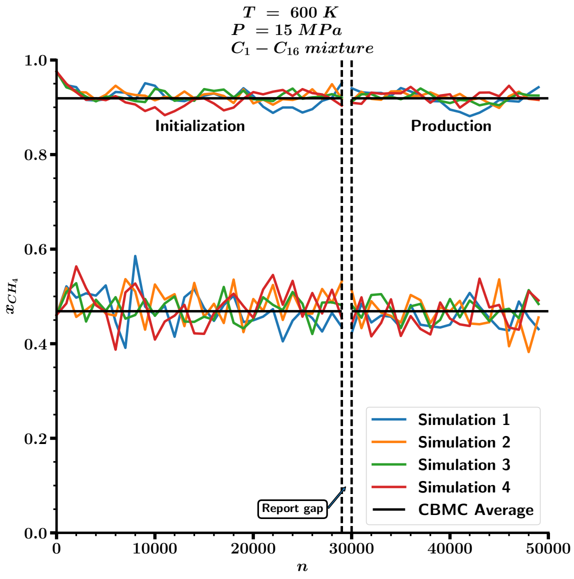

Figure A.67: Methane's mole fraction change as a function of Monte Carlo cycles at $T\ =\ 600\ K$ and at $P\ =\ 15\ MPa$

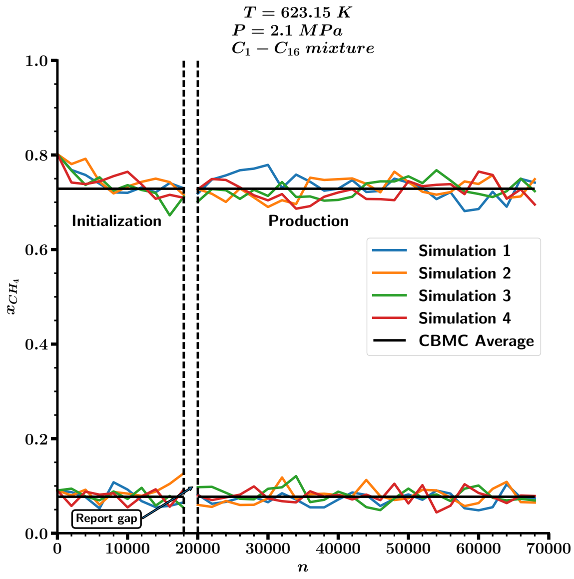

Figure A.68: Methane's mole fraction change as a function of Monte Carlo cycles at $T\ =\ 623.15\ K$ and at $P\ =\ 2.13\ MPa$

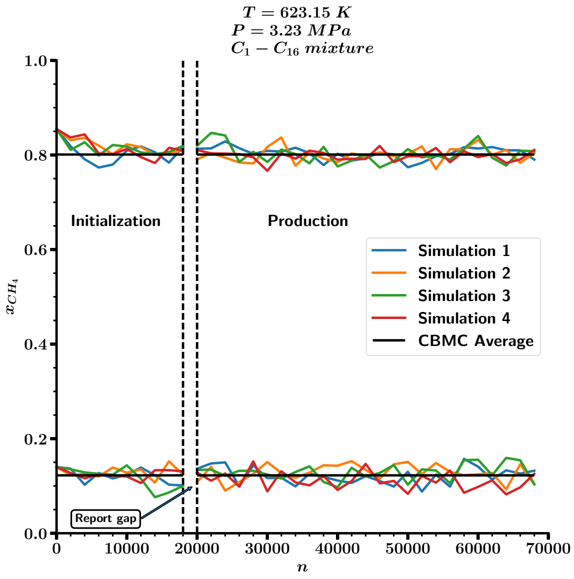

Figure A.69: Methane's mole fraction change as a function of Monte Carlo cycles at $T\ =\ 623.15\ K$ and at $P\ =\ 3.23\ MPa$

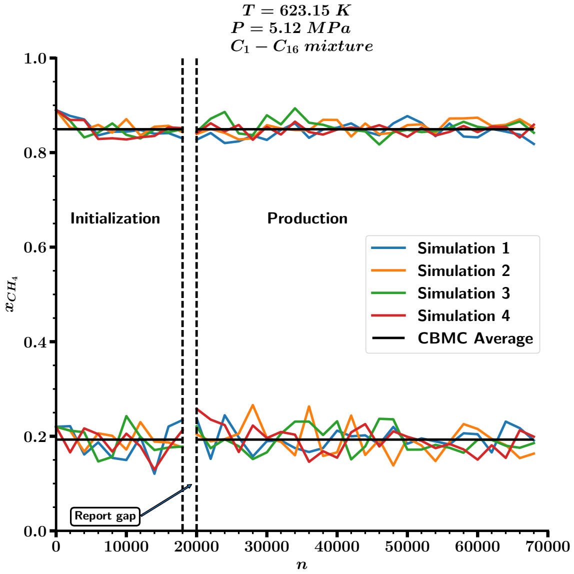

Figure A.70: Methane's mole fraction change as a function of Monte Carlo cycles at $T = 623.15\ K$ and at $P = 5.12\ MPa$

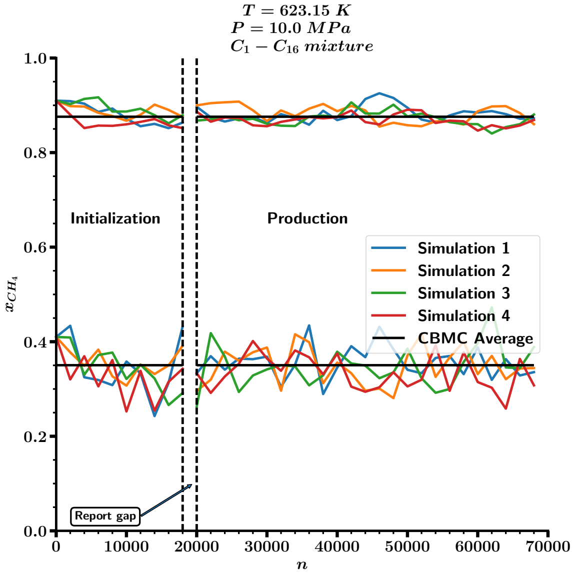

Figure A.71: Methane's mole fraction change as a function of Monte Carlo cycles at $T = 623.15\ K$ and at $P = 10.03\ MPa$

A.4. METHANE - ICOSANE BINARY MIXTURE

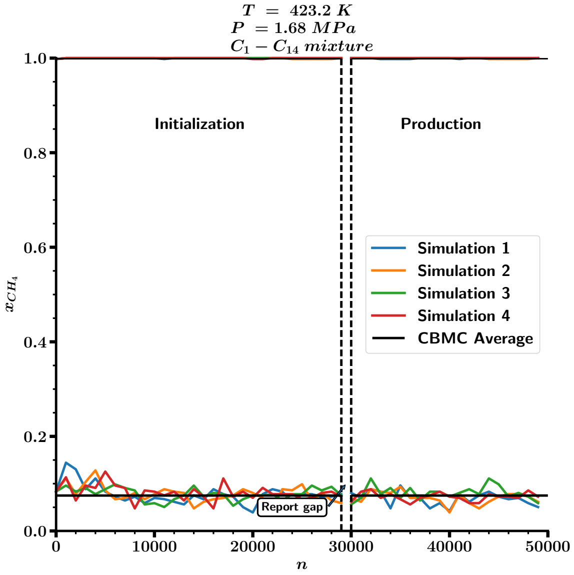

Figure A.72: Methane's mole fraction change as a function of Monte Carlo cycles at $T = 423.2\ K$ and at $P = 1.68\ MPa$

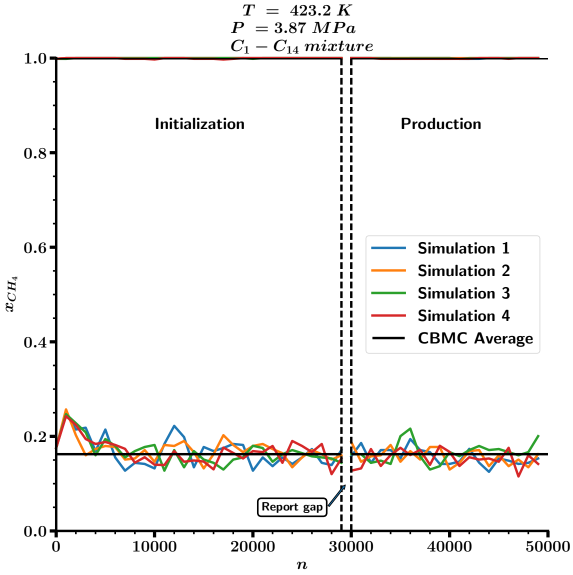

Figure A.73: Methane's mole fraction change as a function of Monte Carlo cycles at $T = 423.2\ K$ and at $P = 3.87\ MPa$

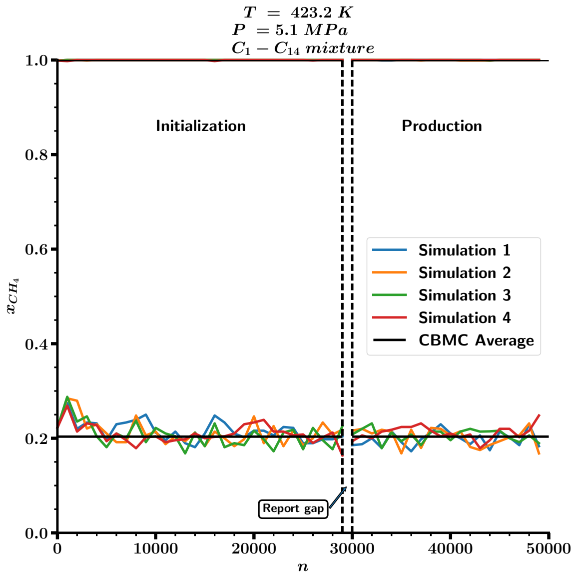

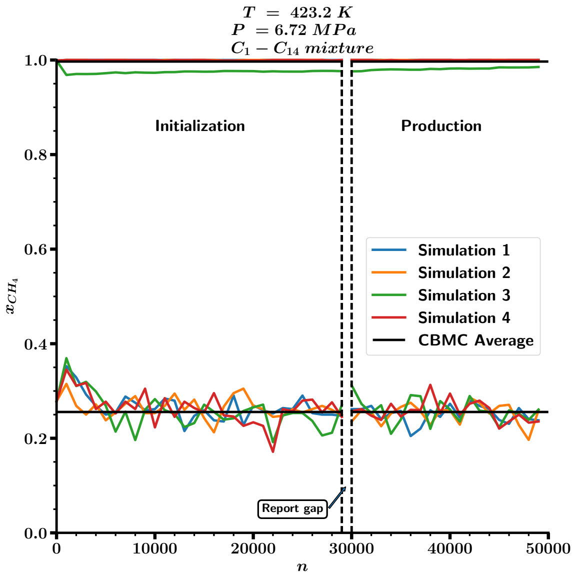

Figure A.74: Methane's mole fraction change as a function of Monte Carlo cycles at $T\ =\ 423.2\ K$ and at $P\ =\ 5.1\ MPa$

Figure A.75: Methane's mole fraction change as a function of Monte Carlo cycles at $T\ =\ 423.2\ K$ and at $P\ =\ 6.72\ MPa$

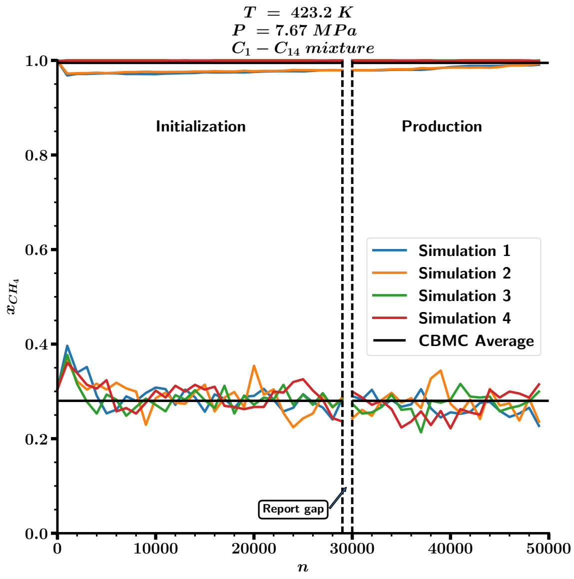

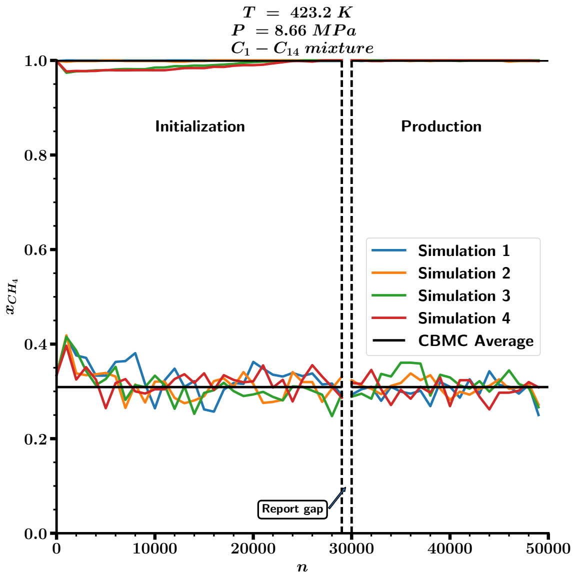

Figure A.76: Methane's mole fraction change as a function of Monte Carlo cycles at $T\ =\ 423.2\ K$ and at $P\ =\ 7.67\ MPa$

Figure A.77: Methane's mole fraction change as a function of Monte Carlo cycles at $T\ =\ 423.2\ K$ and at $P\ =\ 8.66\ MPa$

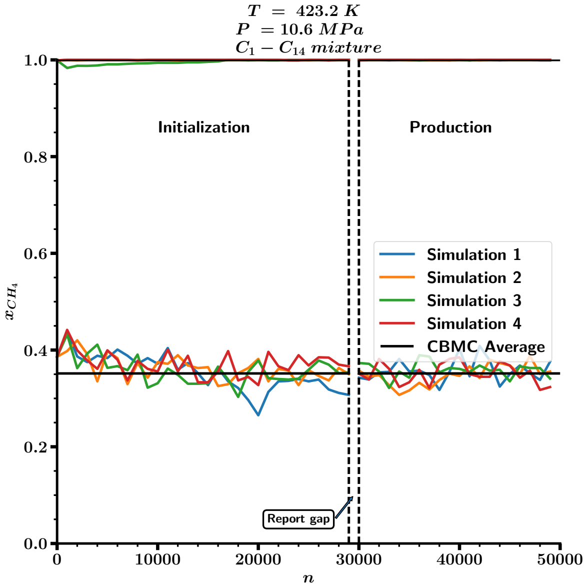

Figure A.78: Methane's mole fraction change as a function of Monte Carlo cycles at $T = 423\ K$ and at $P = 10.6\ MPa$

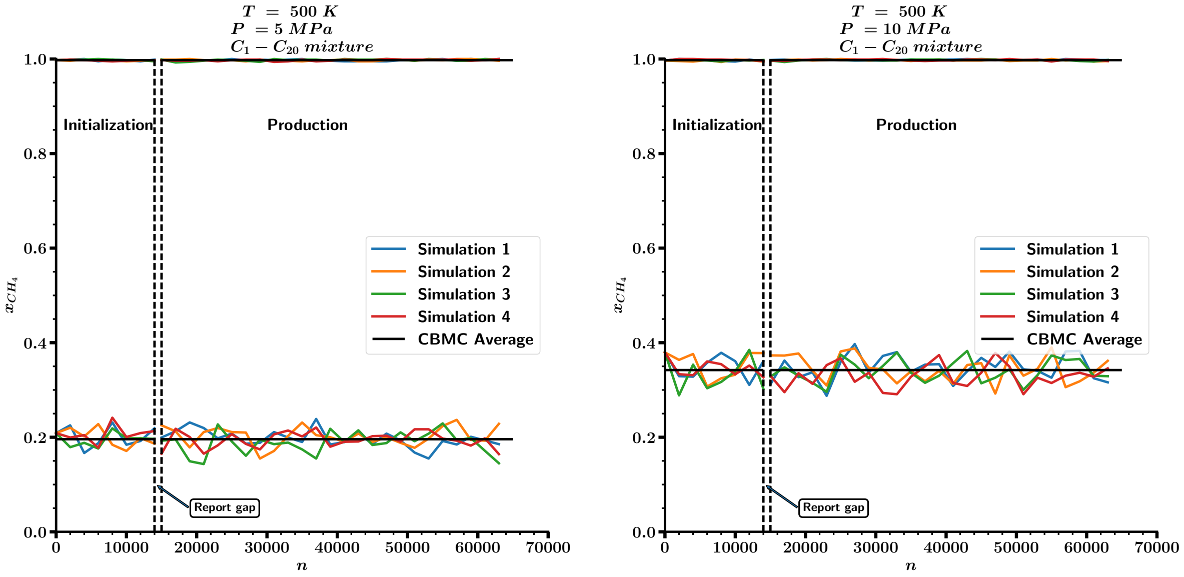

Figure A.79: Methane's mole fraction change as a function of Monte Carlo cycles at $T = 500\ K$ and at $P = 5\ MPa$

Figure A.80: Simulated Methane compositions' change in the vapor and liquid phase in every simulation cycle at $T = 500\ K$ and at $P = 10\ MPa$

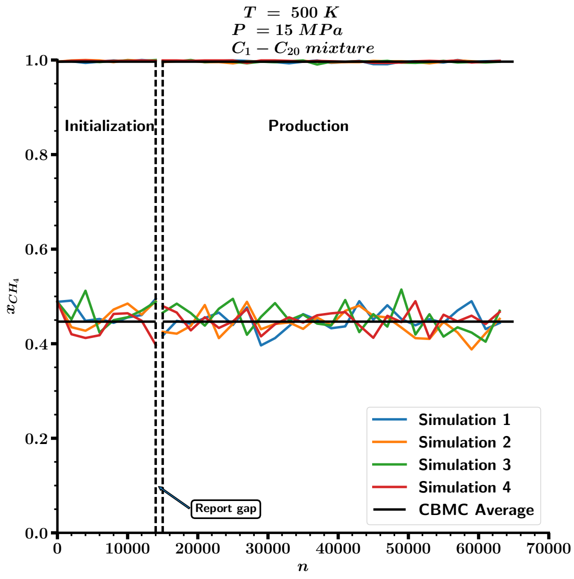

Figure A.81: Methane's mole fraction change as a function of Monte Carlo cycles at $T = 500\ K$ and at $P = 15\ MPa$

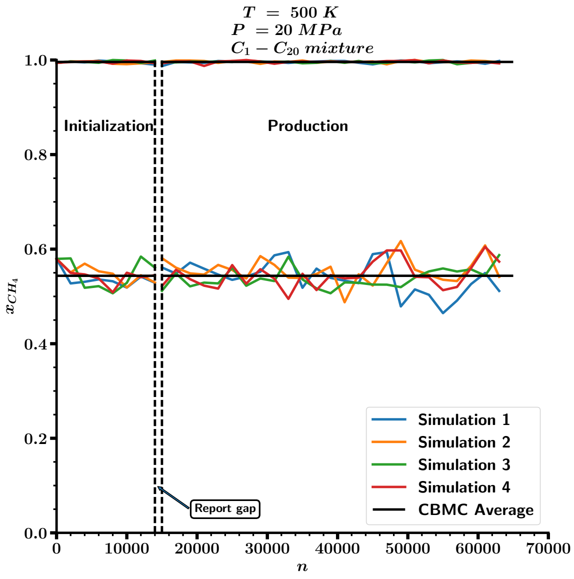

Figure A.82: Methane's mole fraction change as a function of Monte Carlo cycles at $T = 500\ K$ and at $P = 20\ MPa$

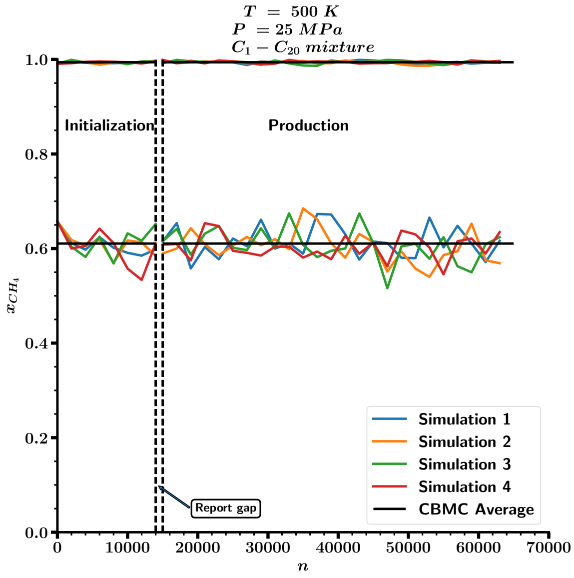

Figure A.83: Methane's mole fraction change as a function of Monte Carlo cycles at $T = 500\ K$ and at $P = 25\ MPa$

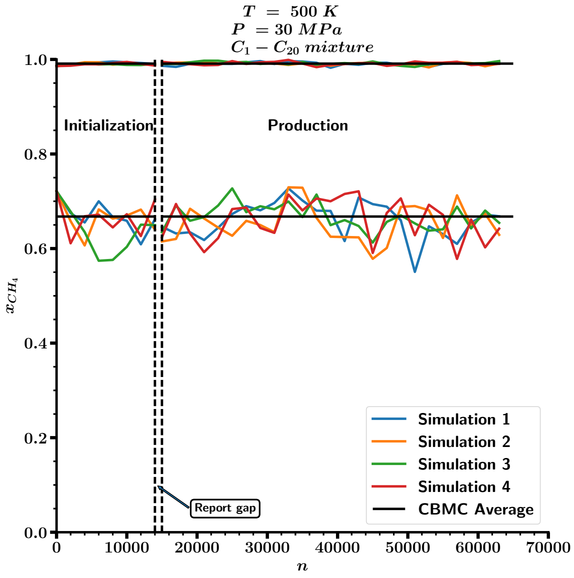

Figure A.84: Methane's mole fraction change as a function of Monte Carlo cycles at $T = 500\ K$ and at $P = 30\ MPa$

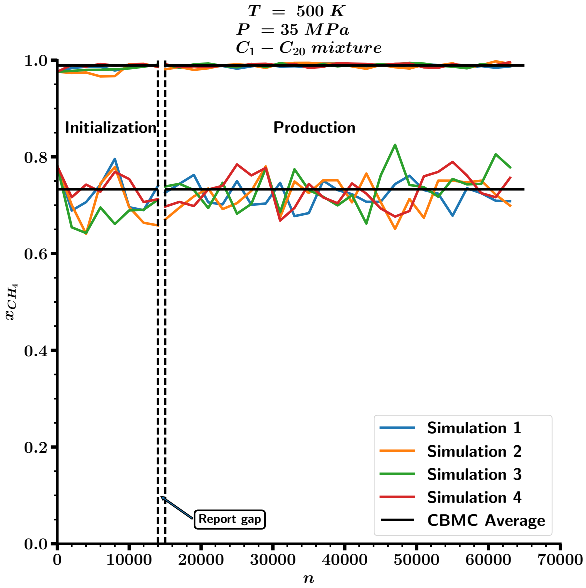

Figure A.85: Methane's mole fraction change as a function of Monte Carlo cycles at $T = 500\ K$ and at $P = 35\ MPa$

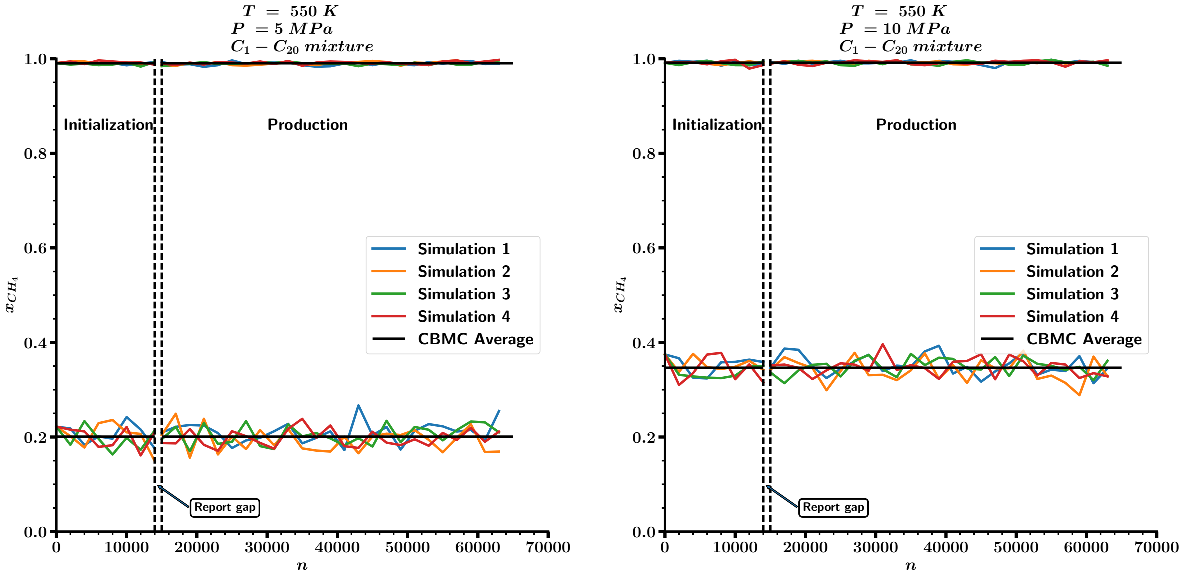

Figure A.86: Methane's mole fraction change as a function of Monte Carlo cycles at $T = 550\ K$ and at $P = 5\ MPa$

Figure A.87: Methane's mole fraction change as a function of Monte Carlo cycles at $T = 550\ K$ and at $P = 10\ MPa$

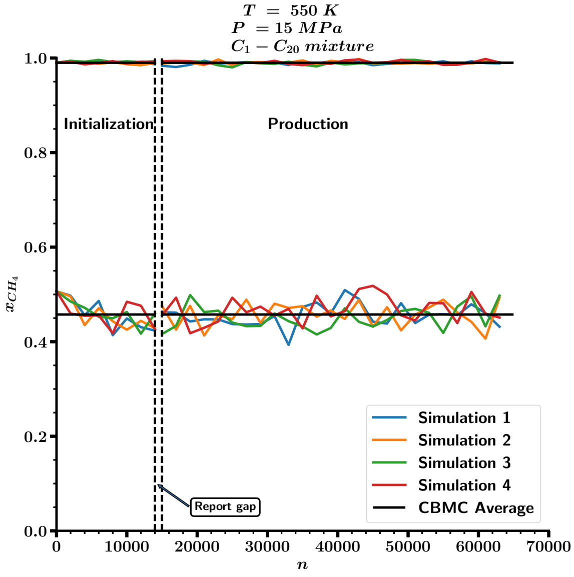

Figure A.88: Methane's mole fraction change as a function of Monte Carlo cycles at $T = 550\ K$ and at $P = 15\ MPa$

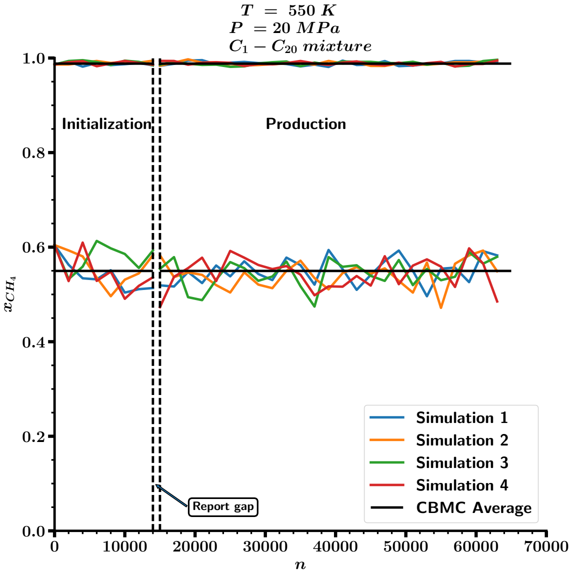

Figure A.89: Methane's mole fraction change as a function of Monte Carlo cycles at $T = 550\ K$ and at $P = 20\ MPa$

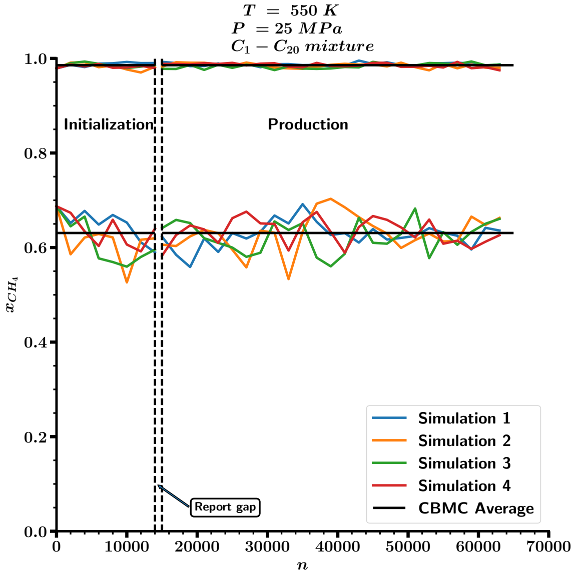

Figure A.90: Methane's mole fraction change as a function of Monte Carlo cycles at $T = 550\ K$ and at $P = 25\ MPa$

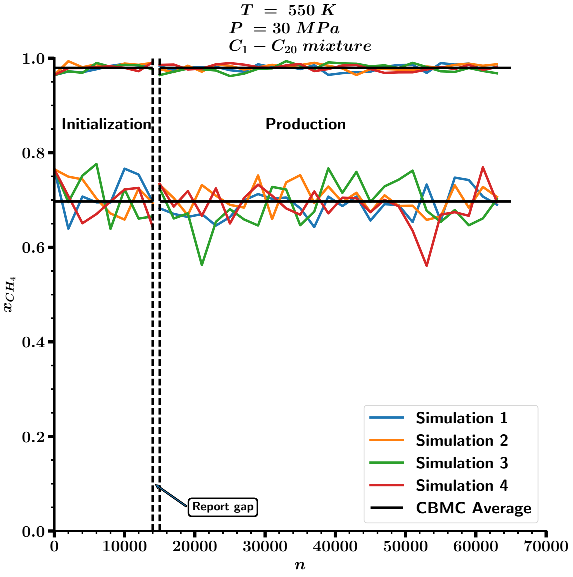

Figure A.91: Methane's mole fraction change as a function of Monte Carlo cycles at $T = 550\ K$ and at $P = 30\ MPa$

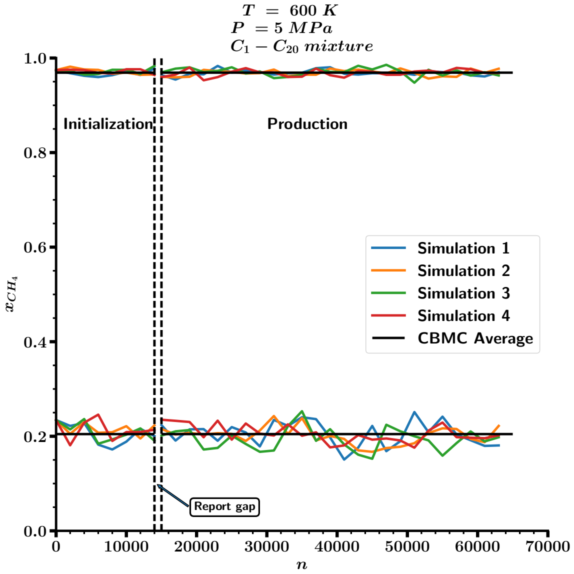

Figure A.92: Methane's mole fraction change as a function of Monte Carlo cycles at $T = 600\ K$ and at $P = 5\ MPa$

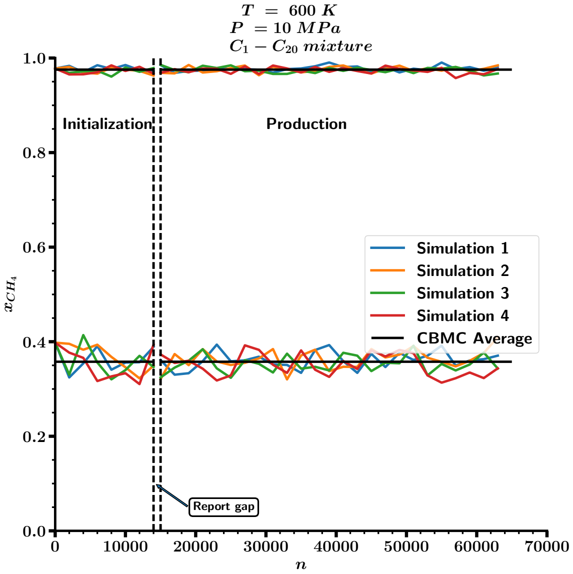

Figure A.93: Methane's mole fraction change as a function of Monte Carlo cycles at $T = 600\ K$ and at $P = 10\ MPa$

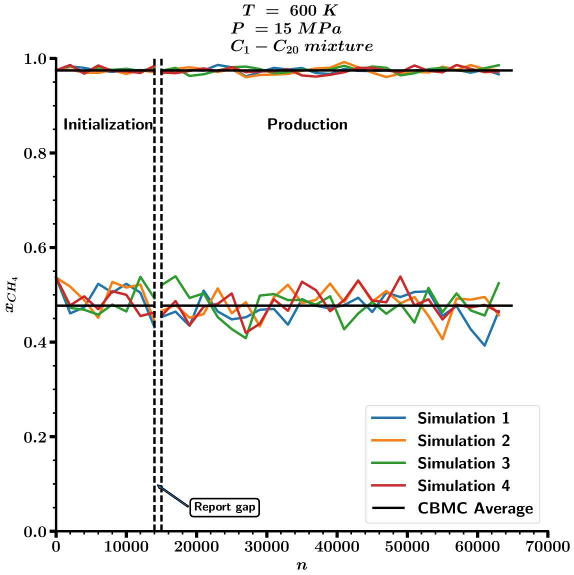

Figure A.94: Methane's mole fraction change as a function of Monte Carlo cycles at $T = 600\ K$ and at $P = 15\ MPa$

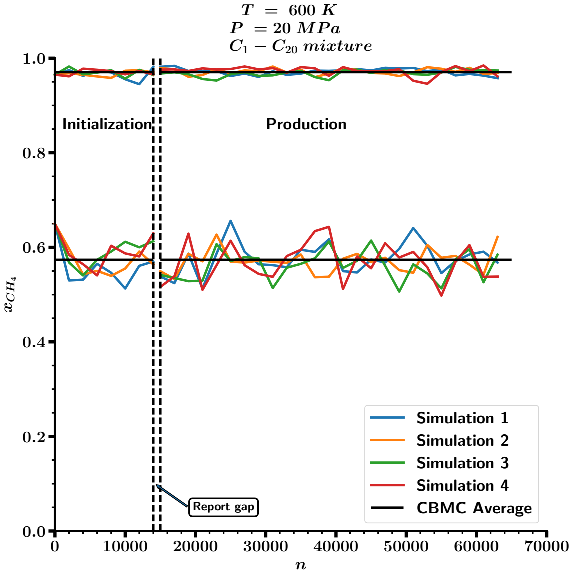

Figure A.95: Methane's mole fraction change as a function of Monte Carlo cycles at $T = 600\ K$ and at $P = 20\ MPa$

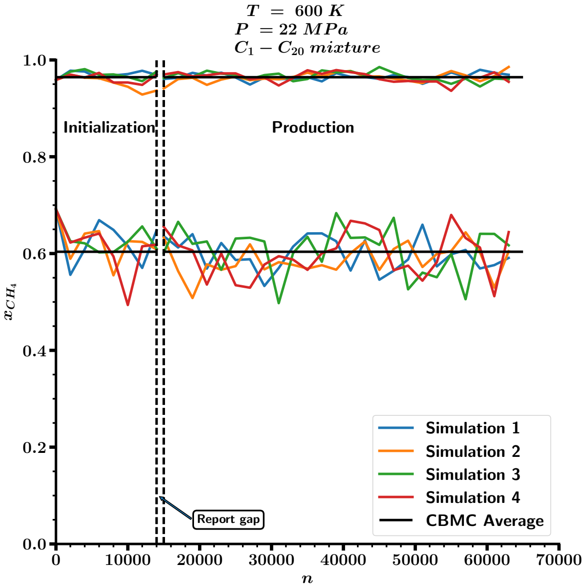

Figure A.96: Methane's mole fraction change as a function of Monte Carlo cycles at $T = 600\ K$ and at $P = 22\ MPa$

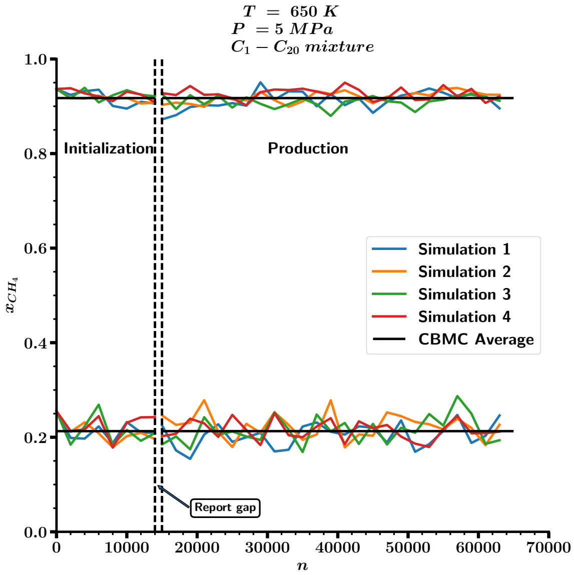

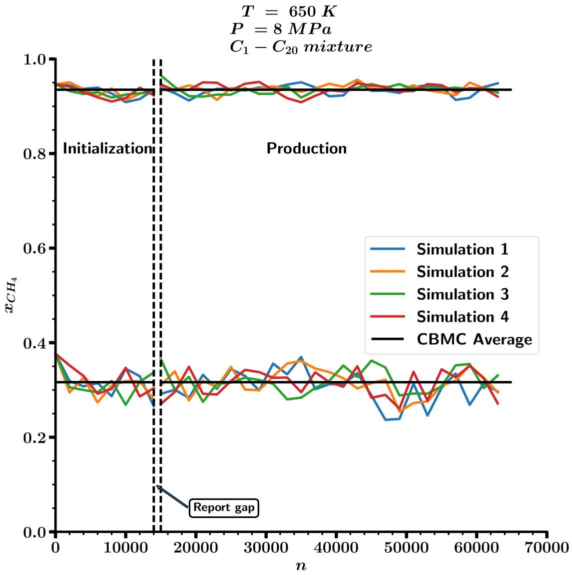

Figure A.97: Methane's mole fraction change as a function of Monte Carlo cycles at $T = 650\ K$ and at $P = 5\ MPa$

Figure A.98: Methane's mole fraction change as a function of Monte Carlo cycles at $T = 650\ K$ and at $P = 8\ MPa$

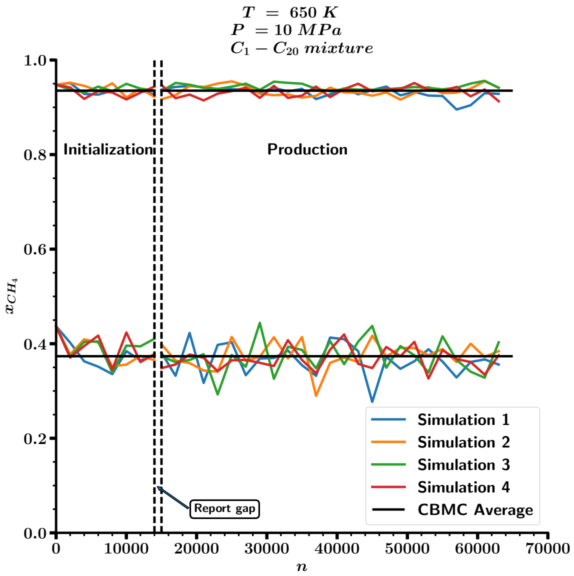

Figure A.99: Methane's mole fraction change as a function of Monte Carlo cycles at $T\ =\ 650\ K$ and at $P\ =\ 10\ MPa$

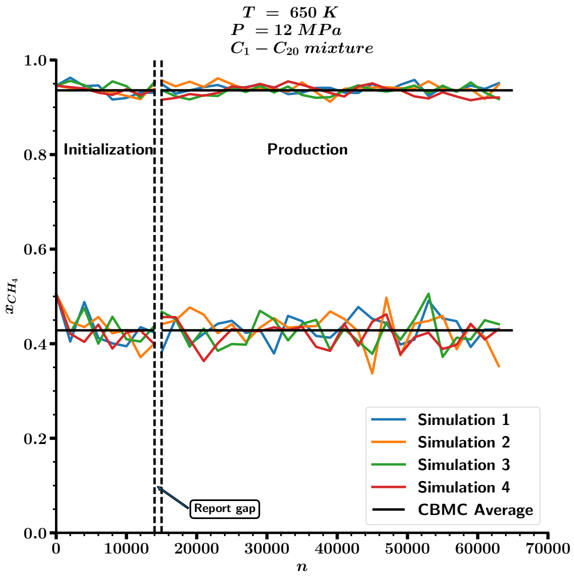

Figure A.100: Methane's mole fraction change as a function of Monte Carlo cycles at $T\ =\ 650\ K$ and at $P\ =\ 12\ MPa$

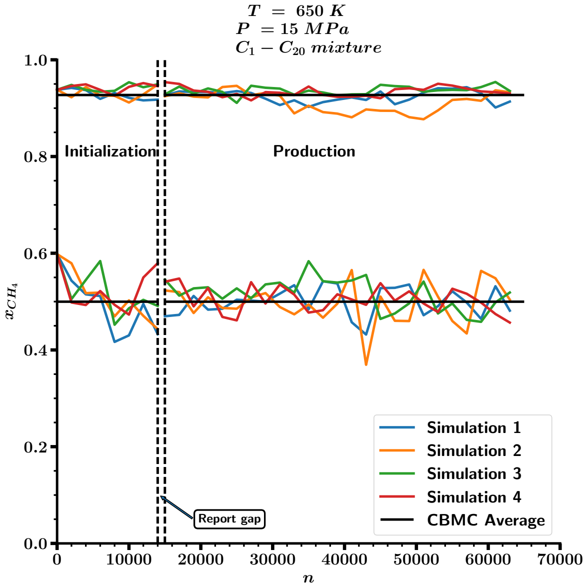

Figure A.101: Methane's mole fraction change as a function of Monte Carlo cycles at $T\ =\ 650\ K$ and at $P\ =\ 15\ MPa$

A.5. METHANE - TETRACOSANE BINARY MIXTURE

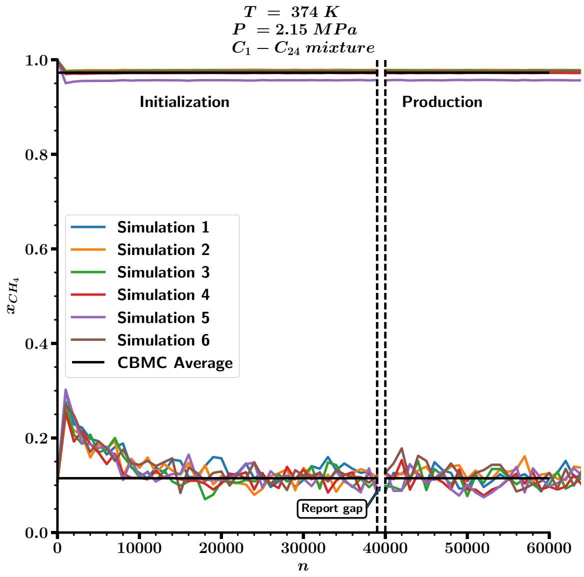

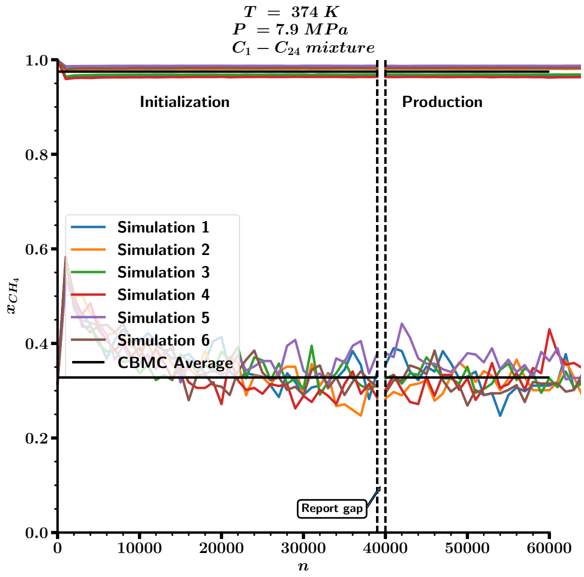

Figure A.102: Methane's mole fraction change as a function of Monte Carlo cycles at $T = 374\ K$ and at $P = 2.15\ MPa$

Figure A.103: Methane's mole fraction change as a function of Monte Carlo cycles at $T = 374\ K$ and at $P = 7.9\ MPa$

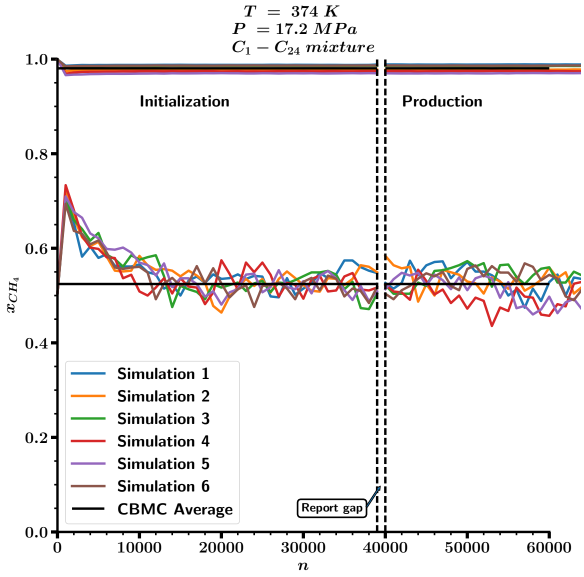

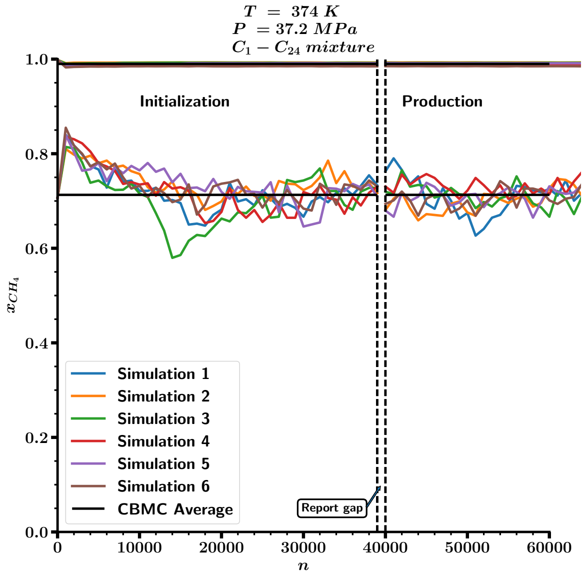

Figure A.104: Methane's mole fraction change as a function of Monte Carlo cycles at $T = 374\ K$ and at $P = 17.2\ MPa$

Figure A.105: Methane's mole fraction change as a function of Monte Carlo cycles at $T = 374\ K$ and at $P = 37.2\ MPa$

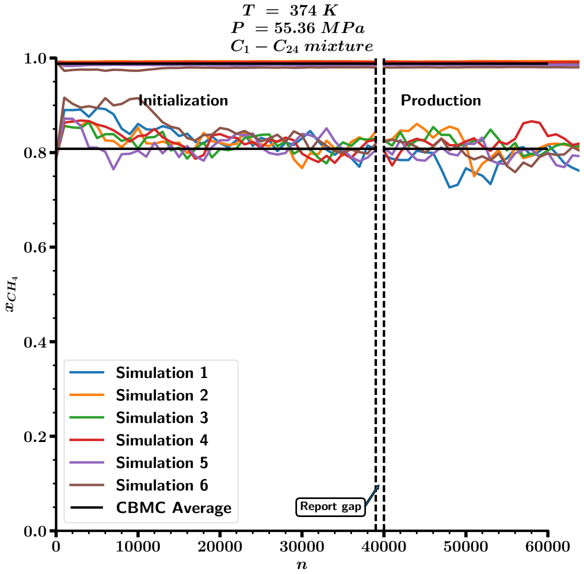

Figure A.106: Methane's mole fraction change as a function of Monte Carlo cycles at $T = 374\ K$ and at $P = 55.36\ MPa$

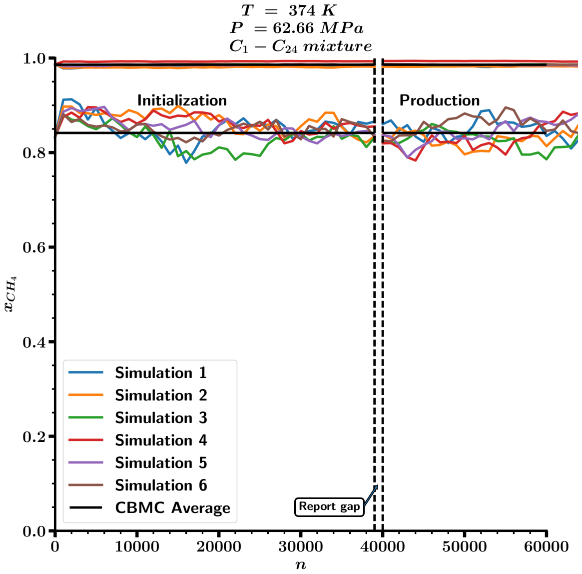

Figure A.107: Methane's mole fraction change as a function of Monte Carlo cycles at $T = 374\ K$ and at $P = 62.66\ MPa$

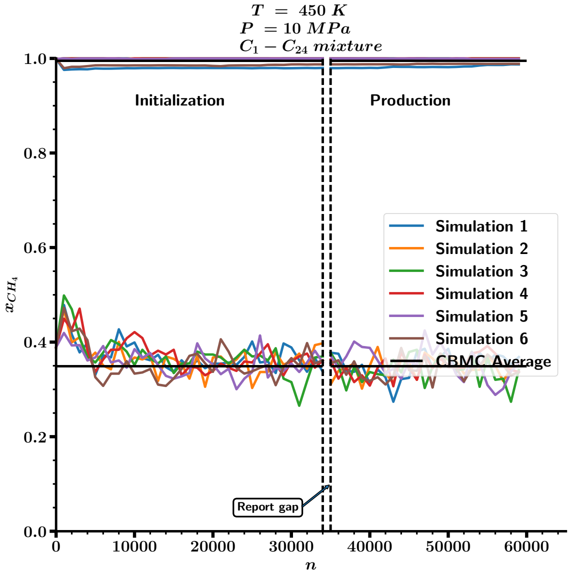

Figure A.108: Methane's mole fraction change as a function of Monte Carlo cycles at $T = 450\ K$ and at $P = 10\ MPa$

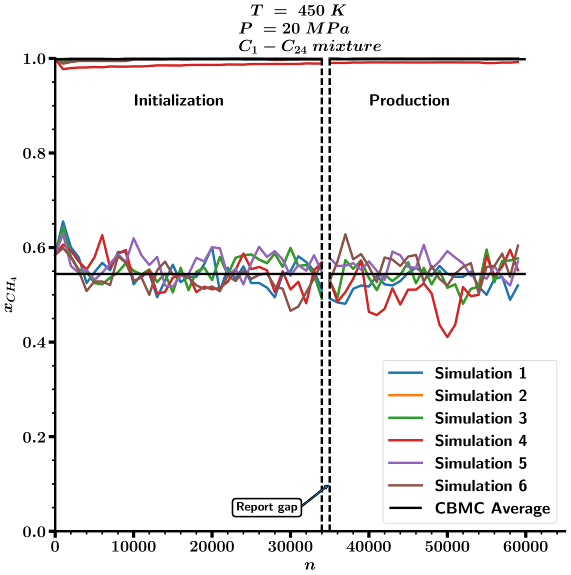

Figure A.109: Methane's mole fraction change as a function of Monte Carlo cycles at $T = 500\ K$ and at $P = 20\ MPa$

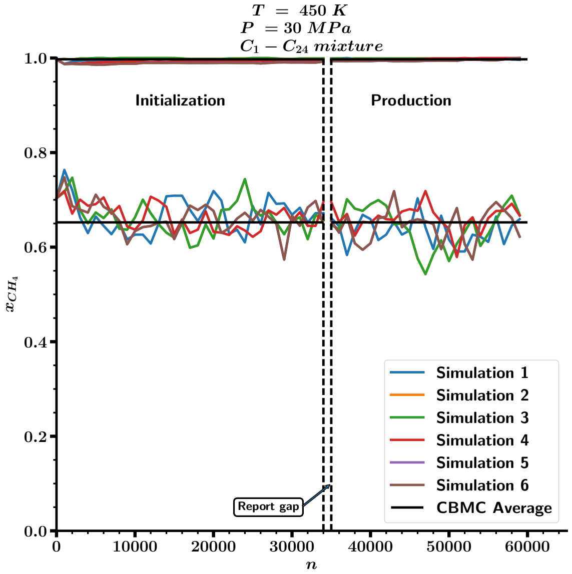

Figure A.110: Methane's mole fraction change as a function of Monte Carlo cycles at $T = 450\ K$ and at $P = 30\ MPa$

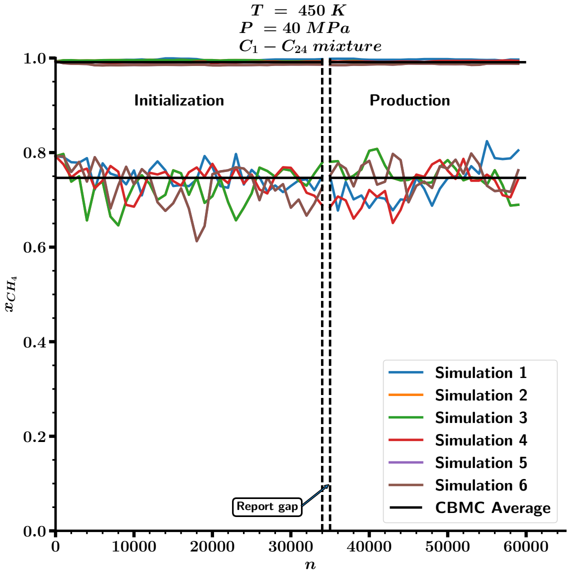

Figure A.111: Methane's mole fraction change as a function of Monte Carlo cycles at $T = 500\ K$ and at $P = 40\ MPa$

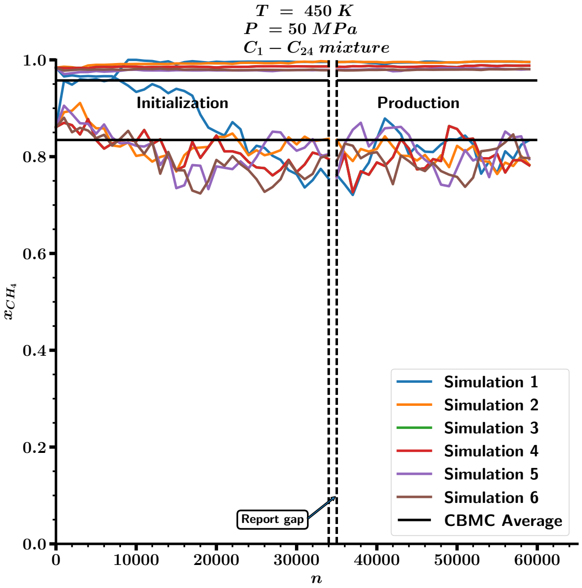

Figure A.112: Methane's mole fraction change as a function of Monte Carlo cycles at $T = 450\ K$ and at $P = 50\ MPa$

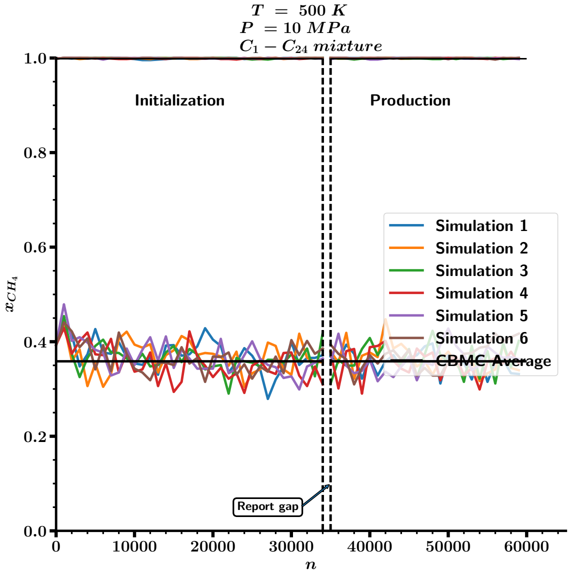

Figure A.113: Methane's mole fraction change as a function of Monte Carlo cycles at $T = 500\ K$ and at $P = 10\ MPa$

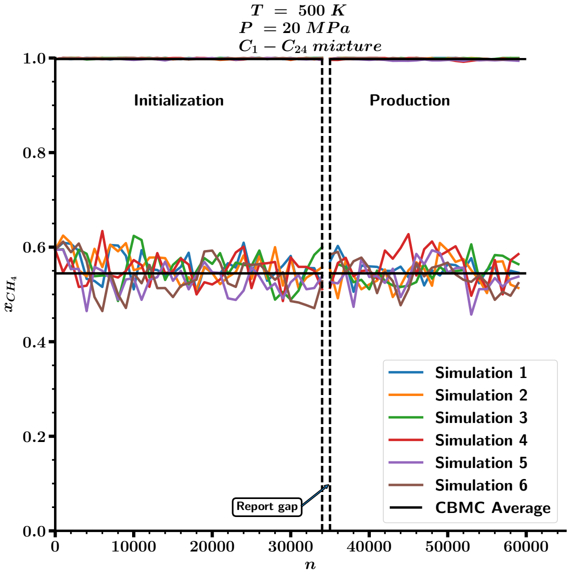

Figure A.114: Methane's mole fraction change as a function of Monte Carlo cycles at $T = 500\ K$ and at $P = 20\ MPa$

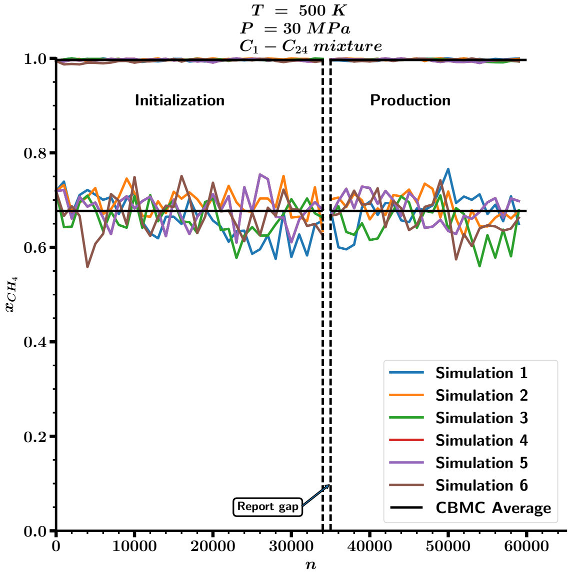

Figure A.115: Methane's mole fraction change as a function of Monte Carlo cycles at $T = 500\ K$ and at $P = 30\ MPa$

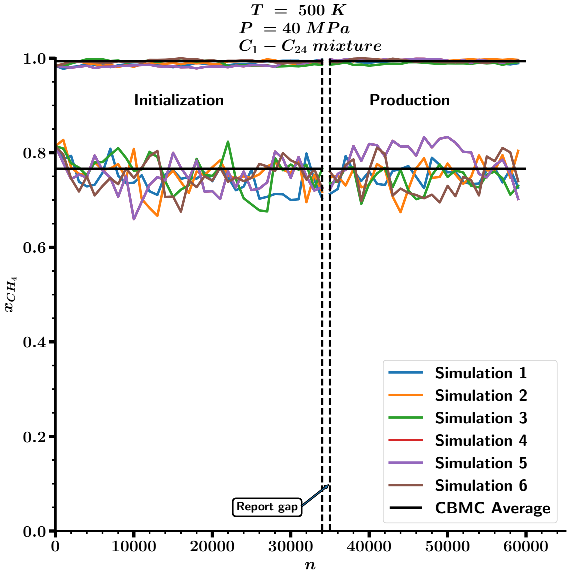

Figure A.116: Methane's mole fraction change as a function of Monte Carlo cycles at $T = 500\ K$ and at $P = 40\ MPa$

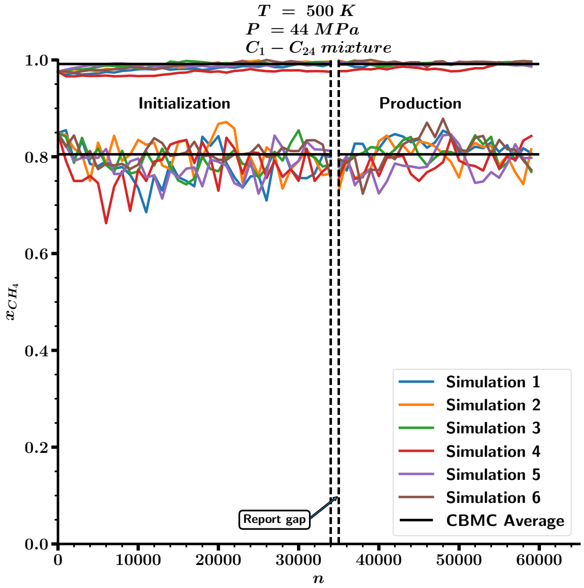

Figure A.117: Methane's mole fraction change as a function of Monte Carlo cycles at $T\ =\ 500\ K$ and at $P\ =\ 44\ MPa$

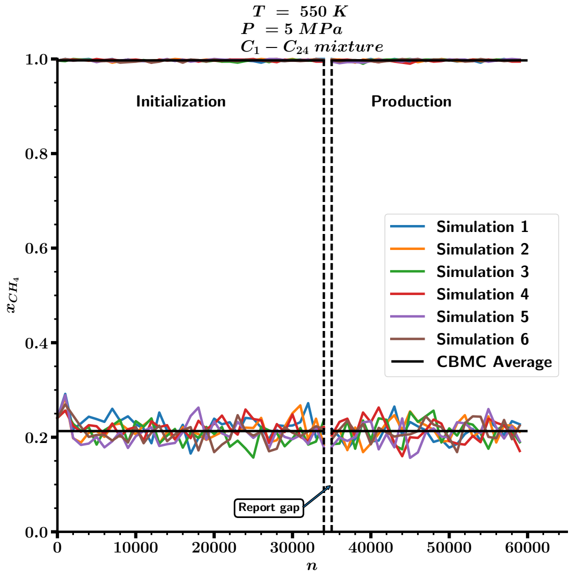

Figure A.118: Methane's mole fraction change as a function of Monte Carlo cycles at $T\ =\ 550\ K$ and at $P\ =\ 5\ MPa$

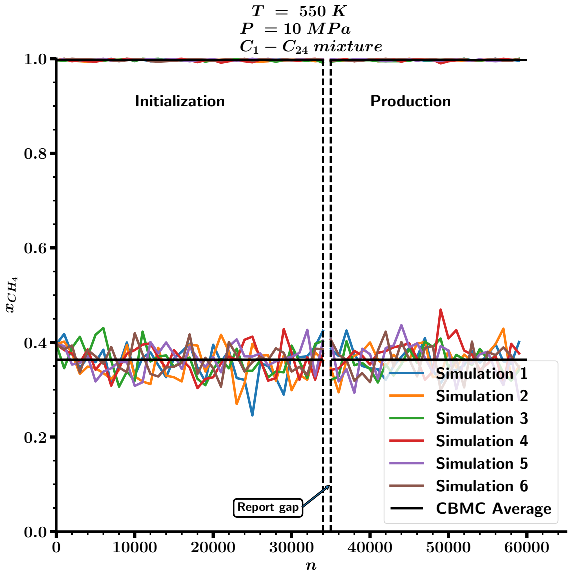

Figure A.119: Methane's mole fraction change as a function of Monte Carlo cycles at $T\ =\ 550\ K$ and at $P\ =\ 10\ MPa$

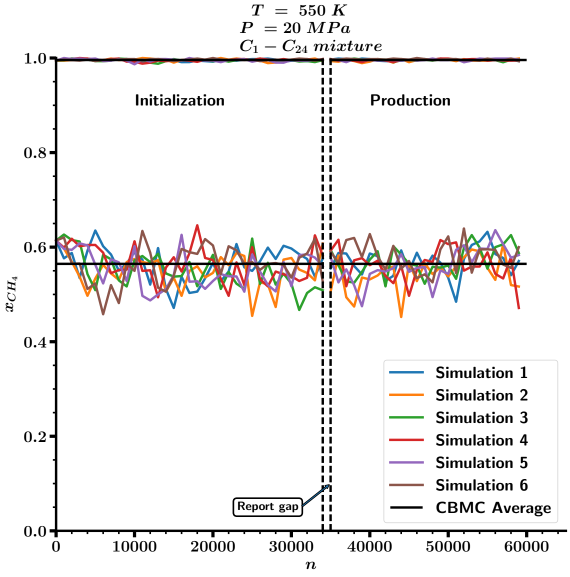

Figure A.120: Methane's mole fraction change as a function of Monte Carlo cycles at $T = 550\ K$ and at $P = 20\ MPa$

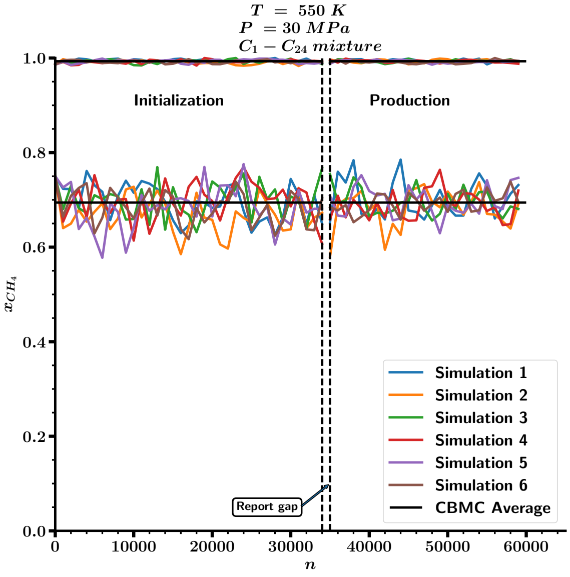

Figure A.121: Methane's mole fraction change as a function of Monte Carlo cycles at $T = 550\ K$ and at $P = 30\ MPa$

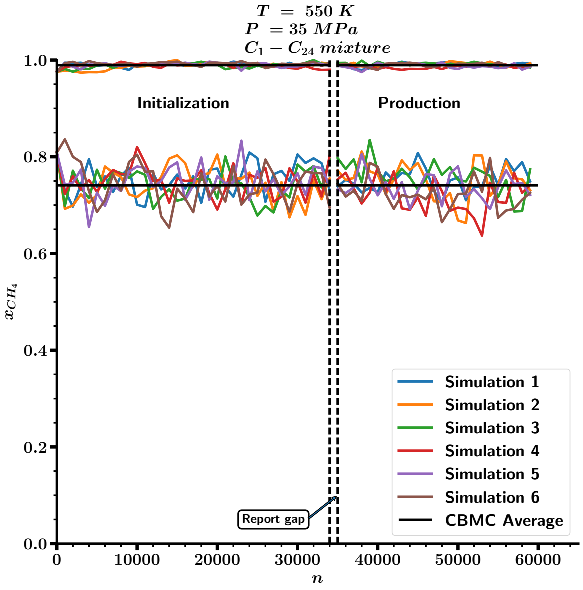

Figure A.122: Methane's mole fraction change as a function of Monte Carlo cycles at $T = 550\ K$ and at $P = 35\ MPa$

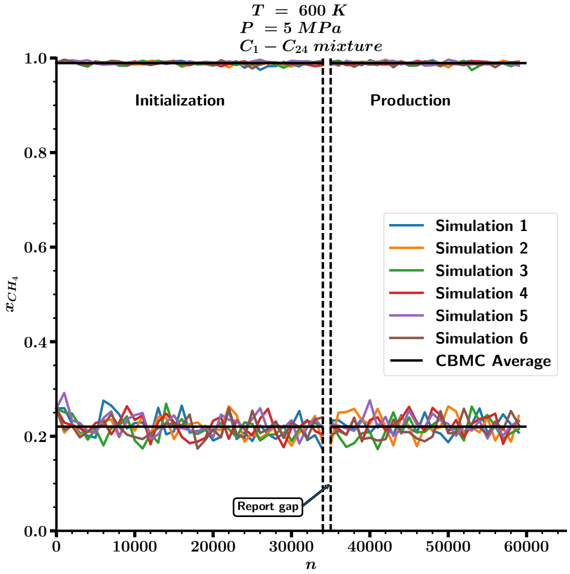

Figure A.123: Methane's mole fraction change as a function of Monte Carlo cycles at $T = 600\ K$ and at $P = 5\ MPa$

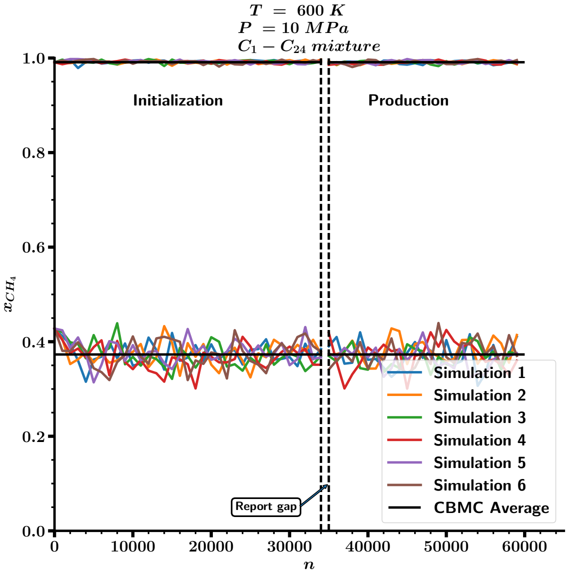

Figure A.124: Methane's mole fraction change as a function of Monte Carlo cycles at $T = 600\ K$ and at $P = 10\ MPa$

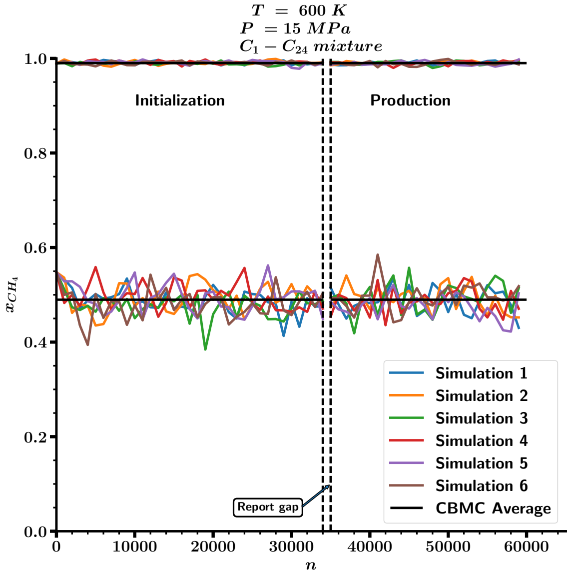

Figure A.125: Methane's mole fraction change as a function of Monte Carlo cycles at $T = 600\ K$ and at $P = 15\ MPa$

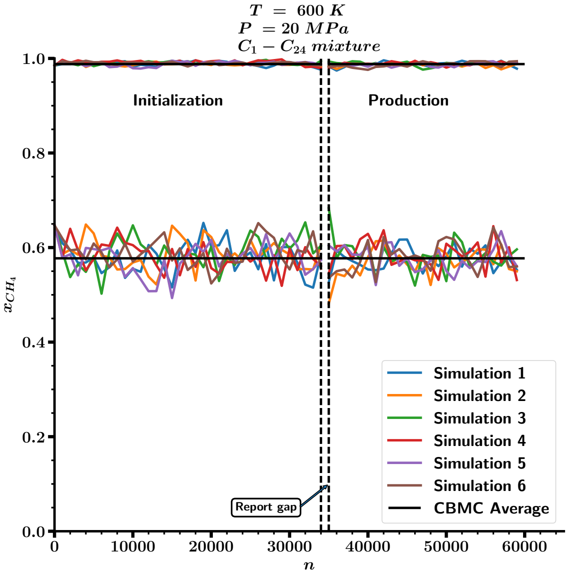

Figure A.126: Methane's mole fraction change as a function of Monte Carlo cycles at $T = 600\ K$ and at $P = 20\ MPa$

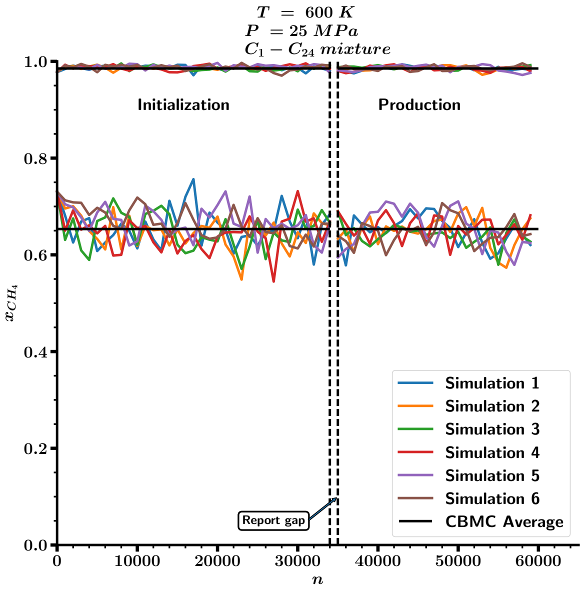

Figure A.127: Methane's mole fraction change as a function of Monte Carlo cycles at $T = 600\ K$ and at $P = 25\ MPa$

A.6. METHANE - TOLUENE BINARY MIXTURE

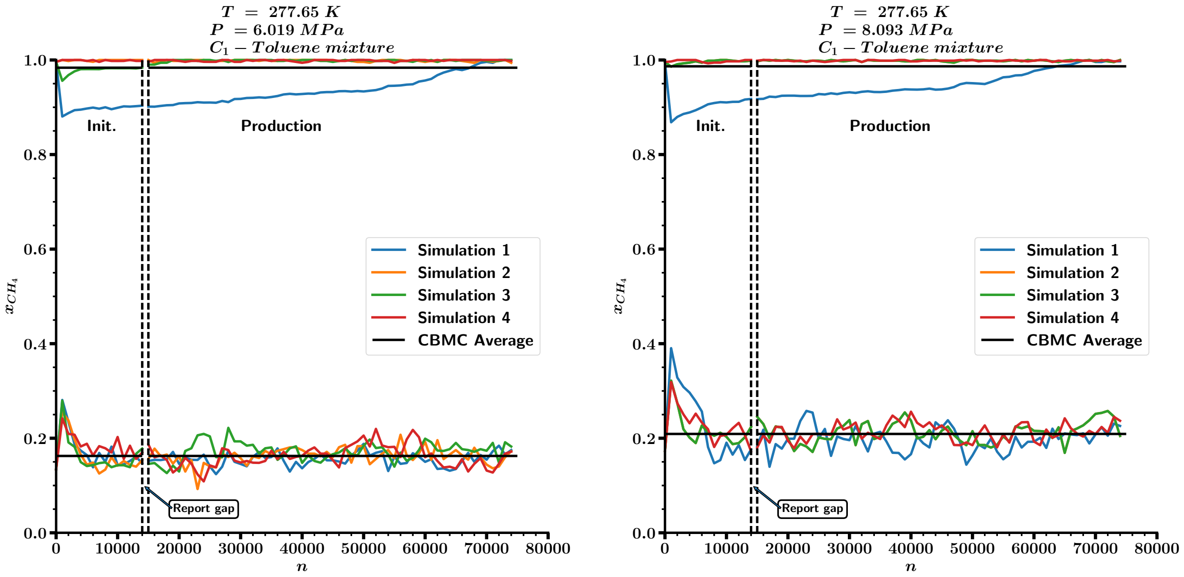

Figure A.128: Methane's mole fraction change as a function of Monte Carlo cycles at $T = 277.65\ K$ and at $P = 6.019\ MPa$

Figure A.129: Methane's mole fraction change as a function of Monte Carlo cycles at $T = 277.65\ K$ and at $P = 8.093\ MPa$

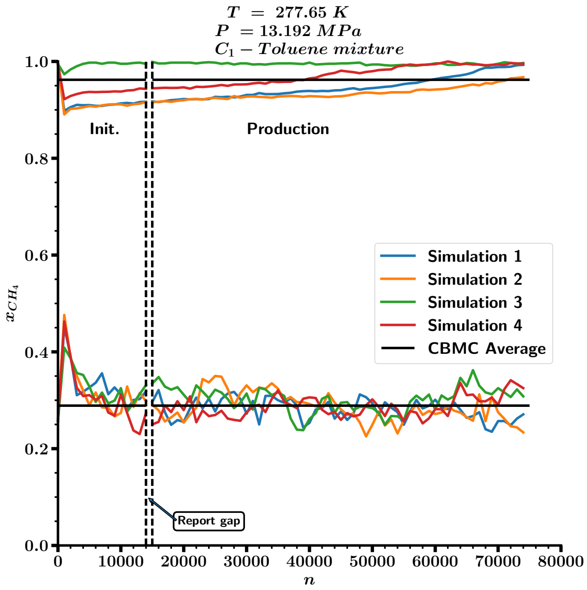

Figure A.130: Methane's mole fraction change as a function of Monte Carlo cycles at $T\ =\ 277.65\ K$ and at $P\ =\ 13.192\ MPa$

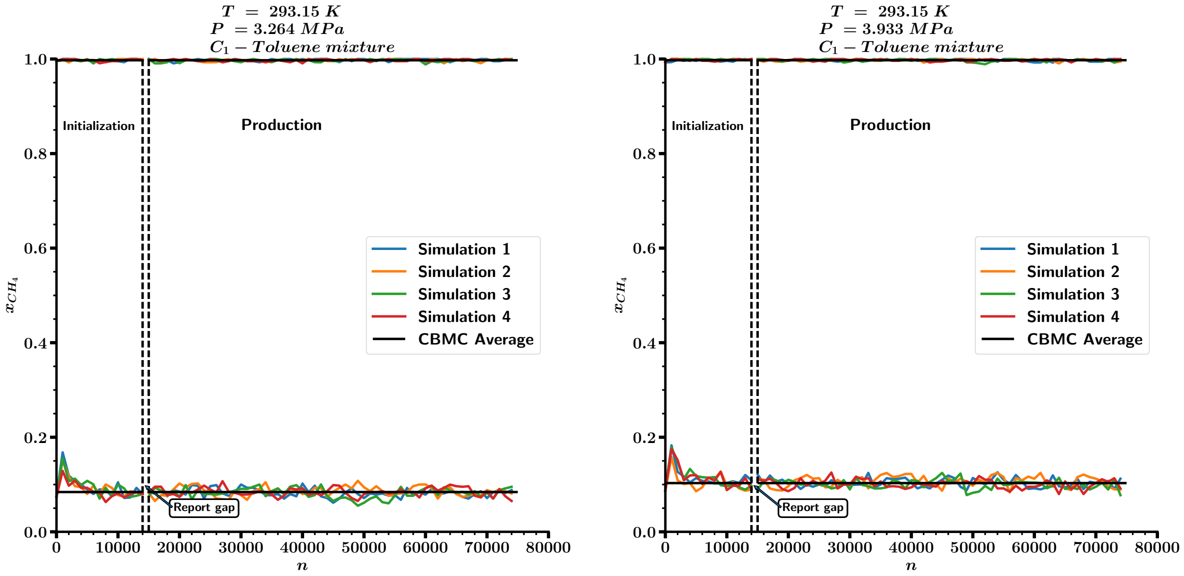

Figure A.131: Methane's mole fraction change as a function of Monte Carlo cycles at $T\ =\ 293.15\ K$ and at $P\ =\ 3.264\ MPa$

Figure A.132: Methane's mole fraction change as a function of Monte Carlo cycles at $T\ =\ 293.15\ K$ and at $P\ =\ 3.933\ MPa$

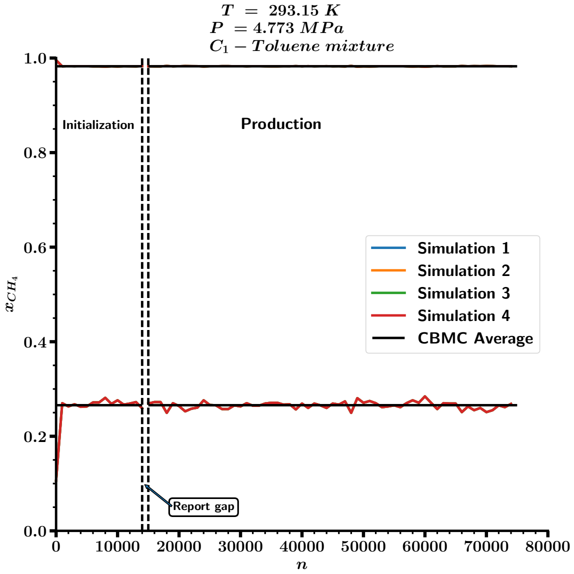

Figure A.133: Methane's mole fraction change as a function of Monte Carlo cycles at $T = 293.15\ K$ and at $P = 4.773\ MPa$

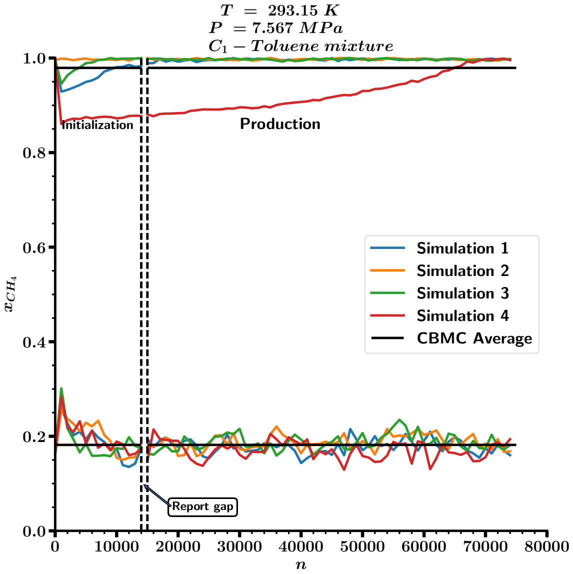

Figure A.134: Methane's mole fraction change as a function of Monte Carlo cycles at $T = 293.15\ K$ and at $P = 7.567\ MPa$

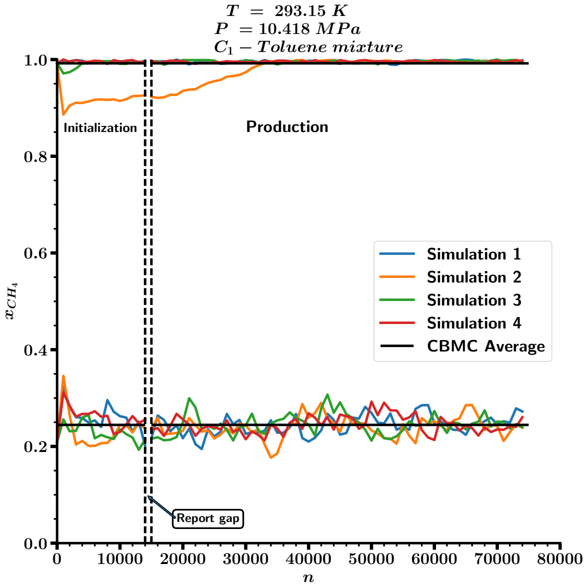

Figure A.135: Methane's mole fraction change as a function of Monte Carlo cycles at $T = 293.15\ K$ and at $P = 10.418\ MPa$

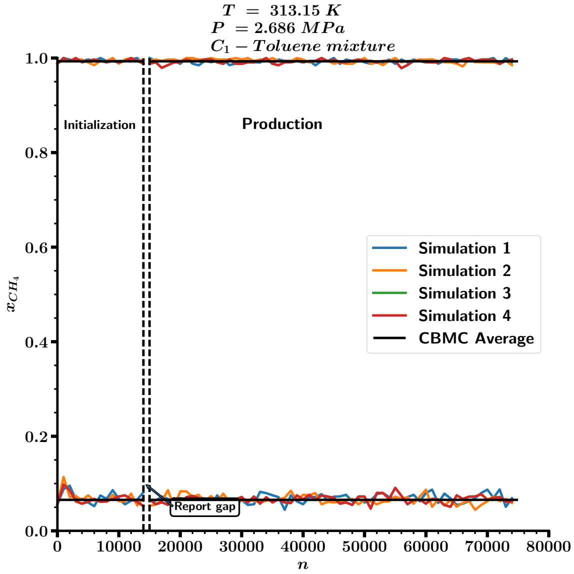

Figure A.136: Methane's mole fraction change as a function of Monte Carlo cycles at $T = 313.15\ K$ and at $P = 2.686\ MPa$

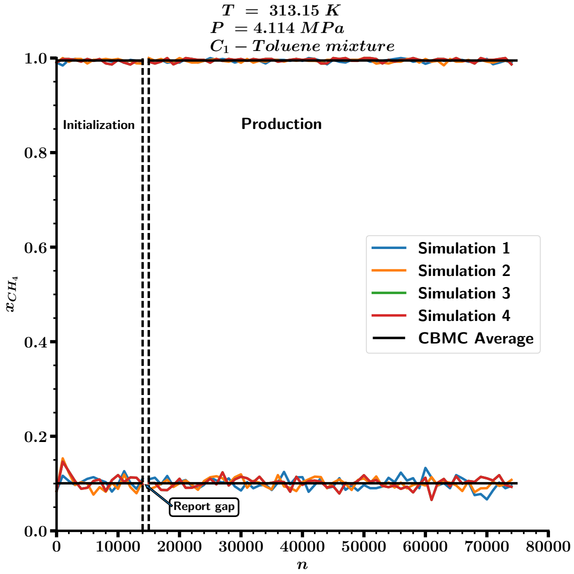

Figure A.137: Methane's mole fraction change as a function of Monte Carlo cycles at $T = 313.15\ K$ and at $P = 4.114\ MPa$

B

Appendix-B

B.1. Methane - Dodecane binary mixture

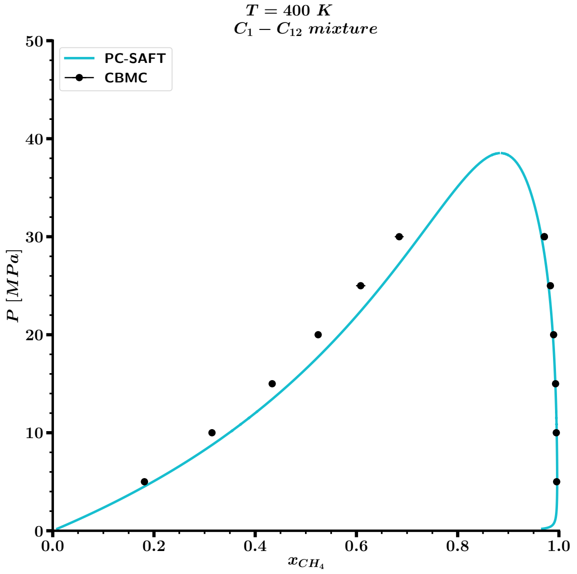

Figure B.1: Vapor-liquid coexistance curve for Methane - Dodecane system. Coexistence data predicted by PC-SAFT is shown as long cian line. Simulated Methane mole fractions for TraPPE force field with CBMC are shown as black dots.

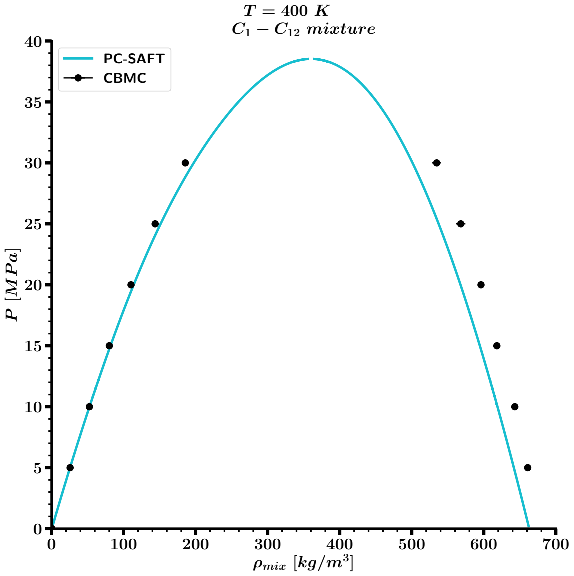

Figure B.2: Vapor-liquid coexistance curve for Methane - Dodecane system. Coexistence data predicted by PC-SAFT is shown as long cian line. Simulated Methane mole fractions for TraPPE force field with CBMC are shown as black dots.

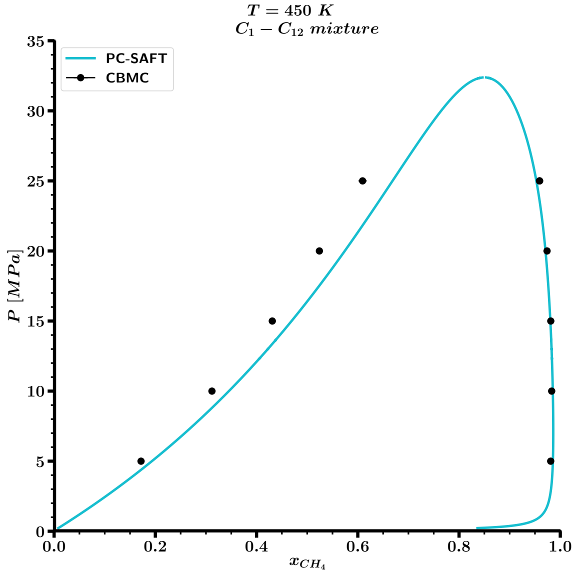

Figure B.3: Vapor-liquid coexistance curve for Methane - Dodecane system. Coexistence data predicted by PC-SAFT is shown as long cian line. Simulated Methane mole fractions for TraPPE force field with CBMC are shown as black dots.

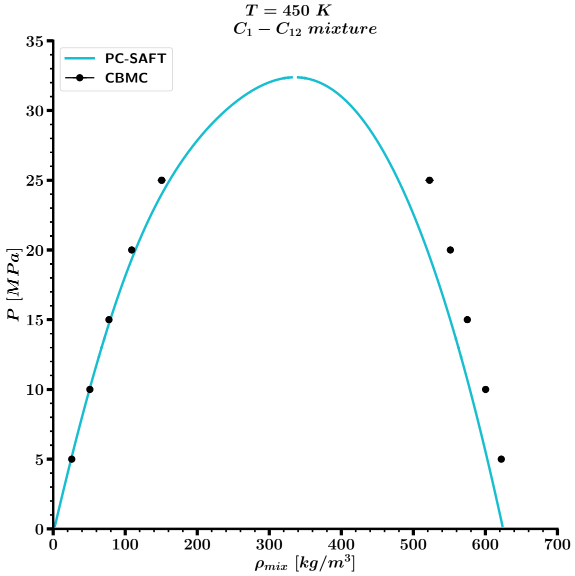

Figure B.4: Vapor-liquid coexistance curve for Methane - Dodecane system. Coexistence data predicted by PC-SAFT is shown as long cian line. Simulated Methane mole fractions for TraPPE force field with CBMC are shown as black dots.

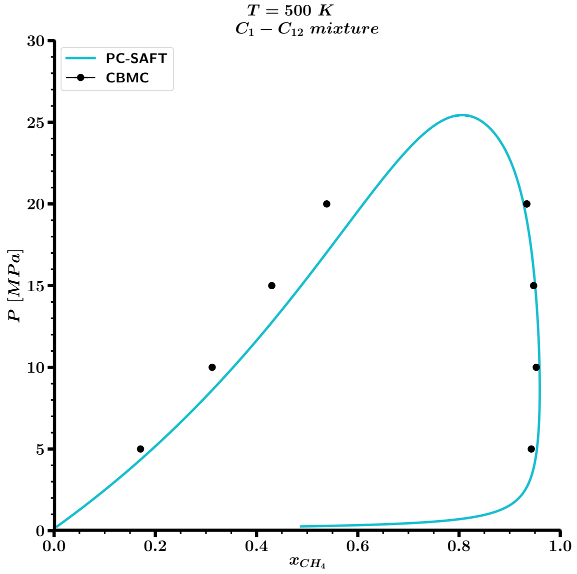

Figure B.5: Vapor-liquid coexistance curve for Methane - Dodecane system. Coexistence data predicted by PC-SAFT is shown as long cian line. Simulated Methane mole fractions for TraPPE force field with CBMC are shown as black dots.

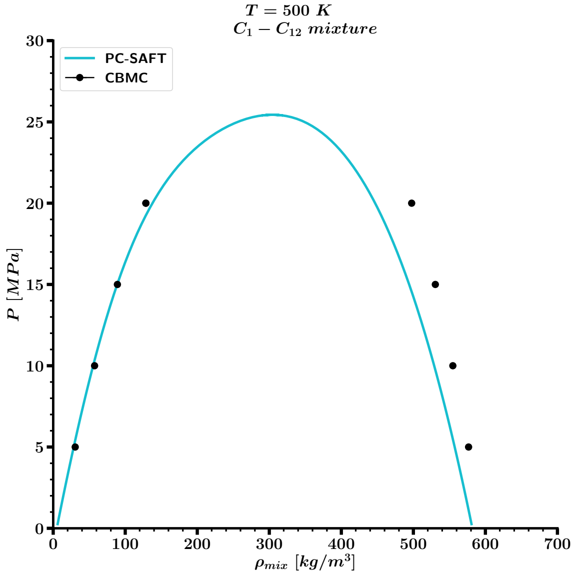

Figure B.6: Vapor-liquid coexistance curve for Methane - Dodecane system. Coexistence data predicted by PC-SAFT is shown as long cian line. Simulated Methane mole fractions for TraPPE force field with CBMC are shown as black dots.

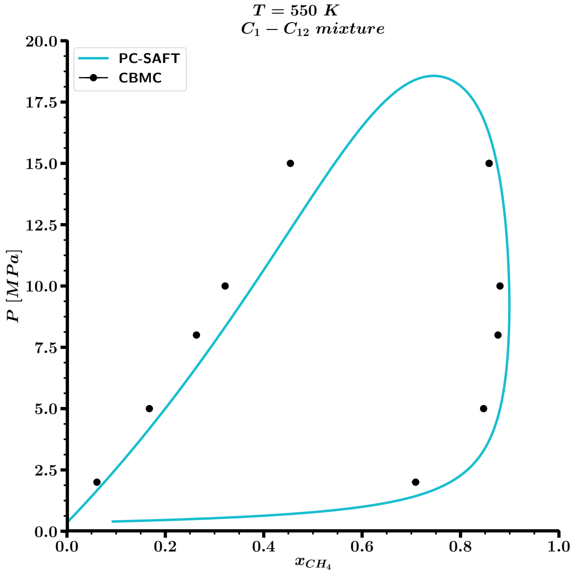

Figure B.7: Vapor-liquid coexistance curve for Methane - Dodecane system. Coexistence data predicted by PC-SAFT is shown as long cian line. Simulated Methane mole fractions for TraPPE force field with CBMC are shown as black dots.

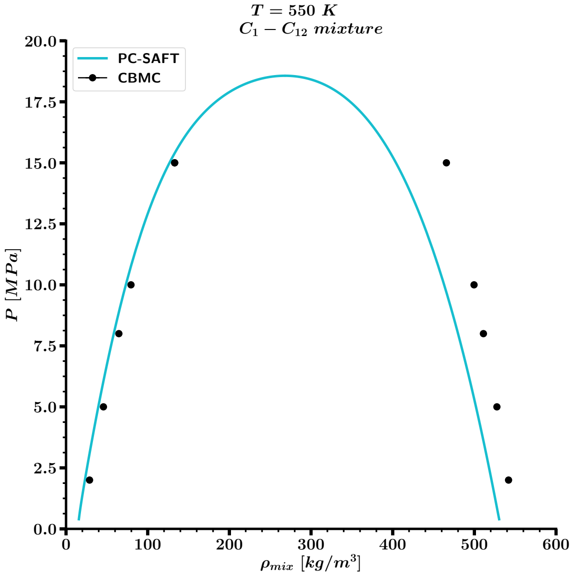

Figure B.8: Vapor-liquid coexistance curve for Methane - Dodecane system. Coexistence data predicted by PC-SAFT is shown as long cian line. Simulated Methane mole fractions for TraPPE force field with CBMC are shown as black dots.

B.2. METHANE - TETRADECANE BINARY MIXTURE

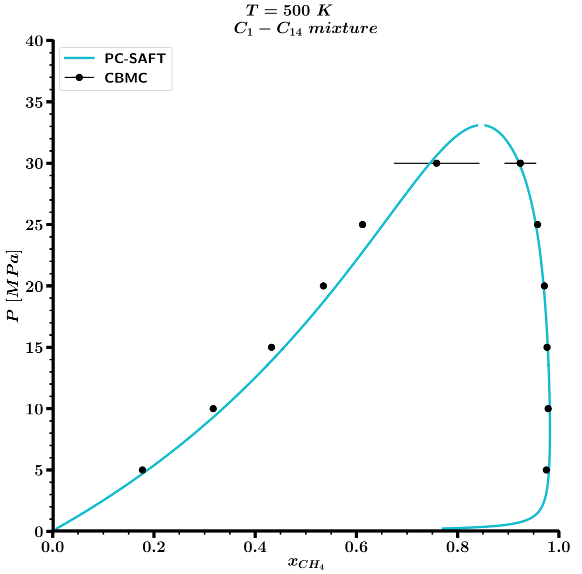

Figure B.9: Vapor-liquid coexistance curve for Methane - Tetradecane system. Coexistence data predicted by PC-SAFT is shown as long cian line. Simulated Methane mole fractions for TraPPE force field with CBMC are shown as black dots.

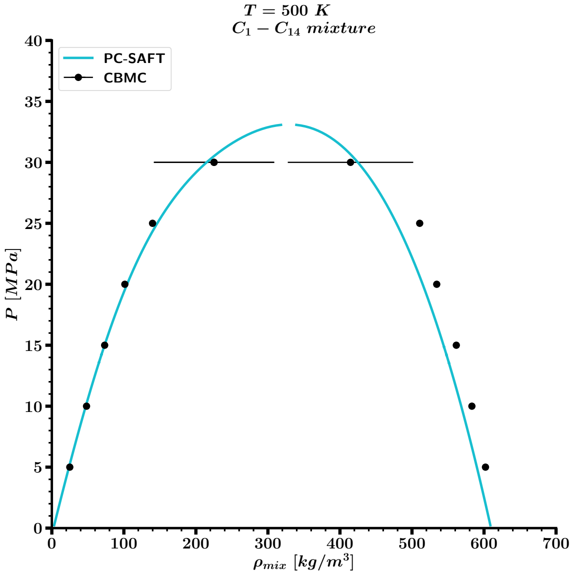

Figure B.10: Vapor-liquid coexistance curve for Methane - Tetradecane system. Coexistence data predicted by PC-SAFT is shown as long cian line. Simulated Methane mole fractions for TraPPE force field with CBMC are shown as black dots.

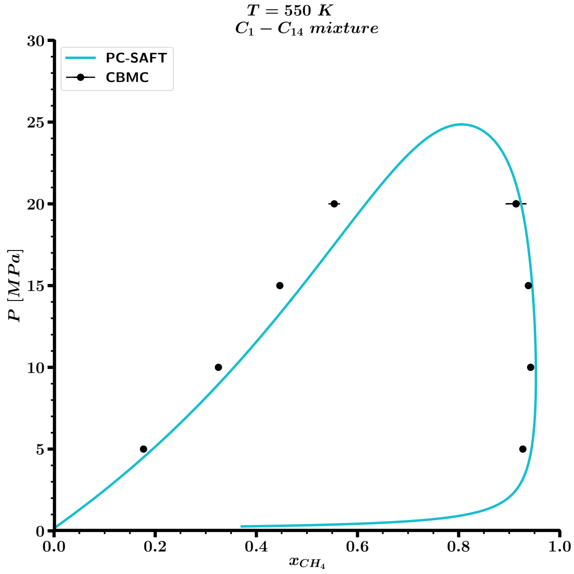

Figure B.11: Vapor-liquid coexistance curve for Methane - Tetradecane system. Coexistence data predicted by PC-SAFT is shown as long cian line. Simulated Methane mole fractions for TraPPE force field with CBMC are shown as black dots.

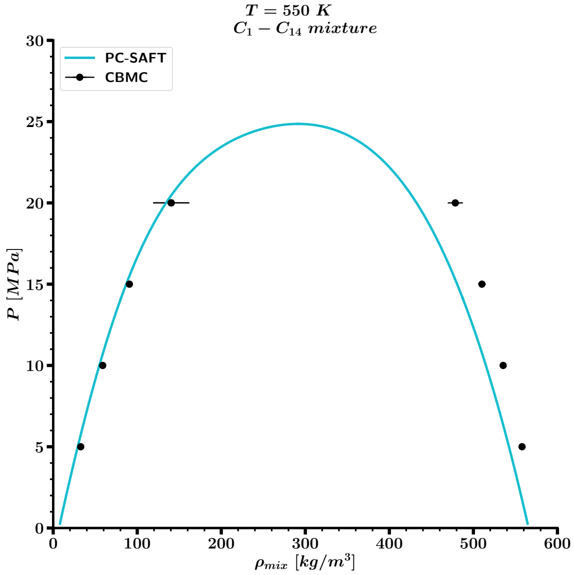

Figure B.12: Vapor-liquid coexistance curve for Methane - Tetradecane system. Coexistence data predicted by PC-SAFT is shown as long cian line. Simulated Methane mole fractions for TraPPE force field with CBMC are shown as black dots.

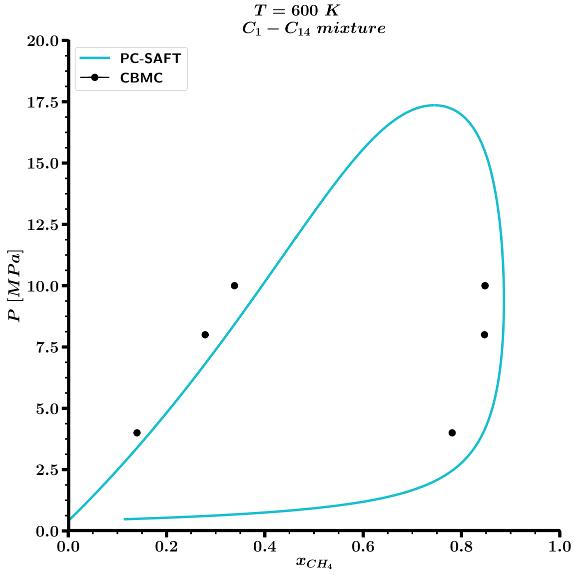

Figure B.13: Vapor-liquid coexistance curve for Methane - Tetradecane system. Coexistence data predicted by PC-SAFT is shown as long cian line. Simulated Methane mole fractions for TraPPE force field with CBMC are shown as black dots.

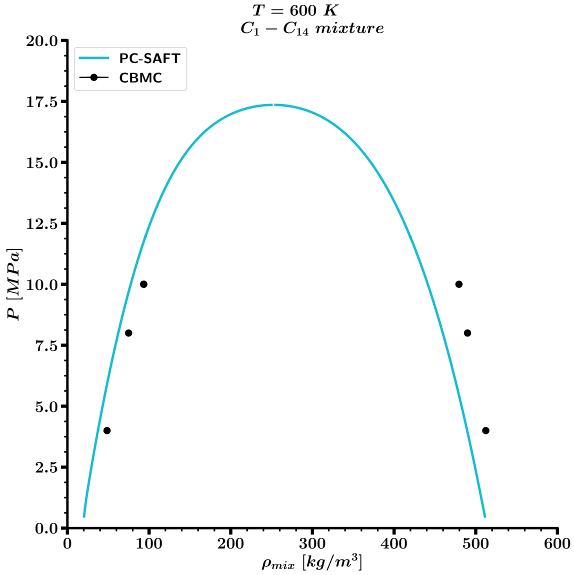

Figure B.14: Vapor-liquid coexistance curve for Methane - Tetradecane system. Coexistence data predicted by PC-SAFT is shown as long cian line. Simulated Methane mole fractions for TraPPE force field with CBMC are shown as black dots.

B.3. METHANE - HEXADECANE BINARY MIXTURE

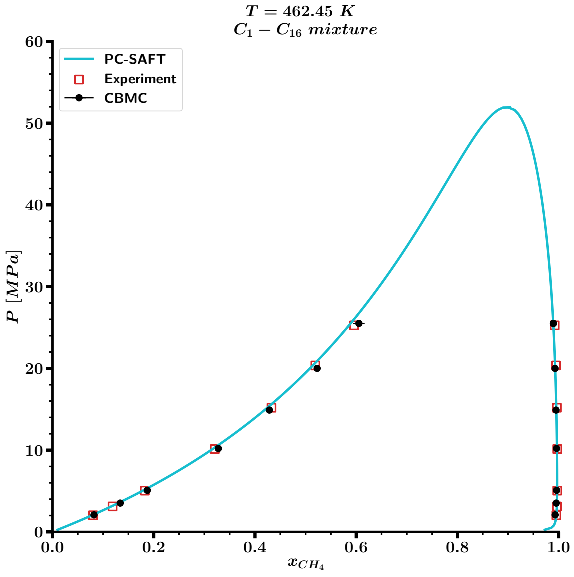

Figure B.15: Vapor-liquid coexistance curve for Methane - Hexadecane system. Experimental coexistence data are shown as red squares. Coexistence data predicted by PC-SAFT is shown as long cian line. Simulated methane mole fractions for TraPPE force field with CBMC are shown as black dots. Simulated methane mole fractions for TraPPE force field with CFCMC are shown as orange triangles.

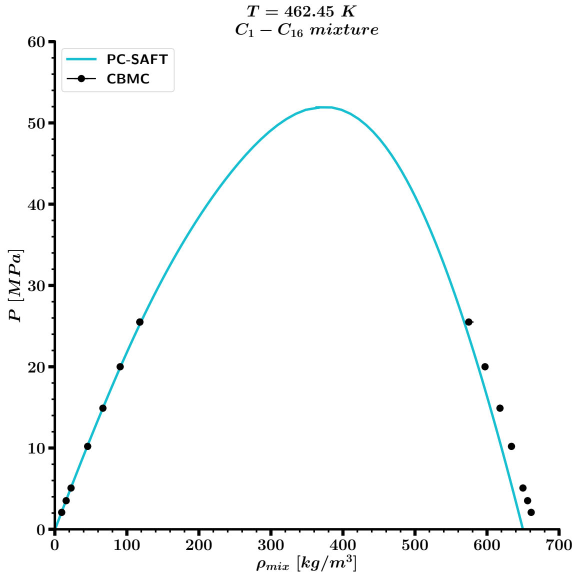

Figure B.16: Vapor-liquid coexistance curve for Methane - Hexadecane system. Coexistence data predicted by PC-SAFT is shown as long cian line. Simulated methane mole fractions for TraPPE force field with CBMC are shown as black dots. Simulated methane mole fractions for TraPPE forcefield with CFCMC are shown as orange triangles.

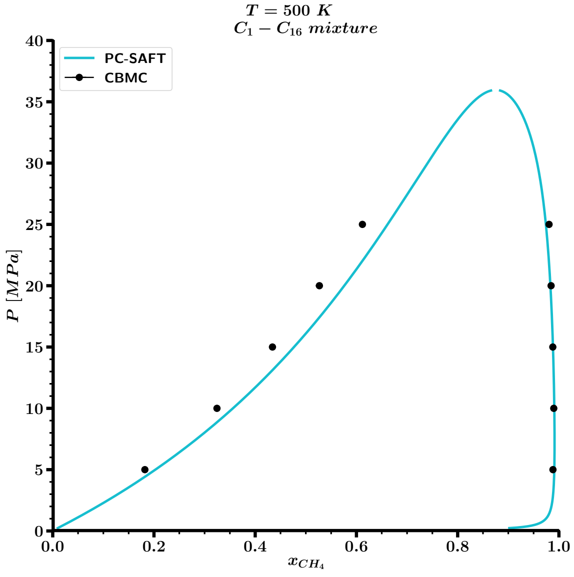

Figure B.17: Vapor-liquid coexistance curve for Methane - Hexadecane system. Experimental coexistence data are shown as red squares. Coexistence data predicted by PC-SAFT is shown as long cian line. Simulated methane mole fractions for TraPPE force field with CBMC are shown as black dots. Simulated methane mole fractions for TraPPE force field with CFCMC are shown as orange triangles.

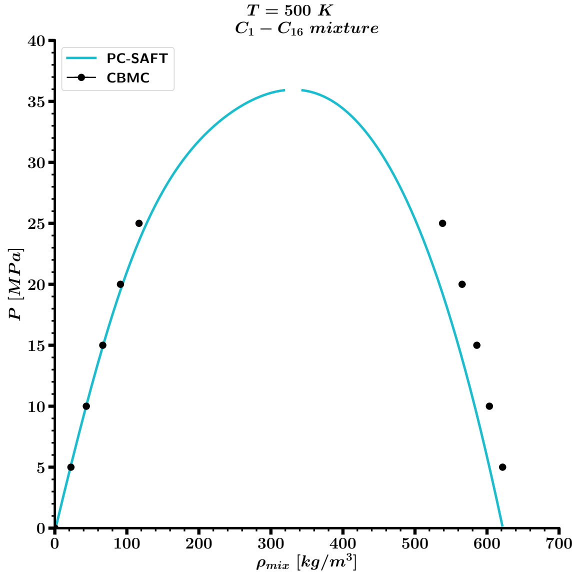

Figure B.18: Vapor-liquid coexistance curve for Methane - Hexadecane system. Coexistence data predicted by PC-SAFT is shown as long cian line. Simulated methane mole fractions for TraPPE force field with CBMC are shown as black dots. Simulated methane mole fractions for TraPPE forcefield with CFCMC are shown as orange triangles.

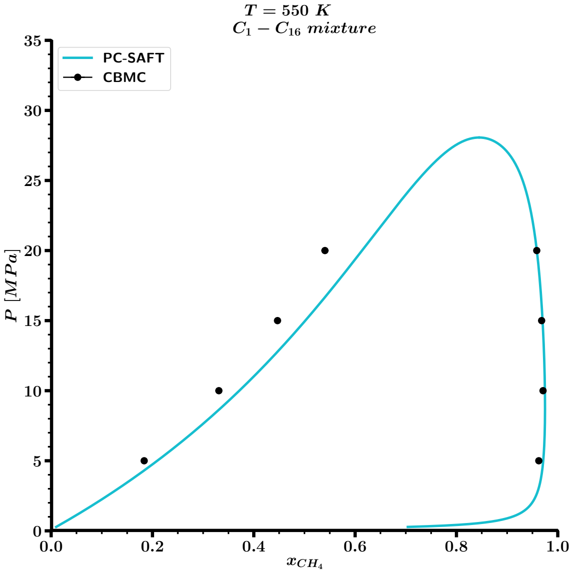

Figure B.19: Vapor-liquid coexistance curve for Methane - Hexadecane system. Experimental coexistence data are shown as red squares. Coexistence data predicted by PC-SAFT is shown as long cian line. Simulated methane mole fractions for TraPPE force field with CBMC are shown as black dots. Simulated methane mole fractions for TraPPE force field with CFCMC are shown as orange triangles.

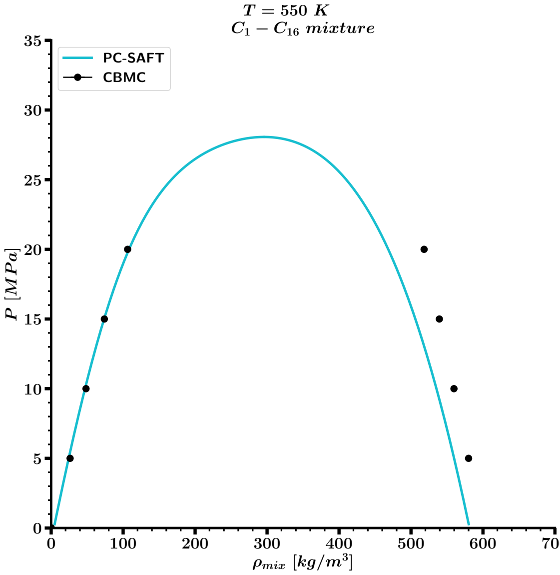

Figure B.20: Vapor-liquid coexistance curve for Methane - Hexadecane system. Coexistence data predicted by PC-SAFT is shown as long cian line. Simulated methane mole fractions for TraPPE force field with CBMC are shown as black dots. Simulated methane mole fractions for TraPPE forcefield with CFCMC are shown as orange triangles.

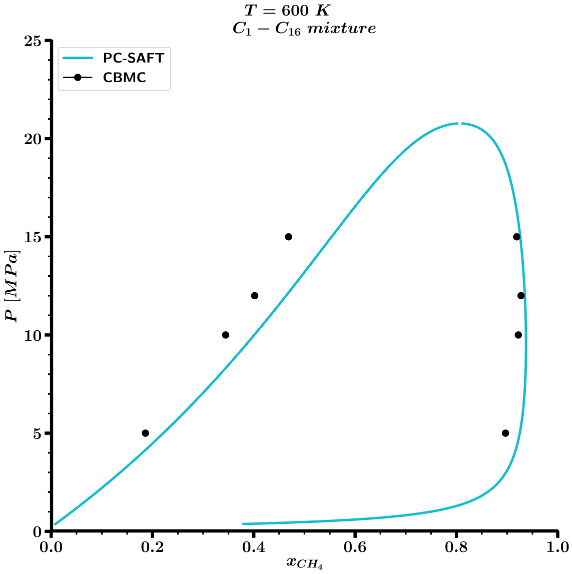

Figure B.21: Vapor-liquid coexistance curve for Methane - Hexadecane system. Experimental coexistence data are shown as red squares. Coexistence data predicted by PC-SAFT is shown as long cian line. Simulated methane mole fractions for TraPPE force field with CBMC are shown as black dots. Simulated methane mole fractions for TraPPE force field with CFCMC are shown as orange triangles.

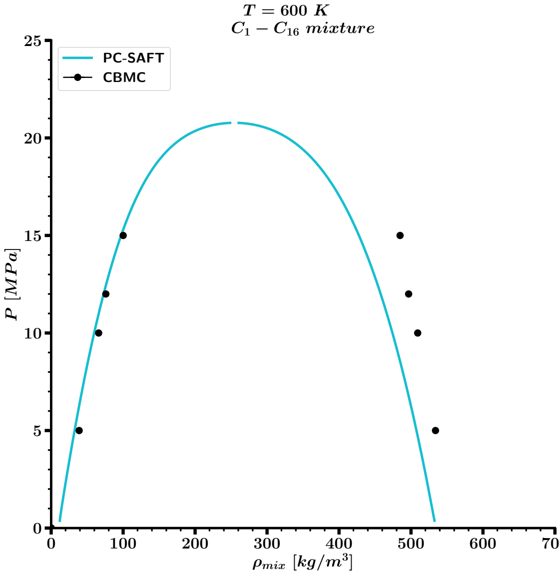

Figure B.22: Vapor-liquid coexistance curve for Methane - Hexadecane system. Coexistence data predicted by PC-SAFT is shown as long cian line. Simulated methane mole fractions for TraPPE force field with CBMC are shown as black dots. Simulated methane mole fractions for TraPPE forcefield with CFCMC are shown as orange triangles.

B.4. Methane - Icosane binary mixture

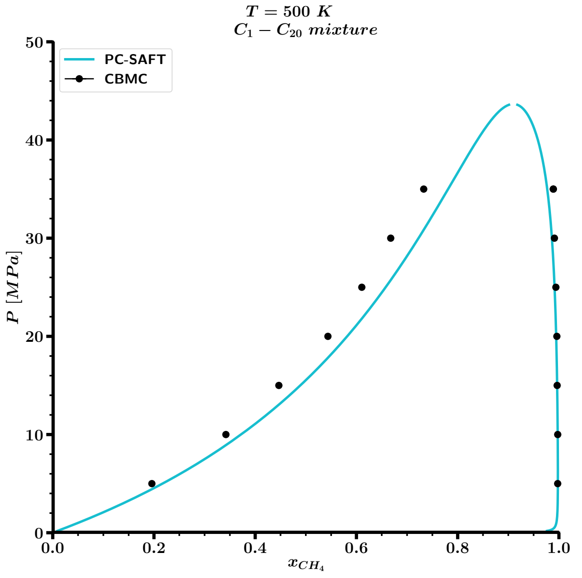

Figure B.23: Vapor-liquid coexistance curve for Methane - Icosane system. Coexistence data predicted by PC-SAFT is shown as long cian line. Simulated Methane mole fractions for TraPPE force field with CBMC are shown as black dots.

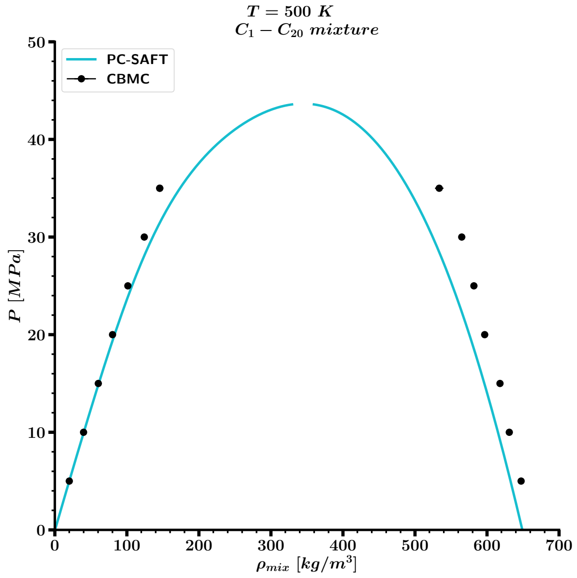

Figure B.24: Vapor-liquid coexistance curve for Methane - Icosane system. Coexistence data predicted by PC-SAFT is shown as long cian line. Simulated Methane mole fractions for TraPPE force field with CBMC are shown as black dots.

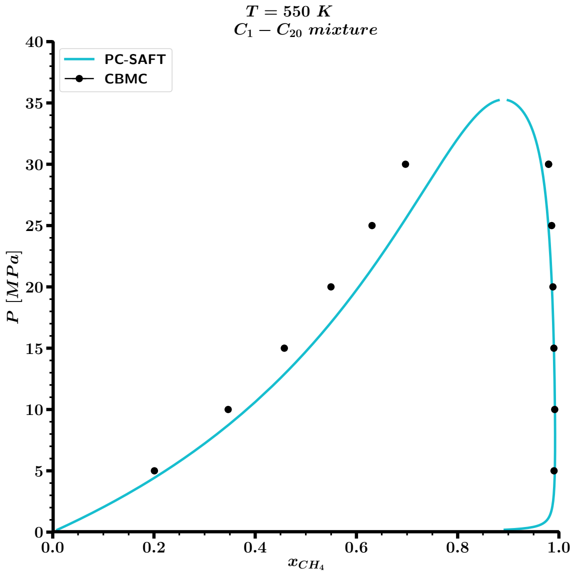

Figure B.25: Vapor-liquid coexistance curve for Methane - Icosane system. Coexistence data predicted by PC-SAFT is shown as long cian line. Simulated Methane mole fractions for TraPPE force field with CBMC are shown as black dots.

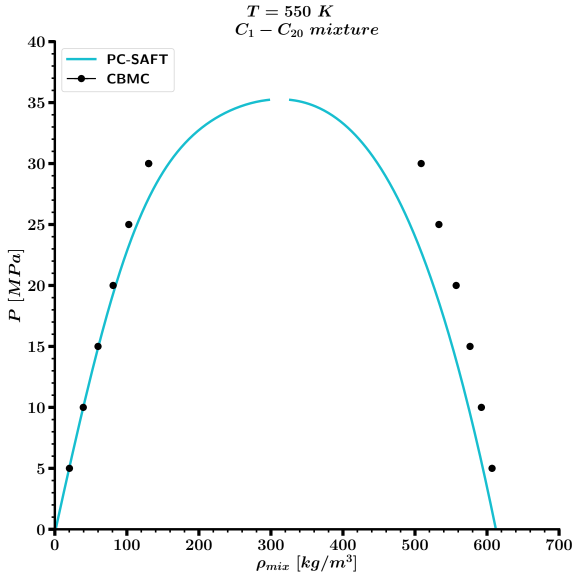

Figure B.26: Vapor-liquid coexistance curve for Methane - Icosane system. Coexistence data predicted by PC-SAFT is shown as long cian line. Simulated Methane mole fractions for TraPPE force field with CBMC are shown as black dots.

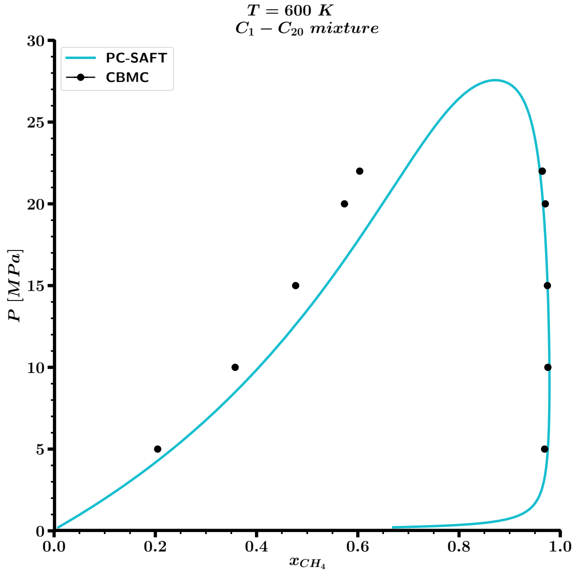

Figure B.27: Vapor-liquid coexistance curve for Methane - Icosane system. Coexistence data predicted by PC-SAFT is shown as long cian line. Simulated Methane mole fractions for TraPPE force field with CBMC are shown as black dots.

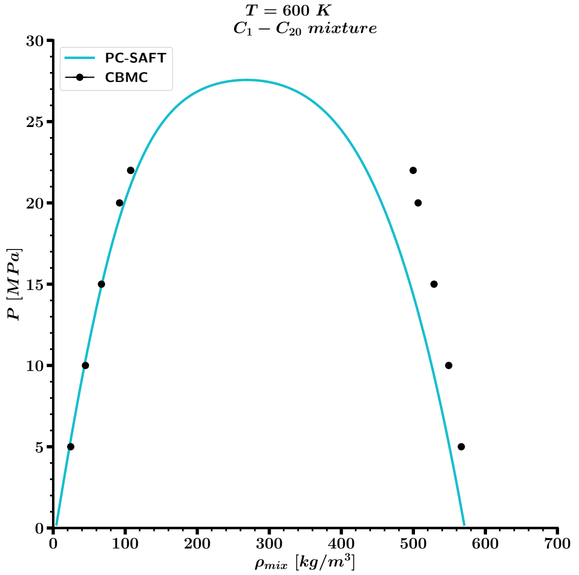

Figure B.28: Vapor-liquid coexistance curve for Methane - Icosane system. Coexistence data predicted by PC-SAFT is shown as long cian line. Simulated Methane mole fractions for TraPPE force field with CBMC are shown as black dots.

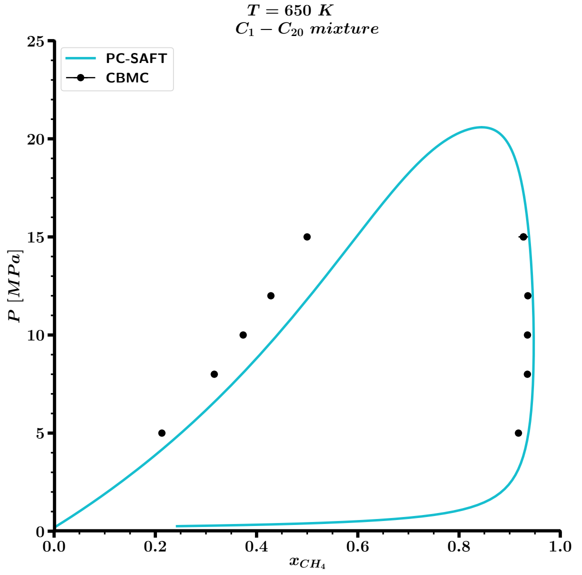

Figure B.29: Vapor-liquid coexistance curve for Methane - Icosane system. Coexistence data predicted by PC-SAFT is shown as long cian line. Simulated Methane mole fractions for TraPPE force field with CBMC are shown as black dots.

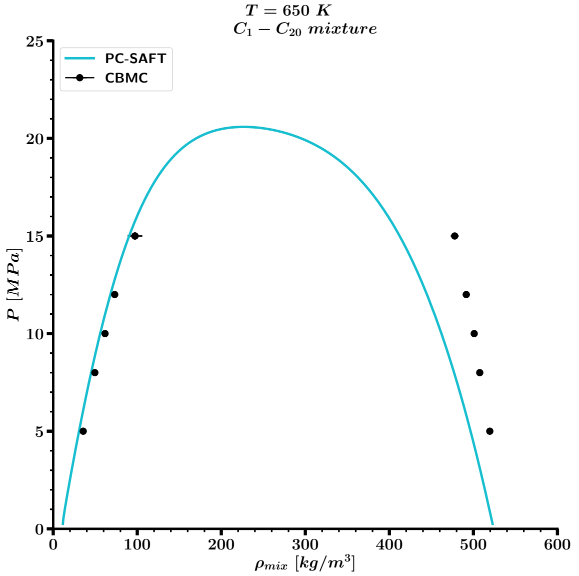

Figure B.30: Vapor-liquid coexistance curve for Methane - Icosane system. Coexistence data predicted by PC-SAFT is shown as long cian line. Simulated Methane mole fractions for TraPPE force field with CBMC are shown as black dots.

B.5. METHANE - TETRACOSANE BINARY MIXTURE

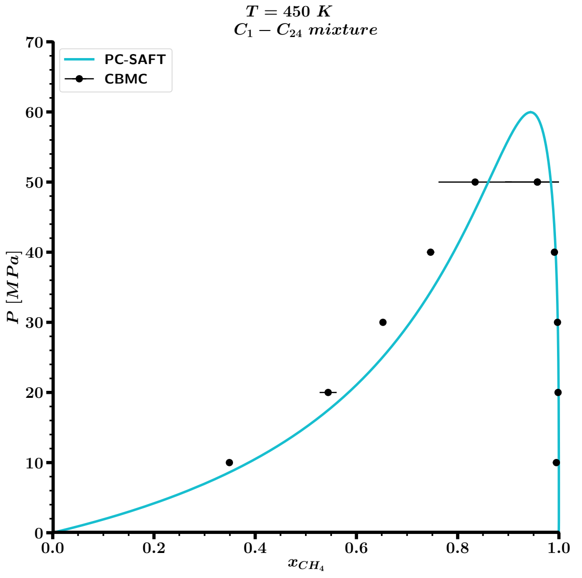

Figure B.31: Vapor-liquid coexistance curve for Methane - Tetracosane system. Coexistence data predicted by PC-SAFT is shown as long cian line. Simulated Methane mole fractions for TraPPE force field with CBMC are shown as black dots.

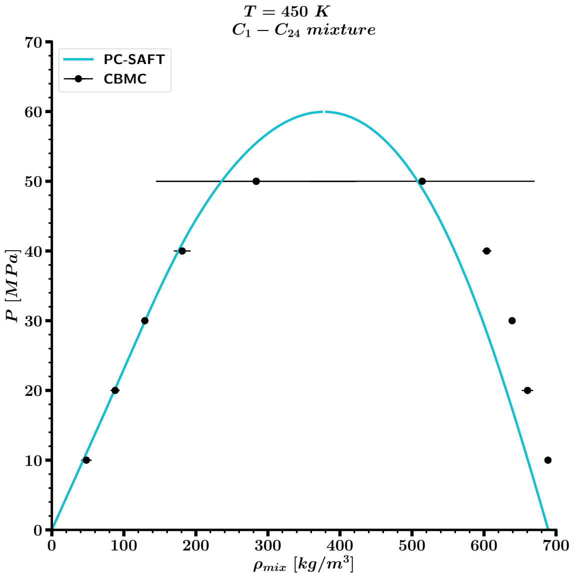

Figure B.32: Vapor-liquid coexistance curve for Methane - Tetracosane system. Coexistence data predicted by PC-SAFT is shown as long cian line. Simulated Methane mole fractions for TraPPE force field with CBMC are shown as black dots.

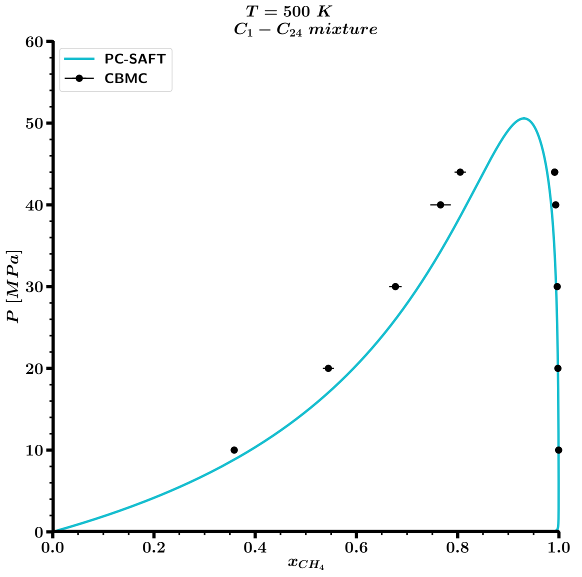

Figure B.33: Vapor-liquid coexistance curve for Methane - Tetracosane system. Coexistence data predicted by PC-SAFT is shown as long cian line. Simulated Methane mole fractions for TraPPE force field with CBMC are shown as black dots.

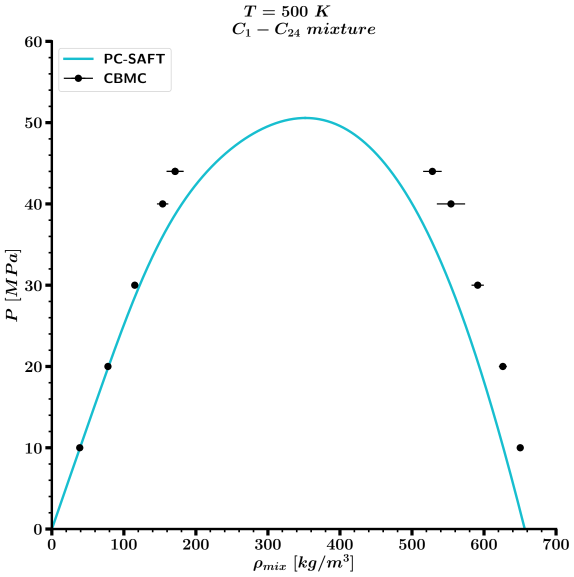

Figure B.34: Vapor-liquid coexistance curve for Methane - Tetracosane system. Coexistence data predicted by PC-SAFT is shown as long cian line. Simulated Methane mole fractions for TraPPE force field with CBMC are shown as black dots.

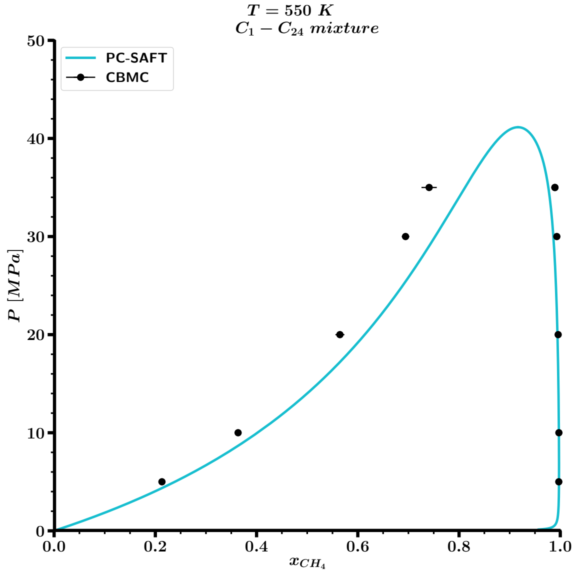

Figure B.35: Vapor-liquid coexistance curve for Methane - Tetracosane system. Coexistence data predicted by PC-SAFT is shown as long cian line. Simulated Methane mole fractions for TraPPE force field with CBMC are shown as black dots.

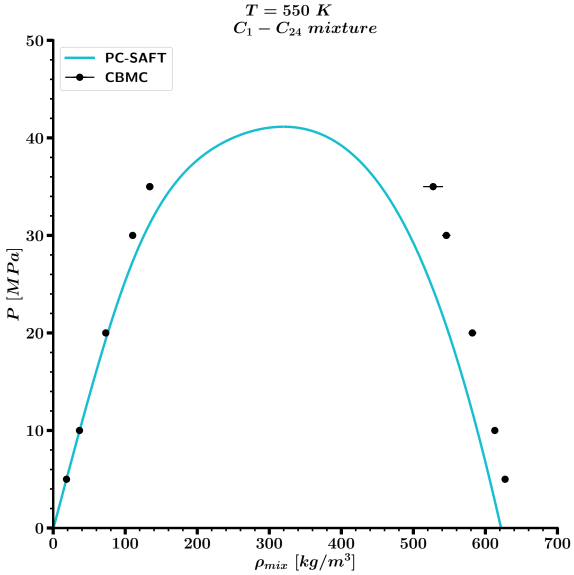

Figure B.36: Vapor-liquid coexistance curve for Methane - Tetracosane system. Coexistence data predicted by PC-SAFT is shown as long cian line. Simulated Methane mole fractions for TraPPE force field with CBMC are shown as black dots.

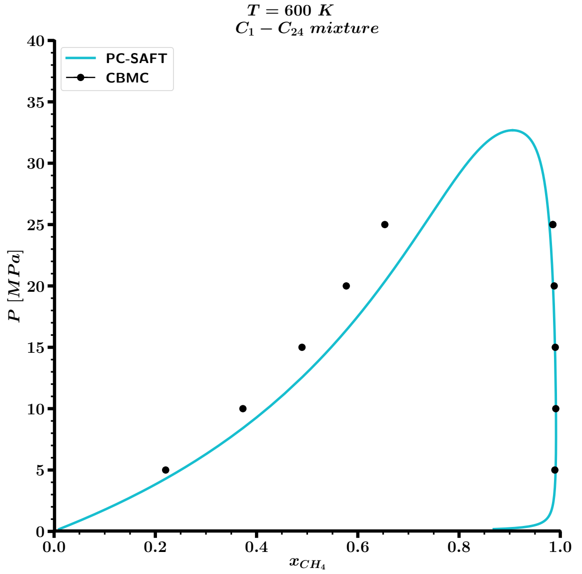

Figure B.37: Vapor-liquid coexistance curve for Methane - Tetracosane system. Coexistence data predicted by PC-SAFT is shown as long cian line. Simulated Methane mole fractions for TraPPE force field with CBMC are shown as black dots.

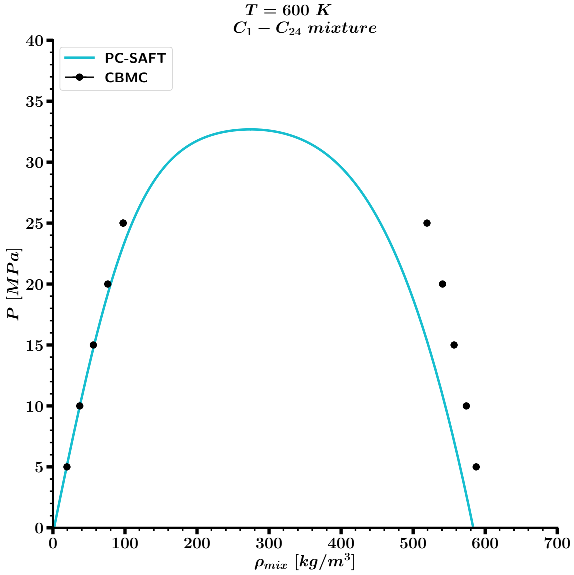

Figure B.38: Vapor-liquid coexistance curve for Methane - Tetracosane system. Coexistence data predicted by PC-SAFT is shown as long cian line. Simulated Methane mole fractions for TraPPE force field with CBMC are shown as black dots.

B.6. METHANE - TOLUENE BINARY MIXTURE

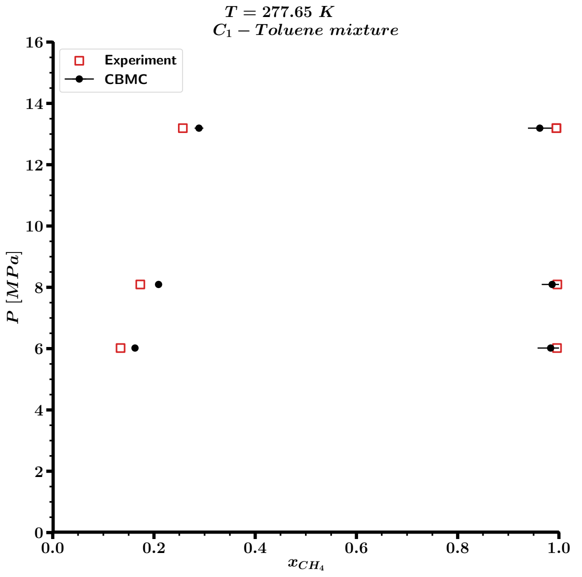

Figure B.39: Vapor-liquid coexistance curve for Methane - Toluene system. Experimental coexistence data are shown as red squares. Simulated Methane mole fractions for TraPPE force field with CBMC are shown as black dots.

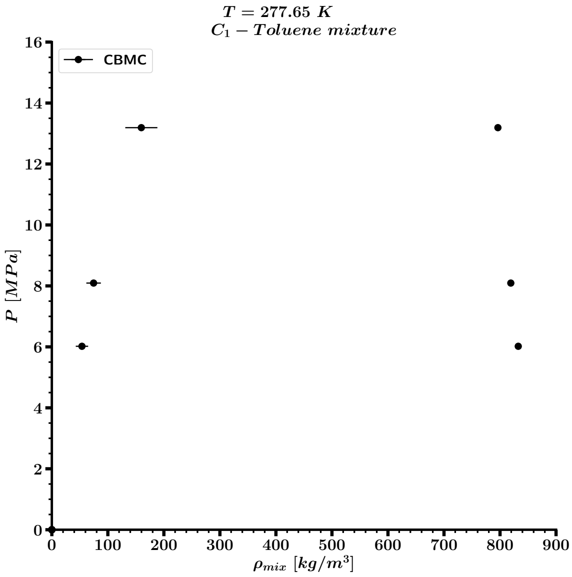

Figure B.40: Vapor-liquid coexistance curve for Methane - Toluene system. Simulated Methane mole fractions for TraPPE force field with CBMC are shown as black dots.

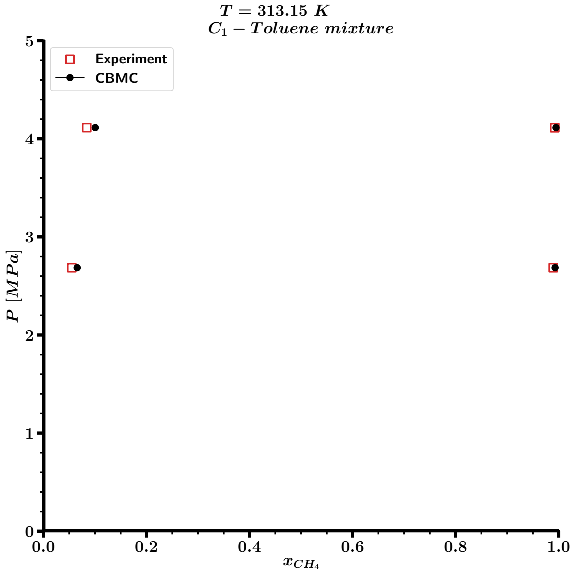

Figure B.41: Vapor-liquid coexistance curve for Methane - Toluene system. Experimental coexistence data are shown as red squares. Simulated Methane mole fractions for TraPPE force field with CBMC are shown as black dots.

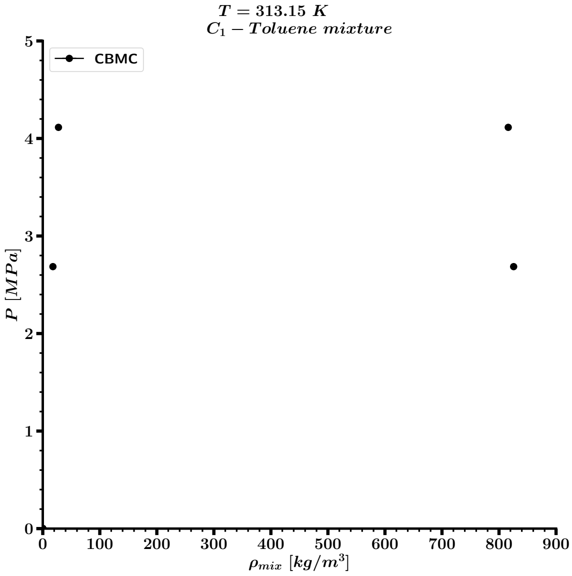

Figure B.42: Vapor-liquid coexistance curve for Methane - Toluene system. Simulated Methane mole fractions for TraPPE force field with CBMC are shown as black dots.

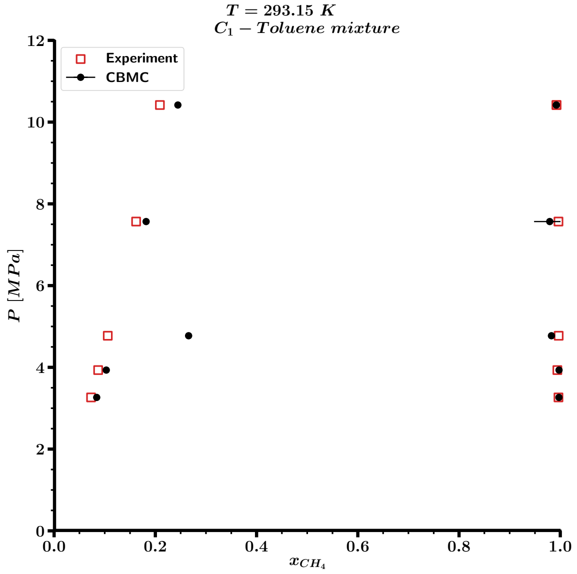

Figure B.43: Vapor-liquid coexistance curve for Methane - Toluene system. Experimental coexistence data are shown as red squares. Simulated Methane mole fractions for TraPPE force field with CBMC are shown as black dots.

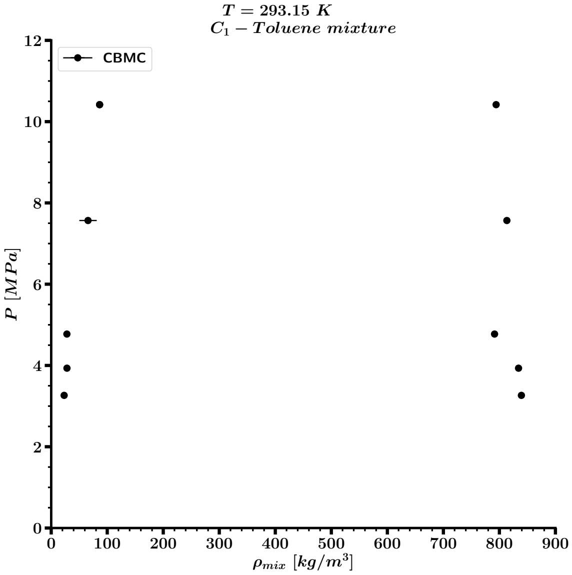

Figure B.44: Vapor-liquid coexistance curve for Methane - Toluene system. Simulated Methane mole fractions for TraPPE force field with CBMC are shown as black dots.

C

APPENDIX-C

```
SimulationType                MonteCarlo
NumberOfCycles                20000
NumberOfInitializationCycles  10000
NumberOfEquilibrationCycles   20000
PrintEvery                    1000
RestartFile                   yes
ContinueAfterCrash            no
WriteBinaryRestartFileEvery   1000
Forcefield                    local
CutOffVDW                     14
#BOX parameters
Box 0 #LIQUID
BoxLengths 48 48 48
BoxAngles 90 90 90
#predifined Temperature
ExternalTemperature 600
ExternalPressure 22000000
Movies           yes
WriteMoviesEvery 1000

Box 1 #GAS
BoxLengths 70 70 70
BoxAngles 90 90 90
ExternalTemperature 600
ExternalPressure 22000000
Movies           yes
WriteMoviesEvery 1000

VolumeChangeProbability 0.1

Component 0 MoleculeName             methane
            MoleculeDefinition       local
            CFLambdaHistogramSize    120
            CBMCProbability          0.0
            TranslationProbability   1.0
            ReinsertionProbability   1.0
            CFGibbsSwapFractionalMoleculeToOtherBoxMoveProbability 1.0
            CFGibbsLambdaChangeMoveProbability 1.0
            CFGibbsFractionalToIntegerMoveProbability 1.0
            CreateNumberOfMolecules  0 0

Component 1 MoleculeName             C20
            MoleculeDefinition       local
            CFLambdaHistogramSize          120
            TranslationProbability         1.0
            RotationProbability            1.0
            ReinsertionProbability         1.0
            CBMCProbability                0.0
            CFGibbsSwapFractionalMoleculeToOtherBoxMoveProbability 1.0
            CFGibbsLambdaChangeMoveProbability 1.0
            CFGibbsFractionalToIntegerMoveProbability 1.0
            CreateNumberOfMolecules  0 0
```

D

Appendix-D

```
SimulationType                MonteCarlo
NumberOfCycles                50000
NumberOfInitializationCycles  15000
PrintEvery                    2000
RestartFile                   no
ContinueAfterCrash            yes
WriteBinaryRestartFileEvery   2000
Forcefield                    local
CutOffVDW                     14

Box 0 #LIQUID
BoxLengths 60 60 60
BoxAngles 90 90 90
ExternalTemperature 550
ExternalPressure 10000000
Movies       yes
WriteMoviesEvery 1000

Box 1 #GAS
BoxLengths 90 90 90
BoxAngles 90 90 90
ExternalTemperature 550
ExternalPressure 10000000
Movies           yes
WriteMoviesEvery 1000

VolumeChangeProbability 0.1

Component 0 MoleculeName             methane
            MoleculeDefinition       local
            StartingBead             0
            TranslationProbability   1.0
            GibbsSwapProbability     0.5
            ReinsertionProbability   1.0
            CreateNumberOfMolecules  154 917

Component 1 MoleculeName             C20
            MoleculeDefinition       local
            StartingBead             0
            TranslationProbability   1.0
            GibbsSwapProbability     0.5
            ReinsertionProbability   1.0
            RotationProbability      1.0
            CBMCProbability          1.0
            CreateNumberOfMolecules  257 8
```